High repetition rate Bose-Einstein condensate production in a compact, transportable vacuum system

by

Matthew B. Squires

B.S., Brigham Young University, 1999

M.S., Brigham Young University, 2001

A thesis submitted to the

Faculty of the Graduate School of the

University of Colorado in partial fulfillment

of the requirements for the degree of

Doctor of Philosophy

Department of Physics

2008

This thesis entitled:
High repetition rate Bose-Einstein condensate production in a compact, transportable vacuum system
written by Matthew B. Squires
has been approved for the Department of Physics

Dana Z. Anderson

Deborah S. Jin

Date

The final copy of this thesis has been examined by the signatories, and we find that both the content and the form meet acceptable presentation standards of scholarly work in the above mentioned discipline.

Squires, Matthew B. (Ph.D., Physics)

High repetition rate Bose-Einstein condensate production in a compact, transportable vacuum system

Thesis directed by Dr. Dana Z. Anderson

This thesis reports on the design and implementation of a compact ($5 \times 10 \times 30$ cm) two chamber system for rapidly producing ^{87}Rb Bose-Einstein condensates (BEC) on an atom chip with the future goal of a transportable BEC based sensor. We present the first use of anodic bonding to fabricate multi-chamber vacuum systems suitable for BEC production. Anodic bonding is a method for joining silicon and Pyrex and is superior to epoxy based construction because anodically bonded vacuum systems can be baked at temperatures > 300°C. The improved vacuum quality is a key aspect of reproducibly building compact BEC quality vacuum systems. In the two chamber vacuum system the first chamber operates a 2D+ magneto-optical trap (MOT) at a Rb pressure of $\sim 10^{-7}$ torr and produces a flux of cold atoms that loads a 3D MOT in the second, low pressure ($< 10^{-9}$ torr) chamber. When loaded to saturation the 3D MOT contains $\sim 500 \times 10^6$ ^{87}Rb atoms. The laser cooled atoms are magnetically transferred to an atom chip where the atoms are cooled to degeneracy by forced RF evaporation in a tight magnetic trap ($1.8 \times 3.0 \times 0.6$ kHz). The system performance is demonstrated by three modes: the rapid production of sequential BECs of 1×10^5 atoms with a period of < 3.8 s, the number optimized production of a BEC of 4×10^5 atoms in < 10 s, and the speed optimized production of a BEC of 5×10^4 atoms in 2.65 s. Initial experiments demonstrating key elements of rotation sensor are also presented. Specifically splitting atoms on a chip in a compact vacuum system and guiding atoms around a curve. Also presented in this thesis is a rubidium dispenser based on a gold/rubidium alloy that has potential as a clean source of rubidium in cold atom experiments.

Dedication

To Dionne.

Acknowledgements

I would like to give thanks to my Heavenly Father who gave me a curious mind, amazing opportunity, inspiration, and peace when it was hard to see the road.

My wife Dionne has been an astonishing companion and friend though this process. She has been patient and supportive of my dreams, aspirations, and goals. More importantly she has sacrificed her time, energy, and will so I could achieve my dream of a PhD in physics. She has worked and been incredibly successful as a mother; A far more reaching and worthwhile endeavor than all of the work I have done or will ever do. I am in constant amazement of her strength and goodness. I would write more, but it would double the length of this thesis. Thank you Dionne!

My boys (Connor, Spencer, Trey, Drew, and Cade) have kept my grounded and have also sacrificed their time with me. I have loved their gentle encouragement and constant excitement about the world around them.

I would like to thank my parents, George and Jean Squires, for their constant support and encouragement. I would like to thank my dad for our many discussions and pointing me toward many authors (Covey, Drucker, and Collins). I would also like to thank my in-laws, Chuck and Joyce Clifton, for their encouragement and support. I have also been supported by my wider family of siblings, extended family, and wonderful friends. There are too many to name; Their kind words and acts of kindness are too many to list. Allen Tracy deserves special mention for finding me an internship at Lockheed Martin. Thank you to you all!

I often think about the path the brought me to this point and the teachers that taught me. I would especially like to mention a few names: my high school physics teacher Mike Harris for his crystal clear teaching and enthusiasm, Steve Turley at BYU for his mentoring and example, and David Allred at BYU for his friendship, giving me wide latitude in his lab, and teaching me to be an experimental physicist.

I would like to thank those who have had a role in this current chapter of my life. I would like to thank Dana for letting me work on such an amazing experiment, for financial support, and for teaching me physics and life lessons that will long improve my professional and personal life. Leslie Czaia and her amazing technical talents have made my experiments reality, and I have appreciated her friendship and advice. Alex Zozulya on his many trips to Boulder has helped with theory. Victor Bright for teaching me MEMS and being part of my committee. I have been lucky to work with many students: Shane Du and I spent many days and nights together, he left a high standard to follow, Yutaka Imai, Seth Frader-Thompson, Saravanan, Zach Walters, Ben Luey (run silent, run deep), Brian McCarthy, Ricardo Jimenez, Megan Hart, Will Holmgren, Ying-Yu Wang, Allison Churnside, and Carl Wiedemann have all been wonderful to work with before they moved on. Evan Salim, Steve Segal, Rick Chuang, Lynsi Aldridge, and Andrew Holmgren have helped in the final phases. Also Sterling McBride and Steve Lipp at Sarnoff and Rob Mihailovich at Teledyne put in many hours making parts that I would use in my experiments.

And to all of JILA, thanks for making this is one amazing place. I asked for help from all of my committee at some point, Eric Cornell, Debbie Jin, and Heather Lewandowski. Also Carl Wieman for a few discussions on the way to the bus stop. The JILA shop and their expertise, especially Todd Asnicar for all of the glass work and Paul Beckingham for the many electronics projects. The OSEP program (funded by the NSF) for financial support and an incredible learning environment.

Contents

Chapter

Tables

Table

Figures

Figure

Chapter 1

Introduction and background

1.1 Brief history of BEC on a chip

In 2001 the Hänsch group achieved Bose-Einstein condensation (BEC) in a single cell vacuum system using lithographically patterned copper wires on an aluminum nitride chip [1]. This was significant in several ways: the critical magnetic trapping fields were produced by lithographically patterned wires on the chip, the entire BEC production cycle took place in a single vacuum chamber, the total production cycle took less than 10 s with the RF evaporation as fast at 700 ms, the rubidium pressure was modulated with low power UV light, and they were able to transport the BEC 3 mm using an atom motor.[1]

Just after the Hänsch BEC on a chip paper the Zimmerman group also published a paper on making BEC on a chip in a single vacuum chamber [2]. In the Zimmermann experiment the BEC chip was suspended in a larger vacuum chamber with coils mounted inside the vacuum chamber. The chip was positioned next to the coils for optimal optical access and easy transfer of atoms to the chip trap. Instead of using UV light to modulate the rubidium pressure a pulse of current was sent though a rubidium dispenser for a few seconds to increase the number captured in the magneto-optical trap (MOT) [3]. Similar to the Hänsch experiment the rubidium dispensing was turned off and the MOT

[1] This paper was published right as I was starting my PhD and after reading it I was very interested in BEC on a chip. Dana had just returned from a sabbatical in Germany working with the Hänsch group and was starting his own BEC on a chip effort at CU.

was held to allow the vacuum to recover before moving on to evaporative cooling. The atoms in the MOT were captured and partially cooled by RF evaporation in a magnetic coil trap. After precooling the atoms were transfered to the chip trap for the final evaporation to BEC.

The significance these two initial demonstration of rapidly producing BEC on chip in a single vacuum chamber was the potential of simplifying and speeding up BEC production. Using a lithographically patterned chip meant that preexisting technologies could be used to develop complex chips for creating and manipulating BECs. Because of the compact and rapid nature of chip based BEC production there was the real possibility of using BEC in real world applications.

BEC on a chip came 6-7 years after the 1st BEC by the groups of Carl Wieman and Eric Cornell at JILA/University of Colorado at Boulder (JILA/CU) [4] and shortly after by Wolfgang Ketterle at MIT [5]. The first BEC machine at CU used a single vacuum chamber and operated at a very low rubidium partial pressure to maintain a magnetic trap lifetime long enough for efficient evaporation. Because of the low rubidium pressure it took five minutes to load the MOT. After a sufficient number of atoms were collected in the MOT the atoms were then transfered to a magnetic trap and cooled to a BEC by evaporative cooling. After the initial demonstrations of BEC in a single vacuum chamber most experiments moved to two chamber vacuum systems where the first chamber was operated at a high alkali metal vapor pressure to quickly gather a large MOT. The second chamber was held a low vacuum pressure to maintain a long magnetic trap lifetime for efficient evaporative cooling to BEC. Most BEC experiments use custom vacuum systems to accommodate the various requirements of collecting a large MOT, transferring the atoms to the BEC chamber, creating a BEC, and then performing various experiments with the cold atoms. The lifetime of a typical BEC apparatus is typically 5–10 years and new experiments are built to take advantage of BEC developments. Because of this each BEC experiment tends to be a

highly customized apparatus, though there has been an effort to develop a simplified and straight forward system for making BEC using off the shelf components [6]. The simplifications and speed increases made possible by BEC on a chip have simplified BEC experiments to the point where BEC could potentially be made available as a tool to a wider spectrum of researchers and for applications of coherent atoms.

1.2 Applications of BEC and apparatus for portable BEC

Well before the experimental realization of BEC it was appreciated that building an atom interferometer could be used for measurements with a significant increase in sensitivity [7]. In particular an atom based Sagnac gyroscope is 10^{11} times more sensitive to rotations that a comparable light based Sagnac gyroscope [8]. Compared to light, atoms are very sensitive to a wide array of stimulus (gravity, static magnetic fields, etc.) and that sensitivity could be used to develop a wide variety of precision sensors not possible using light interferometers.

In the past few funding cycles there has been a push to develop atom interferometers and to simplify the apparatus required for making BEC so atom based sensors could be "taken on the road". A BEC apparatus roughly consists of a vacuum chamber, a set of magnetic coils and power supplies, 3-4 lasers, an imaging system, and a timing/imaging system. When a visitor first walks into a BEC lab the jungle of lenses, mirrors, and fiber optics normally catches the eye. Fortunately BEC optical systems can be simplified and compacted without any significant change in paradigm. High performance, compact laser systems have been the focus of telecom companies for longer than a decade so it is reasonable to assume the laser system can be simplified and compacted using current technologies. The same is also true of the timing and imaging systems (e.g. cell phones). Because of these advances most of the BEC on a chip effort at CU has purposely ignored trying to modularize these systems.

The other major elements of a BEC machine is the vacuum system and the

magnetic coils. These two elements typically scale together because magnetic coils are often mounted outside the vacuum system so the larger the vacuum system the larger the coils and corresponding power supplies. In cold atom experiments the atoms are typically trapped using magnetic field gradients which scale like $N\,I r^{-2}$ where N is the number of turns in the coil, I is the current, and r is the radius of the coil or the distance away from the wire. Typical BEC experiments use 100's of Amps in multiturn coils to generate the magnetic fields for transporting and/or producing BEC [9, 6]. Typical BEC on a chip experiments use ≤ 5 A in a single wire on a chip with an area typically less than 2 cm^2. Because of the reduction in current and size there is the possibility that by using a BEC chip the vacuum apparatus and the magnetic field generation can both be compacted.

As explained above $\nabla B \propto N\,I r^{-2}$, this result holds for anti-Helmholtz coil pairs and straight wires where r is the distance from the center of the coil pair to edge of the coil or from the center of the wire to a point outside of the wire. In a non-chip system $r \sim 5 \times 10^{-2}$ m and in a chip based system $r \sim 10^{-4}$ m. For the same magnetic-field gradient the current required for a chip based system is $\sim 10^{-5}$ the total current of an anti-Helmholtz coil pair. This means that the required power for chip based BECs systems can be significantly reduced and could be powered by batteries. Though not directly related, using a chip can also reduce the overall size of the vacuum system and the associated magnetic field coils.

One of the key parameters in almost any cold atom experiment is vacuum quality. But how good does the vacuum quality need to be for making BEC and can the vacuum apparatus be simplified? The vacuum quality required for making BEC is directly related to how fast the atoms rethermalize in the evaporation process [1, 10], and the rethermalization time τ_{therm} is directly related to how tightly the atoms are compressed in the magnetic trap. Magnetic trap compression is expressed in terms of the classical trap frequencies ω of the magnetic trapping potential (think of marbles oscillating in

a bowl). It is straightforward to show that $\omega \propto \nabla B$ where B is the total magnetic field. Increasing the magnetic-field gradient by bringing the atoms closer to the chip wires facilitates a faster evaporation thus relaxing the vacuum requirement. Typical trap frequencies in coil based BEC systems are on the order of 100 Hz and in chip based systems are on the order of 1,000 Hz. Based on the relative trap frequencies there should be a speed increase and relaxed vacuum requirement by a factor of about 10 by using chip based BEC production versus coil based BEC production.

This speed up is directly related to the tight trapping potential made possible by trapping atoms with wires on a chip. Additionally, the size reductions needed to make a portable BEC system are made possible by using chips to compact the vacuum system and relax the vacuum requirement. The principle of rapid evaporation is applicable to any trap with a tight trapping potential. For example, optical dipole traps with trap frequencies on the order of kHz have also produced BEC in a few seconds and with relaxed vacuum requirements [11, 12].

1.3 BEC in a single cell at CU

In December of 2004 BEC on a chip was produced in a portable ($30 \times 30 \times 15$ cm) single chamber vacuum cell at CU [13]. The details of making BEC in this system are described in Reference [14] but for background the key details and history are briefly reviewed. The vacuum cell was made by epoxying a lithographically patterned chip to the top of a lapped quartz flourimeter cell. Because it was a single chamber cell UV light was used to modulate the rubidium pressure in the cell for improved MOT loading speed and number. At the beginning of the MOT phase the UV light was turned on for a few seconds to load $6 - 10 \times 10^6$ atoms into the MOT. After the UV light was turned off the MOT was held for 5-10 s before transferring to the magnetic trap to allow the vacuum pressure to recover from the UV induced pressure increase. After background pressure recovery the chip magnetic trap lifetime was typically 3-4 s. After

additional optical compression and cooling $2 - 3 \times 10^6$ atoms were transfered into the chip-Z magnetic trap and after 4 s of evaporation a BEC was formed.

The vacuum cell that produced BEC was the 4th or 5th cell that had been built and tested at CU during the experimental setup which started from a bare optics table. Unfortunately, about a month after achieving BEC a leak formed in the cell. At the time a new cell had already built and baked out, however UV light desorption in the replacement cell was significantly less effective compared to previous cells. Multiple cells were tested over a period of approximately a year with wide variability in the vacuum quality and the rubidium modulation via UV light desorption. Also, on time scale of a month the vacuum quality of the vacuum cells degraded to the point that the cells could not be used to produce BEC.

Around the same time CU and Sarnoff Corporation started collaborating on new methods of building compact ultra high vacuum (UHV) cells that would be compatible with making BEC. Sarnoff made several cells using anodic bonding to attach a silicon chip to the end of a Pyrex cell (see Section 4.2). These anodically bonded cells showed no long term vacuum degradation which solved a significant problem with the epoxied cells. However UV light did not modulate the rubidium pressure in anodically bonded cells. In the epoxied cells the UV desorption was highly variable but in the anodically bonded cells the UV desorption was completely absent. This was attributed to the high bakeout temperature ($> 300°$C) made possible using anodic bonding. The bakeout temperature of the epoxied cells had been $\sim 150°$C, so the high temperature bakeout was a key benefit of anodic bonding because the vacuum quality was significantly improved.

Additionally anodically bonded cells showed no vacuum degradation over the period of several months and multiple bakeouts. While anodically bonded cells were not amenable to rubidium pressure modulation using UV light the improvement in the short and long term vacuum quality was significant, so there needed to be a way to create BEC in a compact vacuum system without using UV light desorption to modulate

the rubidium pressure. This thesis details the process of how BEC was achieved in a compact anodically bonded vacuum system.

1.4 Comparing BEC and the laser

It is interesting, but maybe not surprising, to consider Einstein separately contributed to the theory of the laser [15] and BEC [16]. Many similarities from physical [17] and technological [18] standpoints have been drawn between the laser and BEC. From a physics standpoint both the laser and BEC depend on the statistics of Bosons that results in a macroscopic occupation of a single quantum state. For both the photon and the atom the probability of scattering into a state depends on the occupation levels of the system and in that sense the physics of a laser and a BEC can be directly compared.

A BEC can also be compared to the laser from a technological development point of view. Initially the laser started as most research efforts; It required skill and understanding of special techniques to make and build a laser. In our view the success of lasers as a part of everyday life can be attributed to two significant developments in the field of lasers [19, 20]. Examining the significance of these developments and looking at the success of lasers the general requirements and technologies that are needed to make BEC a viable technological tool can be extrapolated.

The first is the development of the laser diode in its various forms. Replacing the crystal lasing medium with a small piece of appropriately doped semiconductor that can be mass produced was a significant advance in laser technology. The key improvements of the laser diode are the reduced size, power consumption, and cost has made lasers ubiquitous in a wide variety of products.

The second development, fiber optics, has allowed lasers to be part of everyday life is arguably not even part of a laser. Laser light is an amazing medium but can be very sensitive to environmental effects (e.g. smoke, clouds, moisture, etc.) especially

over long distances. Fiber optics provides a pristine and stable environment for lasers to be sent wherever the light needs to be. The key improvement of fiber optics is the ability to isolate light from the effects of its surroundings and simplify light distribution.

While the results of this thesis will not produce BEC is a package less than 1 mm^3 or transport BEC across the continent, they have the potential to lead to a compact device that is portable and can produce BEC with reduced power consumption. Because of the two chamber system and relaxed vacuum requirement there is the possibility that a BEC can be produced outside of the controlled laboratory environment and be transported to a variety of locations.

1.5 My contributions

My contributions to this thesis are the initial experiments with gold as rapid rubidium dispenser in anodically bonded cells to compensate for the lack of UV light rubidium desorption. Gold was not used as a rubidium dispenser in the final two chamber BEC cell because the time scale of the rubidium pressure modulation is on the order of 10's of seconds. The gold results are included in this thesis because gold still has excellent potential as a dispenser and pump in compact BEC systems. While I performed the initial experiments of gold dispensing with and without a MOT, the final gold pumping and dispensing experiments were performed by Ben Luey and Will Holmgren.

Because of the difficulty of modulating the rubidium pressure in anodically bonded cells I implemented a six-beam MOT and a magnetic trap to load and transfer at minimum a few 10^6 atoms into the chip magnetic trap while maintaining a low rubidium pressure. A six-beam MOT and magnetic transport are commonplace, but in order to facilitate transfer to the chip the MOT is operated with angled beams to bring the MOT closer to the chip. This angled MOT was first modeled with a basic Monte-Carlo simulation and was then implemented in the experiment. The other unique aspect of

this configuration is using a large Z-shaped wire to magnetically transport and then adiabatically transfer atoms to the chip-Z trap.

Instead of a pulsed dispenser a two-chamber vacuum system was implemented with a 2D MOT in a high rubidium vapor pressure chamber and a 3D MOT in a UHV chamber. Evan Salim had implemented an all glass compact two chamber system with a 2D MOT in one chamber loading a 3D MOT in a second chamber. This was not the first time that a 2D MOT was used in a multichamber system, but special attention was made to not significantly increase the size compared to the single chamber design. The experience from these experiments was applied to making a compact two chamber system with an atom chip suitable for BEC production.

Using a 2D MOT to load a 3D MOT significantly improved the number that could be captured in the 3D MOT. After the MOT atoms were magnetically captured and coupled onto the atom chip BEC was produced in three significant modes. A high repetition rate mode where 30 BECs were sequentially made with a BEC being produced every 3.65 s. This production mode demonstrated the possibility of using BEC in a real world application where BEC will need to be consistently and rapidly produced. The second significant production mode was optimizing the production for the largest BEC number. While optimizing a BEC machine for largest number is not unique, comparing the BEC number ($\sim 400 \times 10^3$) and production time (< 10 s) put this system within an order of magnitude of the highest throughput rubidium BEC systems [9]. If the size of the vacuum system is taken into account ($5 \times 10 \times 30$ cm) this is one of the smallest BEC systems.[2] If size and BEC throughput are considered together then this apparatus is a significant advance in BEC production. The BEC apparatus was also optimized to produce BEC as fast as possible and is able to produce BEC from MOT loading to taking images of BEC in < 2.65 s. The final BEC mode produces BEC in a magnetic

[2] Here size denotes the size of the vacuum system and magnetic coils. No efforts to simplify the laser/control systems will be discussed in this thesis, but it is worth mentioning CU plus a few companies are in the process of simplifying and compacting the laser system.

trap 300 μm from the chip surface and with trap frequencies suitable for splitting a BEC with an optical pulse.

Additionally, there is some preliminary work on techniques that would be needed to make a Sangac gyroscope. The first experiment is splitting a BEC or cold atoms with a standing light wave. Again splitting a cloud of atoms with a standing light wave is not new, but splitting close to a chip that forms one wall of the vacuum chamber had not been previously performed. Steven Segal helped with the splitting beam setup especially the optomechanics around the cell. The second experiment is a curved waveguide that was used to guide atoms around a curve with a 1 cm radius. Guiding atoms around curves has been done previously [21, 22] but this method of guiding the atoms created a moving 'bucket' where the atoms could be accelerated as they moved around the curve. This was done with the help of Evan Salim and Ben Luey, plus theoretical support by Alex Zozulya.

1.6 Outline of the rest of thesis

The rest of the thesis will be organized as follows: First the basic theory of chip magnetic traps, MOTs, vacuum considerations in small systems, BEC, and atom splitting will be covered. These topics will be covered at a level that was useful for me in designing and conducting cold atom experiments. Then a potential rubidium dispenser based on the properties of the gold/rubidium alloy, however this dispenser was not used in the final experimental configuration. While the dispenser was not used in the final BEC configuration the technology and potential applications are still noteworthy as a rubidium dispenser and pump. The final configuration used for BEC production will then be detailed followed by the specifics of the various operating modes used to produce BEC. The final chapter will be experimental results of curved waveguiding and the splitting of a BEC/cold atoms on a simply supported chip with a standing light field as a groundwork for future chip based experiments.

Chapter 2

Essential theory

Theory is a strong word for this chapter. This is mostly a collection of basic formulas and ideas needed for back of the envelope calculations related to vacuum cells, magnetic traps made from wires and bias fields, MOTs, and BEC. Reference [10] is an excellent summary of chip based magnetic traps and BEC on a chip. Reference [14] additionally provides excellent derivations of the interaction of atoms and lasers, chip traps, imaging, etc.

2.1 Magnetically trapping atoms

Classically atoms can be modeled as miniature bar magnets where the energy of the atom in a magnetic field **B** is

$$U = \overrightarrow{\mu_c} \cdot \overrightarrow{B} \tag{2.1}$$

where μ_c is the classical magnetic dipole moment. If μ_c is (anti-)aligned with the magnetic field then the bar magnet will be in a (high)low energy state. Assuming atoms are bar magnets allows many magnetic trapping properties to be described, but atoms are fundamentally quantum mechanical objects. Quantum mechanically there is not a continuum of dipole and magnetic-field alignments but the alignments are quantized. Equation 2.1 becomes

$$U = \mu_m \, B \tag{2.2}$$

where $\mu_m = \mu_B\ m_F\ g_F$. Here μ_B is the Bohr magneton, m_F is the magnetic quantum number, and g_F is the Lande g-factor. The magnetic quantum number has values $F_- \leq m_F \geq F_+$ where F is the total atomic angular momentum ($F_\pm = J \pm I$) . The Lande g-factor can be positive or negative depending on the atom and the atomic state. Depending on the product of $m_F\ g_F$ the atom can be put into a high-field seeking state ($m_F\ g_F < 0$), a clock state ($m_F\ g_F = 0$), or a weak-field seeking state ($m_F\ g_F > 0$). Most BEC applications trap atoms in the weak-field seeking states because the Ernshaw theorem [23] states in steady state a magnetic-field maximum cannot be created in free space. In ^{87}Rb atoms are typically trapped in the $|F = 1, m_F = -1\rangle$ ($g_F = -1/2$) or the $|F = 2, m_F = 2\rangle$ ($g_F = 1/2$) states.

The force experienced by an atom in a magnetic field is

$$\mathbf{F} = -\nabla U = -\mu_m\ \nabla B. \tag{2.3}$$

This expression is useful for calculating the magnetic-field gradient needed to hold atoms against gravity. For atoms in the $|F = 2, m_F = 2\rangle(|F = 1, m_F = -1\rangle)$ state $\nabla B \approx$15(30) G/cm to cancel gravity.

The other consideration when trapping atoms, especially cold atoms, is how to maintain the alignment of the magnetic dipole moment as an atom moves in a magnetic trapping potential. Classically a bar magnet can be given angular momentum by rotating the bar magnet. This will cause the bar magnet to precess around the direction of the magnetic field and will maintain the average alignment of the bar magnet in the magnetic field. If the direction of magnetic field is slowly varied then the orientation of the bar magnet will follow the magnetic field. The definition of slowly is

$$\frac{d\theta}{dt} < \omega \tag{2.4}$$

where θ is the instantaneous alignment of the magnet with the magnetic field and ω is the precession frequency. For atoms the Larmor frequency is equivalent to the precession

frequency. The trapping requirement is now

$$\frac{d\theta}{dt} < \frac{\mu_m |B|}{\hbar} = \omega_L \tag{2.5}$$

where ω_L is the Lamor frequency. This puts a minimum value on the magnetic field that will prevent atoms from 'flipping' the value of m_F. Atoms in the strong-field state are especially sensitive to this flipping because they are aligned opposite the direction of the magnetic field and if they flip it is into an anti-trapped (high field seeking) state. Atom loss due to m_F flipping is often called spin-flip or Marjorana loses. The region where the magnetic trapping field is too low to maintain atoms in the trapped state is typically called a 'hole in the bottom of the trap' [24]. The minimum magnetic field to avoid Marjorana losses is typically a few Gauss, but the actual value of the 'bottom field' depends on the temperature (i.e. velocity) of the atoms and ∇B.

2.2 Basic wire magnetic trap

The magnitude of the magnetic field and gradient for an infinitely long wire is

$$B = \beta \frac{I}{r} \tag{2.6}$$

$$B' = \beta \frac{I}{r^2} \tag{2.7}$$

where $\beta \equiv \mu_0/(2\pi) = 2 \times 10^{-7}$ N A^{-2} and all negative signs have been dropped. The magnetic field circulates around the wire according to the right hand rule and when a perpendicular (relative to the wire) bias field is added a magnetic minimum is created at a finite distance from the wire

$$B_{trap} = \left| \beta \frac{I}{r} - B_\perp \right|. \tag{2.8}$$

The gradient of the magnetic trap is the same as when there was no bias field. The distance of the magnetic minimum from the wire and the gradient at the minimum are

$$r_{min} = \beta \frac{I}{B_\perp} \tag{2.9}$$

$$B'_{min} = \frac{B_\perp^2}{\beta I}. \tag{2.10}$$

As mentioned above if the atoms pass though a zero magnetic field they will spin flip into an untrapped magnetic state and be lost from the magnetic trap. The zero of the wire magnetic field is 'plugged' by adding a uniform magnetic field parallel to the wire. The total trapping field is

$$B_{tot} = \sqrt{B_{trap}^2 + B_{\parallel}^2}. \tag{2.11}$$

Traps are characterized by their trap frequency assuming the trap is harmonic

$$\omega = \sqrt{\frac{\mu_m B''}{m_{Rb}}}. \tag{2.12}$$

If Equation 2.11 is expanded around the trap minimum then

$$\omega \propto \frac{B'}{\sqrt{B_{\parallel}}} \tag{2.13}$$

2.2.1 Z-wire trap

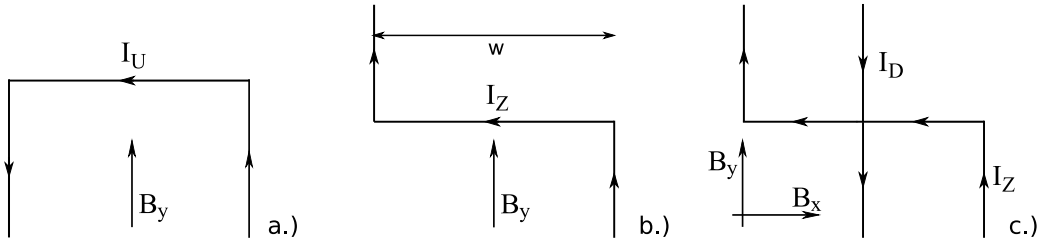

Figure 2.1: Figure a.) shows a U-wire configuration for creating a quadrupole magnetic trap. Figure b.) shows a Z-wire configuration for creating a Ioffe-Prichard magnetic trap. Figure c.) shows the wire configuration for creating a dimple trap. By themselves these wire configurations will not produce magnetic traps and must be augmented with external bias fields as shown.

From the magnetic field of a single wire two simple chip wire traps can be made by bending the ends wire (see Figure 2.1). The first is the U-wire trap that make a quadrupole trap (zero minimum field), and a Z-wire trap that makes a Ioffe-Prichard trap (non-zero minimum field). The U-wire trap can be used to make a mirror MOT [25] close to the surface of the chip and was used in first single chamber BEC experiments [18], however cold atoms need a non-zero minimum bias field to avoid Majorana losses

so the Z-wire trap is used for BEC production. While a U-wire was used in the first BEC on a chip experiment [1] the current BEC production cycle exclusively uses a Z-wire trap.

The trap frequencies of a Z-wire trap can be approximated by assuming there is one weak axis (longitudinal or axial axis) nearly parallel with the x-axis, and two tight axes (transverse or radial axis). Assuming $z \ll w$ (see Figure 2.1) then then the longitudinal trapping field can be approximated by two half-infinite wires

$$B(x) = B_0 + B_2 x^2 + \ldots \tag{2.14}$$

where

$$B_0 = \left| B_x + 4\beta \frac{I_Z z_0}{w^2} \right| \tag{2.15}$$

$$B_2 = 8\beta \frac{I_Z(6B_x z_0 + \beta I_Z)}{w^4 \left| B_x + 4\beta \frac{I_Z z_0}{w^2} \right|} \tag{2.16}$$

where $z_0 = \beta I_z / B_y$. In this expansion there is no first order term so the frequency along the longitudinal axis is given by Equation 2.12. The transverse trap frequencies of a Z-wire trap are approximately

$$\omega_\perp = \sqrt{\mu_m / m_{Rb}} \frac{B_y^2}{\beta I_Z \sqrt{B_0}}. \tag{2.17}$$

The Z-wire trap will be also be used for magnetically transporting atoms over several cm's so it cannot always be assumed that $z \ll w$. The key aspects to consider when the atoms are far away the Z-wire is maintaining the trap gradient along the transverse axis and trap depth along the longitudinal axis. Far enough away from a Z-wire the field will largely be the field of a long straight wire except for the location of the kink in the wire. Both the transverse and the longitudinal traps will be negligible at $z \gg w$. The transverse magnetic field from a Z-wire can be approximated by the

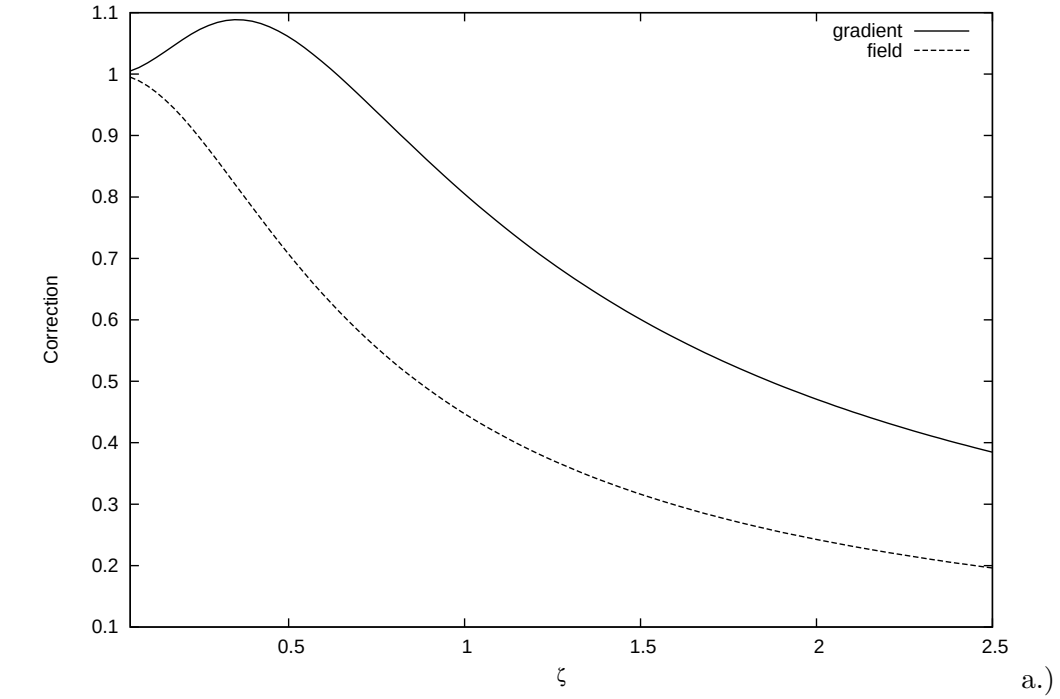

a.)

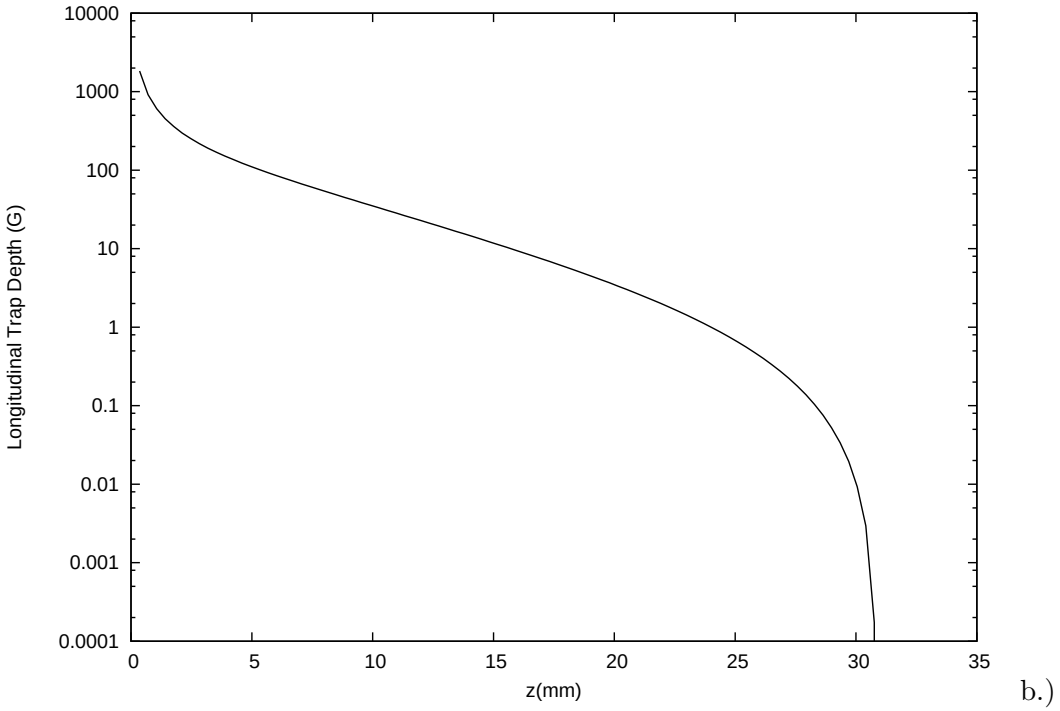

b.)

Figure 2.2: Figure a.) shows the correction factor for the magnetic field and gradient of a short piece of wire as a function of distance from the wire. The distance from the wire is scaled to the width of the wire section. The correction is relative to the fields of an infinitely long wire. Figure b.) shows the approximate trap depth of a 30 mm Z-wire running 5×130 A as a function of distance from the center of the Z-wire. The trap depth is the maximum magnetic field toward the edges of the Z-wire minus the field at the center of the Z-wire.

magnetic field of a short section of wire

$$B_{finite} = B_\infty \frac{1}{\sqrt{1+4\zeta^2}} \tag{2.18}$$

$$B'_{finite} = B'_\infty \frac{8\zeta^2+1}{(4\zeta^2+1)^{3/2}} \tag{2.19}$$

where $\zeta = z/w$ and B'_∞ is the field of an infinitely long wire (Equation 2.7). The correction factors are shown in Figure 2.2a and it is interesting to note that for distances less than $w/2$ the field gradient of a short wire is slightly greater than the gradient of a long wire but then quickly falls off.

The trap depth of the longitudinal field is approximated by field of two long wires separated by w and taking the difference of the maximum field versus the field at the center of the wires at a height z

$$B_{depth} = \beta I_Z \left(\frac{\sqrt{w^2+\sqrt{w^4+16z_0^2w^2}}}{2\sqrt{2}wz_0} - \frac{4z_0}{w^2+4z_0^2} \right). \tag{2.20}$$

As seen in Figure 2.2b the longitudinal trap depth becomes zero for values greater than $\sim w$. For atoms in the $|2,2\rangle$ state 1G$\approx$ 67 μk. For an atom cloud after the optical molasses stage the typical temperature is 20–50 μk and assuming the trap should be 5–7 times deeper than the temperature [10] then the minimum trap depth should be 2-5 G. As seen in Figure 2.2b that is approximately 20 mm or about 2/3 the size of the external Z-wire. That is for the specific parameters of the initial external Z-wire trap of Section 4.4.6. Because the longitudinal trap depth rolls off more quickly than transverse trapping force the width of the Z-wire is the limiting factor of the maximum distance that atoms can be trapped by the field of a Z-wire trap.

2.3 Dimple trap

A Z-wire trap typically has two tight axes and one significantly weaker axis. The weak axis of the trap limits the total effective trap frequency because $\bar{\omega} = (\omega_1\,\omega_2\,\omega_3)^{1/3}$.

This is especially true when the chip Z-wire is wide as in this thesis (see Section 4.4.6). To counter this a sequence of smaller chip Z-wires could be energized to compress the weak axis of the magnetic trap [10]. This scheme is slightly more complicated because it would require an independent current driver for each of the Z-wire legs.

A dimple trap in the center of the chip Z-wire accomplishes the same purpose by adding a relatively strong trapping potential perpendicular to the chip Z-wire field. While the dimple trap accomplishes the same effect as compressing a sequence of Z-wires it requires only one additional current driver.

2.3.1 Basic properties

A dimple trap is made using a wire configuration shown in Figure 2.1c plus B_x and B_y bias fields to essentially overlap two magnetic waveguides. Because the dimple trap is the vector sum of two long wire fields plus the corresponding bias fields the properties of the dimple trap are a vector sum of the total field. This can be see in Figure 2.3 where the trap is centered over the origin in the XY plane but the residual traps from the I_x and I_y wire currents can be seen extending from the origin. While a dimple trap can achieve a higher $\bar{\omega}$ than a Z-wire trap the various bias fields can no longer be considered orthogonal and independent. The behavior and applications of the dimple trap are described in the following section.

2.3.1.1 Dominant wire determination

The dimple trap is formed by taking the vector sum of two magnetic fields that each have there own zero. One the magnetic fields zeros is dominant and determines the position of the magnetic trap. Assume the minima are at r_0 and r_1 with magnetic field gradients B'_0 and B'_1. The dominant magnetic trap will be at the global field minimum. Assuming the field around the minima is well described by a linear gradient so the

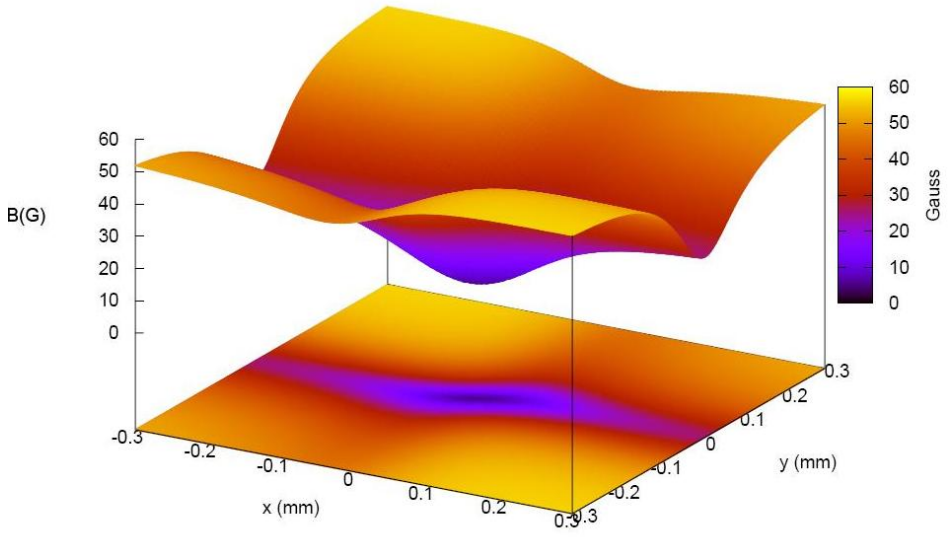

a.)

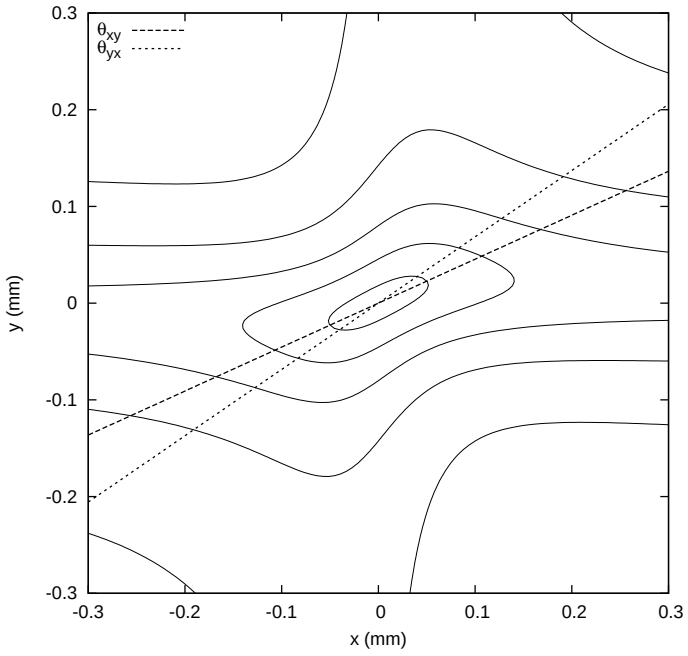

b.)

Figure 2.3: A calculation of the dimple trap used for BEC production. The following parameters were used to generate this representation: I_x = 1.25 A, I_y = 3.75 A, B_x = -38 G, I_y = 46 G. Figure a.) shows a 2D slice though the center of the magnetic trap parallel to the chip surface with the magnetic field shown on the Z-axis and in false color. Figure b.) shows a contour plot of the same trapping potential showing the two calculations for the trap rotation angle.

magnetic field at each minimum is

$$B_{0,1} = B'_{0,1}\Delta r \tag{2.21}$$

where $\Delta r = |r_0 - r_1|$. So the dominant minimum is created by the field with the largest gradient. While there is a dominant trap it is possible to have the atoms stably trapped in the secondary trap if the atoms start in the secondary trap and the energy barrier between the dominant and secondary minima is much greater than the temperature of the atom cloud.

2.3.1.2 Dimple trap depth

The depth of the dimple trap is defined as the difference of the magnetic field directly above the wire crossing and at the far extent of the dominant wire. Assume the dimple is formed at z_0 so the depth of the trap is

$$B_{depth} = B(\infty, z_0) - B(0, z_0) \tag{2.22}$$

where

$$B(x, z_0) = \left| \beta \frac{I_y \, z_0}{x^2 + z_0^2} - Bx \right|. \tag{2.23}$$

Inserting Equation 2.23 into Equation 2.22 the trap depth is

$$B_{depth} = \begin{cases} 2B_x - \beta \frac{I_y}{z_0} & B_x < \beta \frac{I_y}{z_0} \\ \beta \frac{I_y}{z_0} & B_x > \beta \frac{I_y}{z_0} \end{cases}. \tag{2.24}$$

Thus the maximum depth of the dimple trap is determined by the wire that generates the dimple trap and is simply the magnetic field of the dimple wire at z_0 (see Figure 2.4). The dimple trap depth is different than other wire traps where the trap depth is almost entirely a function of the trap bias field [25]. The dimple trap depth for reasonable parameters is significantly deep enough to trap laser cooled atoms. See Figure 2.5 for dimple trap depth versus the dimple trapping current.

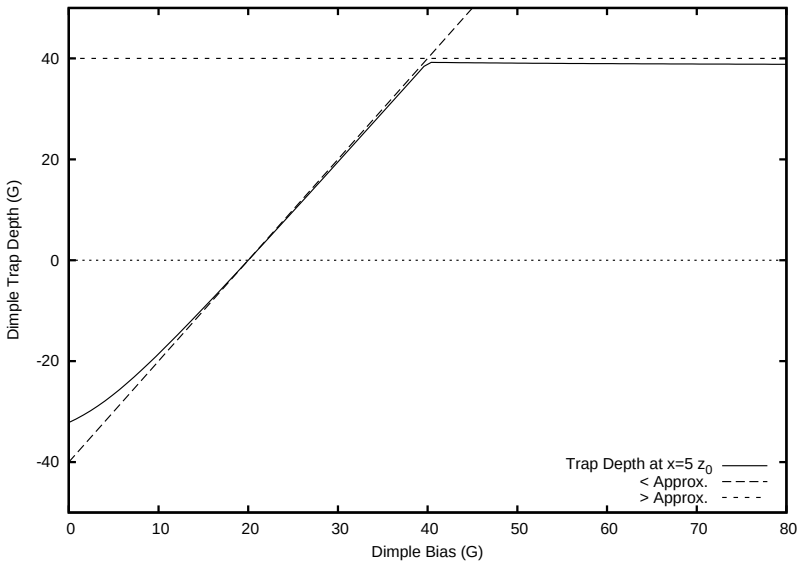

Figure 2.4: Dimple trap depth showing calculation of trap depth assuming depth is evaluated relative to the side of the trap. The calculation assumes $I_x = 5$ A, $I_y = 2.5$ A, and $B_y = 80$ G. Also shown are the limits assuming the depth is evaluated at the trap center and at infinity. For values less than 20 G there is no dimple trap and the resulting potential will split the cloud.

2.3.2 Trap frequency calculation

As seen in Figure 2.3b the dimple trap is rotated relative to the wires that create the magnetic field. This is due to the vector sum of two orthogonal infinite magnetic waveguides. Calculating the trap frequencies beyond the infinite wire approximation requires the angle of the magnetic trap to be included because the rotation angle can be large depending on the relative current in the trapping wires [26].

The trap rotation angle is determined by minimizing the directional derivative $(\nabla|B|\cdot\mathbf{b})$ in the XY plane ($B_z = 0$) at the minimum of the trapping field. Oddly enough there are two similar but slightly different answers depending on the order that x and y are set to zero.

$$\tan(\theta_{xy}) = \frac{-I_x}{I_y} \tag{2.25}$$

$$\tan(\theta_{yx}) = \frac{1}{2B_x/B_y + I_y/I_x} \tag{2.26}$$

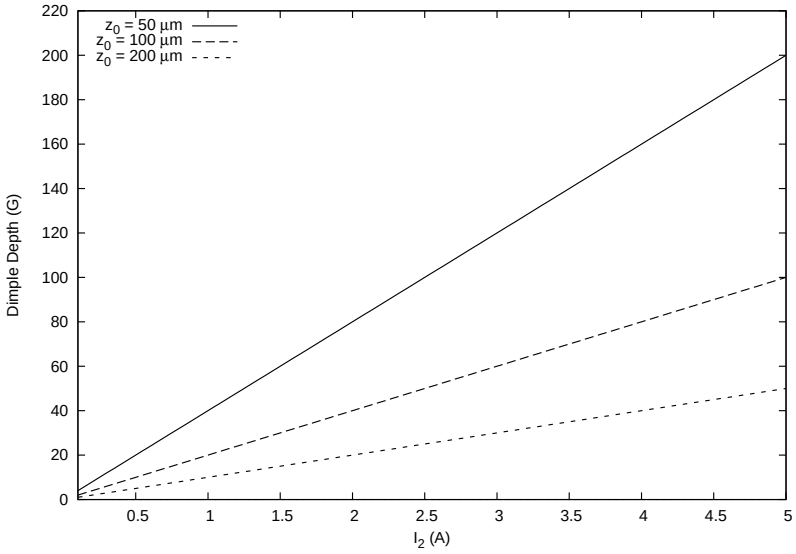

Figure 2.5: Dimple trap depth as a function of distance away from the wire center and current in the wire.

where the order in which the coordinates are set to is denoted by the subscript. As seen in Figure 2.3b both approximations give a reasonable estimate of the trap rotation. For the sake of simplicity and consistency with other derivations [27] assume $\theta_D = \theta_{xy}$.

By Taylor expanding around the trap minimum with the appropriate angle correction gives

$$B_t = B_0 + \frac{1}{2\eta^2}\frac{B'^2}{B_0}t^2 + \dots \tag{2.27}$$

$$B_l = B_0 - \eta(\gamma+\eta)\frac{B'^2}{B_0}l^2 + \dots \tag{2.28}$$

$$B_z = B_0 + B_y\eta(\gamma+\eta)\frac{B'}{B_0}z_0 + \frac{B'^2}{2B_0}z_0^2 + \dots \tag{2.29}$$

where $B_0 = B_y|\gamma+\eta|$, $B' = B_y^2/(\beta I_x)$, $\gamma = B_x/B_y$, and $\eta = I_y/I_x$. Assuming η and γ are less than 1 then the dimple trap will have a tight and loose axis as can been seen in Figure 2.3; t denotes the coordinate along the tight direction of the trap and l along the loose direction of the trap.

The frequencies of the dimple trap (using the definition of Equation 2.12) are

$$\omega_t = \frac{\omega_0}{\sqrt{2}\,\eta} \tag{2.30}$$

$$\omega_l = \sqrt{\eta(\gamma+\eta)}\,\omega_0 \tag{2.31}$$

$$\omega_z = \frac{\omega_0}{\sqrt{2}} \tag{2.32}$$

where $\omega_0 = \sqrt{\mu_m/m_{Rb}}\,B'/\sqrt{B_0}$. Because $\eta < 1$ the dimple trap compresses one of the tight axis of the dimple trap. The weak axis of the dimple trap is a function of the main wire trap frequency. This expansion is valid for $\eta > 0$ otherwise the trap frequencies would approach ∞. In the case of $\eta \sim 0$ it cannot be assumed that the trap is a dimple trap and the exact wire pattern must be considered.

2.3.3 Comparison of dimple and Z-wire traps

The dimple trap provides excellent compression in all three dimensions where a trap made using a Z-wire configuration has excellent compression in two dimensions and it is typically weak along one axis. Compare the effective trap frequencies $\bar{\omega}$ to evaluate the merits of the dimple trap versus the Z-wire trap.

2.3.3.1 Z-wire trap

The Z-wire trap is created using a wire pattern shown in Figure 2.1b. As mentioned this type of trap typically has two tightly compressed axes and one axis with weak compression. The trap frequencies of the highly compressed dimensions are

$$\omega_1 = \omega_2 = \sqrt{\mu_m/m_{Rb}}\frac{\beta\,I_Z}{r_z^2\sqrt{B_0}}. \tag{2.33}$$

The trap frequency of the weak dimension can be approximated assuming there are two half infinite wires separated by w_z.

$$\omega_3 \approx \frac{\sqrt{\mu_m/m_{Rb}}}{w_z}\sqrt{\frac{\beta\,I_x}{r_z}} \tag{2.34}$$

The bottom bias field does not appear in the equation because the trap is created by the end caps of the Z-wire trap. Equation 2.34 includes an extra factor of 1/2 to better approximate the shape of the longitudinal axis.

The net effective trap frequency for the Z-wire trap is

$$\bar{\omega}_z = \sqrt{\mu_m/m_{Rb}}\,\beta^{5/6}\left(\frac{I_x^{5/2}}{B_0\, r_z^{9/2} w_z}\right)^{1/3}. \tag{2.35}$$

2.3.3.2 Dimple trap

As explained previously the dimple trap is made from two wires that cross at right angles. For the following calculations assume that the trapping wire and the dimple wire are at the same distance from the atoms r_D and that $I_y = \eta I_x$. This form of the dimple trap is being used instead of Equations 2.30–2.32 because it simplifies the comparison between the two trap. Along the strong direction the trap frequencies are

$$\omega_1 = \omega_2 = \sqrt{\mu_m/m_{Rb}}\frac{\beta\, I_x}{r_D^2\sqrt{B_0}} \tag{2.36}$$

and along the weak direction

$$\omega_3 = \sqrt{\mu_m/m_{Rb}}\frac{\beta\,\eta I_x}{r_D^2\sqrt{B_0}}. \tag{2.37}$$

Together the effective trap frequency is

$$\bar{\omega}_D = \sqrt{\mu_m/m_{Rb}}\frac{\beta\, I_D}{r_D^2\sqrt{B_0}}\sqrt[3]{\eta}. \tag{2.38}$$

2.3.3.3 Compare dimple to Z-wire trap

Set the two effective trap frequencies equal and solve for r_T

$$r_T = \sqrt{\sqrt{\mu_m/m_{Rb}}\beta\frac{I_y\sqrt[3]{\eta}}{\bar{\omega}_z\sqrt{B_0}}}. \tag{2.39}$$

To have the same effective trap frequency as a Z-wire trap the working distance scales as the square root of the dimple current. Even though the dimple trap compensates for the weak axis of the Z-wire trap the dimple current can become prohibitively large very

quickly as the distance from the center of the wire is increased. The values previously used to achieve BEC [18] can be substituted into Equation 2.39 to give an approximate experimental value for r_T ($\eta = 1/2$, $r_z = 80\,\mu m$, $w_z = 2\,mm$, $B_0 = 2\,G$, $I_z = 2.75$ A)

$$r_T \sim 100 \times 10^{-6}\sqrt{I_y}. \tag{2.40}$$

So it may be possible to put wires on the back of a chip structure and still achieve the conditions for rapid BEC production.

2.3.4 BEC without vias

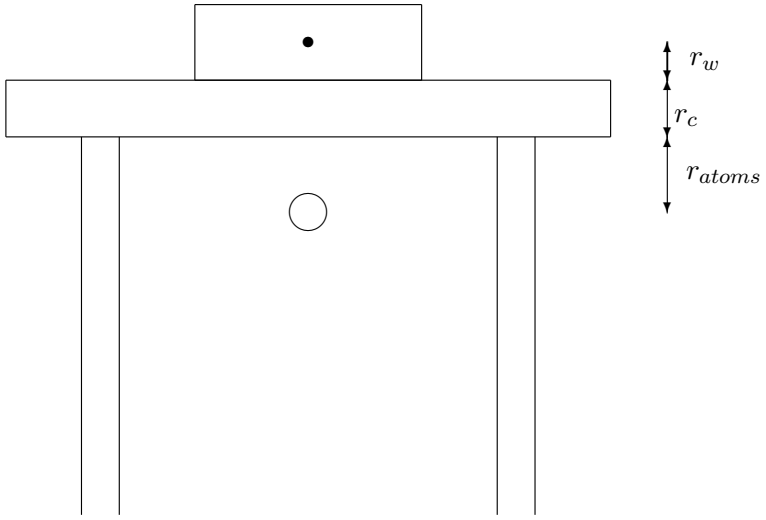

Figure 2.6: Geometry for calculating the optimal chip width r_c and wire currents to create BEC without vias.

This thesis uses ultra-high vacuum compatible vias to pass current though a silicon chip to create a magnetic trap suitable for rapid BEC production. By using a dimple trap it may be possible to create a BEC compatible magnetic trap with wires on the air side of a thin silicon chip. The conditions used in Reference [18] for creating BEC were $I_Z = 2.75$ A, $r_z = 80\,\mu$m, with a wire size of $10 \times 100\,\mu$m, and ~ 15 mm

long. From these parameters the chip Z-wire dissipates about 2 W. What wire and chip configurations will have the same $\bar{\omega}_z$ but dissipate the same power? Assume the geometry is as shown in Figure 2.6 and that the maximum current that can be easily controlled for a few seconds without excessive circuitry is about 50 A.

First define approximate chip thickness limitations. While a 2 cm^2 area and 100 μm thick silicon membrane will support atmospheric pressure other issues need to be considered such as power dissipation and membrane deflection. For the following calculations assume that the thickness of the chip r_c is at least 200 μm to assure structural integrity.

Another issue to consider is the potential for the atoms to collide with the surface of the chip as they are brought close to the chip. Assuming the distance of the atoms from the chip r_{atoms} is 100 μm is a reasonable working distance to avoid atom loss and to facilitate direct imaging of the atom cloud.

2.3.4.1 Wire shapes

Two general wire shapes may be considered, round and rectangular. For optimized magnetic-field gradient and minimized power the rectangular wire is best. The magnetic field from a flat wire with width w is nominally the same as a round wire as long as the field is evaluated at $r \geq w$. The maximum width of the wire that will not show flattening effects is set by the total distance from the center of the wire to the atoms $w_w = r_{atoms} + r_{chip} + r_w$ where $r_w = h_w/2$. The power dissipated in a rectangular wire is

$$P_{rect} = I_D^2 \frac{\rho L}{2 r_w w_w} \tag{2.41}$$

where ρ is the resistivity of the metal and L is the length of the wire. The optimal wire shape is determined by minimizing dP_{rect}/dI_D because the magnetic field is proportional

to I_D and yields $r_w = (r_a + r_c)/2$. The optimal power is

$$P_{rect} = I_D^2 \frac{\rho L}{3/2(r_a + r_c)^2}. \tag{2.42}$$

Rearranging terms in Equation 2.39

$$I_D = r_T^2 \frac{B_{bot}^{1/6} I_z^{5/6}}{r_z^{3/2} w^{1/3} \beta^{1/6} \delta^{1/3}}. \tag{2.43}$$

Equation 2.42 becomes

$$P_{rect} = \frac{27 B_{bot}^{1/3} I_z^{5/3} L \rho}{8 r_z^3 w^{2/3} \beta^{1/3} \delta^{2/3}} (r_a + r_c)^2 \tag{2.44}$$

where the substitution $r_T = 3/2(r_a + r_c)$ is made. The optimized power and current is shown in Figure 2.7 assuming the same BEC values used previously [14].

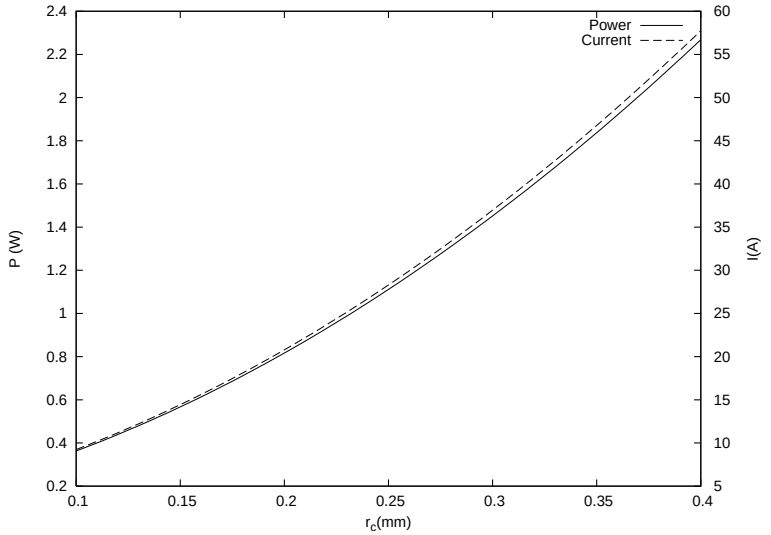

Figure 2.7: Expected power dissipated in a rectangular wire as a function of chip thickness to create trap conditions suitable for BEC production.

2.3.4.2 Bias field requirements

Even though the dimple wires dissipate a reasonable amount of power the bias fields to create the dimple trap may be large. The bias fields (see Figure 2.8) are calculated via Equation 2.6 using the current and distance from Figure 2.7. The current

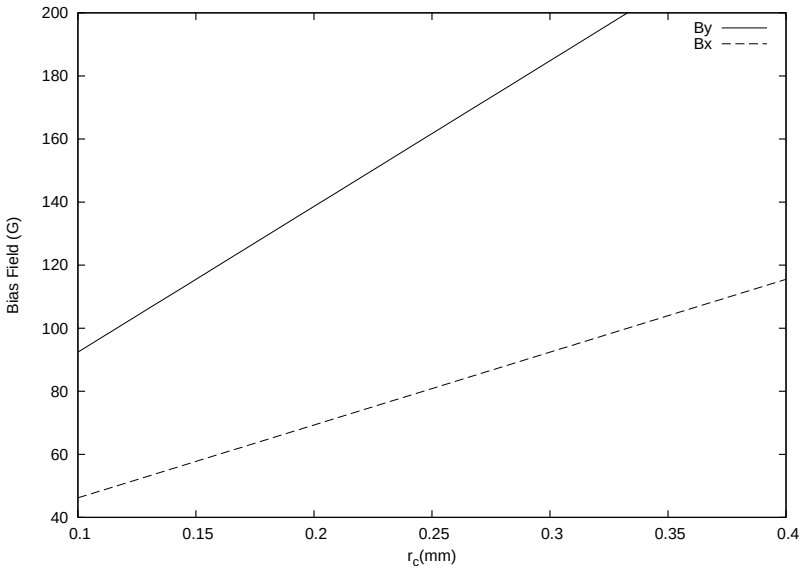

Figure 2.8: Bias fields needed to create a tight dimple magnetic trap as a function of chip thickness.

magnetic field generating coils can create bias fields of $B_x \approx 80$ G and $B_y \approx 160$ G (similar to rectangular coils in Reference [14]). The maximum chip thickness limited by the current bias field configuration is $r_c \approx 250\,\mu$m, $I_D \approx 30$ A, and $P \approx 1.4$ W. These are all reasonable experimental parameters that are currently attainable.

2.3.5 Evaporation during transport

There are currently several efforts to continuously load, evaporate, and produce BEC in a long waveguide [28, 29]. These experiments typically employ a long (one to several meters) waveguide that is tightly confining in 2D. As the atoms propagate along the guide the atomic density and collision rate is sufficient that evaporative cooling is seen in the waveguide. In one experiment the evaporation is accomplished by moving the atoms though various evaporation zones [30].

In another experiment a chip based moving magnetic trap was implemented to move laser cooled atoms 1.75 cm using a periodic potential [31]. Combining the two ideas and using dimple traps to maintain a high $\bar{\omega}$ it is plausible to consider a BEC

"production line" where the atoms are loaded from the optical molasses and optical pumping stage into the first dimple trap. The dimple trap array moves the atoms though evaporation zones until the atoms are finally cooled to BEC. The rate of BEC production would be limited by the MOT loading rate and the time in each evaporation zone. An array of dimples similar to Figure 4.3b but with less spacing between dimple wires could be used to make an array of traps.

2.4 MOTs and BEC chips

MOTs are the workhorse of cold atomic physics experiments and while robust to most imperfections there are several effects contributing to a MOT so the basic physics is not immediately intuitive. The main change to the MOT configuration in this thesis allows a six beam MOT to be positioned about a factor of two closer to the chip surface is explained in Section 2.4.4.

2.4.1 Basic MOT considerations

A MOT provides two different mechanisms (cooling and trapping) from the interaction of several key elements: laser polarization, laser frequencies, magnetic field magnitude, magnetic field direction, and m_F state. For the sake of simplicity cooling and trapping will be discussed as separate processes. First the force on an atom from a single laser is

$$\mathbf{F} = \frac{\hbar \mathbf{k} \Gamma}{2\pi} \frac{S}{1 + NS + 4(\delta_L + \mathbf{k} \cdot \mathbf{v} + \mu_m B/\hbar)^2/\Gamma^2} \tag{2.45}$$

where Γ is the linewidth of the transition, S is the saturation parameter I/I_S, N is the total number of lasers shining on the atoms, and δ_L is the detuning of the laser away from resonance. This equation can be separated into two basic parts: the momentum of a photon ($\hbar\mathbf{k}$) and the number of photons scattered by the atom per unit time (the rest of the equation). The force from a pair of counter-propagating beams with identical

parameters (S, δ, etc.) is

$$\mathbf{F} = \frac{\hbar \mathbf{k} \Gamma S}{2\pi} \left(\frac{1}{1 + NS + 4(\delta_+/\Gamma)^2} - \frac{1}{1 + NS + 4(\delta_-/\Gamma)^2} \right) \tag{2.46}$$

where

$$\delta_\pm = \delta_L \mp \mathbf{k} \cdot \mathbf{v} \pm \mu_m B/\hbar. \tag{2.47}$$

2.4.1.1 Cooling

There are several regimes and limits of laser cooling that depend on a very wide range of operating conditions, but the maximum capture velocity is a straight forward calculation. The maximum possible force on an atom is $\hbar k \Gamma/(2\pi)$ (assume $S \gg 1$ in Equation 2.45) which if divided by m_{Rb} gives an acceleration of $a = 3.5 \times 10^4$ m/s^2! From this acceleration the maximum velocity that can be stopped in a cell of width w is $v_{max} = \sqrt{2aw}$. For typical cell sizes of 1, 2, 3 cm this yields capture velocities of 27, 38, and 46 m/s respectively, all significantly below 240 m/s, the mean velocity of ^{87}Rb at room temperature. The result is only atoms in the low velocity tail of the Maxwell-Boltzmann distribution are captured in a MOT [32].

In laser cooling atoms are cooled because of an apparent velocity dependent force that is directed against the velocity (i.e. $F = -cv$). This damping is greatest when one of the lasers in nearly on resonance with the appropriate laser beam. The damping coefficient c can be calculated by Taylor expanding Equation 2.46 around $\delta_+ \approx 0$ and dropping all terms other than the first order

$$c = \frac{d\mathbf{F}}{dv} = \frac{\hbar \mathbf{k}^2 \Gamma S}{\pi} \frac{4\delta_-}{\left(1 + NS + 4(\delta_-/\Gamma)^2\right)^2}. \tag{2.48}$$

Now consider the interplay between the Doppler and Zeeman shift and determine where each effect dominates in Equation 2.47 (assume $\delta_l = 2\Gamma$). First only consider the effect of the Doppler shift where $v = \delta_l/k$. For the assumed detuning and $\lambda = 780$ nm, $v_{Doppler} = 9.4$ m/s significantly below the maximum capture velocity of even a 1 cm cell. Thus the Doppler effect only contributes after the atoms are cooled below 9 m/s.

Now only consider the effect of the Zeeman shift assuming $B = B'z$ where B' is the gradient of the MOT field along the strong axis. The radius where the Zeeman shift is comparable to the typical laser detuning is

$$z = \frac{2\hbar\Gamma}{\mu_m B'}. \tag{2.49}$$

For a typical MOT gradient of $B' = 12$ G/cm the distance where the magnetic field and the laser detuning cancel at $z \approx 3$ mm. This is significantly smaller than a typical vacuum cell, but the real significance is if a low velocity atom wanders away from the magnetic field center the Zeeman shift will shift the atom onto resonance with the appropriate laser pushing the atom back to the center of the MOT. This only happens when the atoms are near the center of the MOT.

The final consideration is when the Doppler shift and the Zeeman shift are both much larger than δ_l but approximately the same magnitude. This is the same principle behind the Zeeman slower [33] where atoms exiting a high temperature oven with very large velocities can be cooled in 1D. A significant difference between the Zeeman slower and the MOT is the number of cooling beams, because a Zeeman slower uses a single laser to slow the atoms in 1D. If Equation 2.45 was used instead of Equation 2.46 then the damping coefficient c would have the second order as the lowest order and would be proportional to δ.

Because of this higher order dependence a Zeeman slower's field is tailored to matched the Doppler shift of the atoms while they are slowed to maximize the scattering rate over the length of the Zeeman slower. In comparison c_{MOT} only assumes δ_+ is small to achieve damping. This make the MOT easier to operate and robust over a variety of operating conditions, however it involves more lasers.

Because there is a balance between the two laser beams there is also an optimal cooling trajectory in a MOT. For example if an atom starts too slow it will be sped up before it is slowed so the optimal trajectory is maintained as the atom is cooled toward

the center of the MOT fields (see Figure 2.9). For comparison, in a Zeeman slower atoms with a Doppler shift less than the current Zeeman shift will drift down the tube until the Doppler and Zeeman shifts are matched and at that point the atom will be captured by the slowing trajectory of the Zeeman slower.

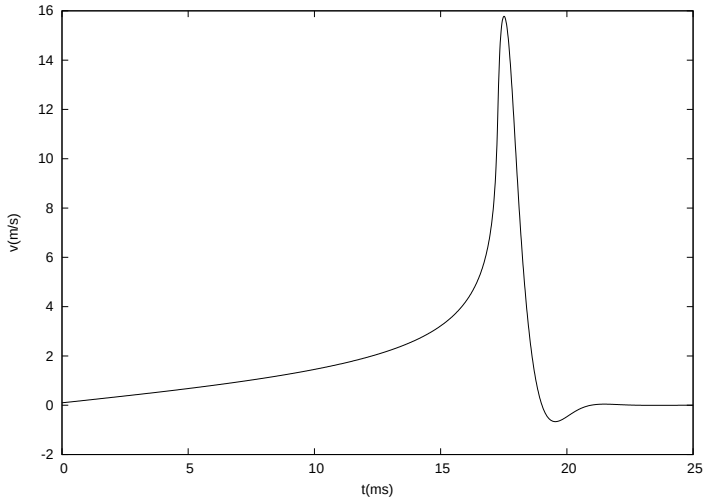

Figure 2.9: Numerical ODE calculation of the trajectory of an atom in a MOT starting at 0.1 m/s and the edge of the MOT. The 'atom' is centered in the laser beams with the velocity pointed at the zero of the magnetic field. This shows atoms with a low velocity will be sped up to match the optical forces until the laser forces are balanced.

In summary, there are two basic cooling mechanisms at play in a MOT depending on the relative magnitudes of δ_l and $\mathbf{k} \cdot \mathbf{v}$, and the position of the atoms in the MOT. If $\mathbf{k} \cdot \mathbf{v} \approx \delta_l$, $B \ll \delta_l$, and $z \ll 3$ mm then Doppler cooling is the dominant mechanism. If $\mathbf{k} \cdot \mathbf{v} \gg \delta_l$ and $z > 3$ mm then cooling takes place because of the Zeeman shift balances the Doppler shift. Actually MOT (Magneto-Optical Trap) does not describe these two processes and the cooling mechanisms can be divided into two regions: the Doppler region, and the Zeeman region. The relevance of these two regions to compact BEC systems is cooling parameters (especially the capture velocity) are related to the MOT loading efficiency. Specifically the cooling path length directly corresponds to the minimum size of the vacuum apparatus.

The above discussion was focused on cooling atoms from a room temperature

thermal distribution but once the atom has been slowed to a few m/s what is the lowest achievable temperature? When an atom is cooled by a laser it typically adsorbs a photon from the laser that is directed opposite it's velocity. Then the energy adsorbed by the atom is radiated away in a random direction. Averaged over many photons the momentum of the absorbed photons will have a net force in the direction of the laser. The momentum of the emitted photons will average to zero, but at any instant of time the emitted photons will impart a random momentum to the atom. This Brownian like heating is canceled in a MOT by the cooling mechanisms described above. The balance of the recoil heating rate and the low intensity Doppler cooling rate leads to the Doppler temperature $T_D = \hbar\Gamma/(2k_B)$ [34]. For ^{87}Rb $T_D = 143\mu$k corresponding to a velocity of 17 cm/s. This temperature is in agreement with the temperature of a reasonably optimized CMOT (see Section 4.4.5).

In the early days of MOTs the Doppler limit was a well known temperature limit but in initial laser cooling experiments the measured temperature was significantly lower than the Doppler limit [35]. This new cooling mechanism was called sub-Doppler cooling and worked by introducing a velocity dependent force dependent on the light shift due to the polarization of the light beams [36].

2.4.1.2 Trapping

After the atoms are cooled they need to be trapped and the MOT also performs this function. The trapping in a MOT is assumed to have the form $F = kx$ where k is the effective spring constant of the trap. Assume the atoms have been cooled below a few m/s so $\mathbf{k} \cdot \mathbf{v}$ can be ignored. The spring coefficient k can be calculated by Taylor expanding Equation 2.46 around $r \approx 0$ and dropping all terms other than the first order

$$k = \frac{d\mathbf{F}(r \approx 0)}{dx} = -\frac{\hbar\mathbf{k}^2\Gamma S}{\pi} \frac{16B_c\,\delta_l}{\left(1 + NS + 4\delta_l^2/\Gamma^2\right)^2} \tag{2.50}$$

where $B_c = \mu_m B'/\hbar$. If the typical MOT detuning $\delta_l = \Gamma$ is used then

$$k = -\frac{\hbar \mathbf{k}^2 S}{\pi} \frac{32 B_c}{(NS+17)^2}. \tag{2.51}$$

Thus atoms that have been cooled will feel a force toward the center of the magnetic field that is proportional to the magnetic field gradient. Increasing the magnetic field gradient will compress the atoms, a key element of a compressed MOT [37]. In practice the intensity of the optical fields will also determine the position of the MOT, but that anaylsis would require significantly more computational effort.

2.4.2 Chip versus six-beam MOTs

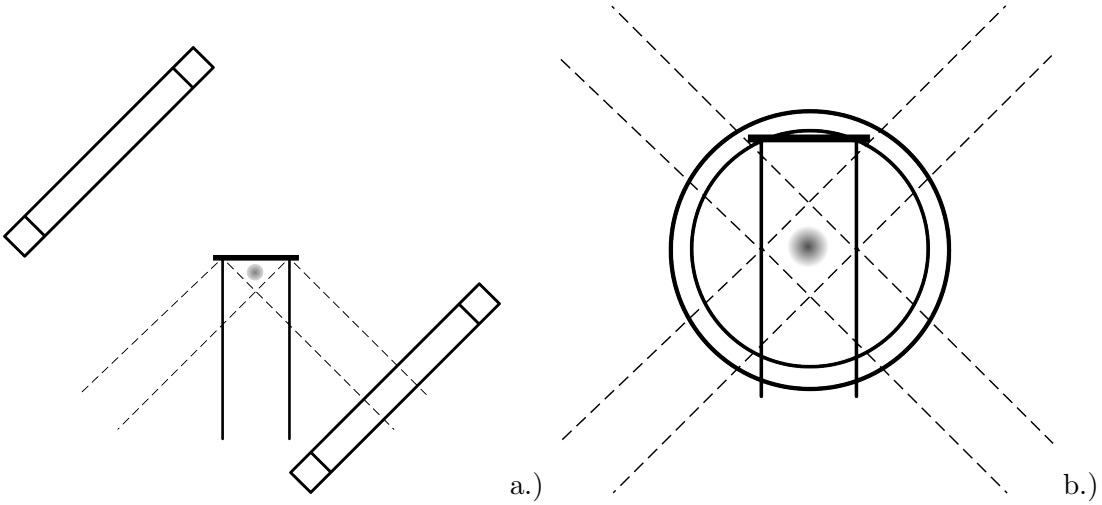

Figure 2.10: This show the reletive alignments and positions of the laser beams (dashed lines) with the cell and atom chip. Not shown are the 5th and 6th beams that would go in and out of the page. Also shown is the position of the coils needed to generate the MOT magnetic field. Figure a.) shows the configuration for a mirror MOT and Figure b.) shows the configuration of six beam MOT.

The first BEC on a chip experiment [1] and the first BEC on a chip experiment at CU [18] both used a mirror MOT to laser cool atoms close (1-2 mm) from the chip surface. Mirror MOTs were used for initial BEC on a chip experiments because it simplified the transfer to the chip magnetic trap. The details of a mirror MOT can be found in References [25, 14] but the basic configuration of a chip MOT are the lasers

beams are reflected off the surface of a chip to form a prism of light that creates a cooling force in all directions and the magnetic coils are rotated 45° to the plane of the chip (see Figure 2.10a). The essential characteristic of the mirror MOT is the ability to position the MOT close to the chip. Initially the mirror MOT position is moved away from the chip to capture a large number of atoms. After the atoms are gathered the cloud is compressed in a CMOT and brought close to the surface of the chip. Depending on the laser alignment the atoms can be brought to < 1 mm from the chip surface. The close proximity of the atoms to the chip surface makes it possible to magnetically trap the atoms with < 5 A of current on the chip.

A "U" shaped wire on the chip plus a bias field can also create a MOT magnetic field. This combination is called a chip mirror MOT and has the advantage of precisely positioning the MOT relative to the chip wires and mode matching the MOT to the magnetic trap. There are many variants to the chip mirror MOT that are explained in References [38, 39, 40].

While the benefits of the chip MOT are mode matching, proximity to the chip, precise alignment, and low power the significant trade-off is reduced MOT number because the stopping distance is effectively halved. The loss in MOT number is greater than a half because the MOT number is a strong function of the stopping distance of the atoms [32] and the stopping distance of the mirror MOT more than halved. Additionally the alignment of the laser fields depends on the mirror surface. Some configurations apply an insulated mirror directly over the trapping wires [25, 18] while other experiments etch fine lines in a gold or silver mirror surface to create an integrated mirrored atom chip. Both approaches have been used at CU, applying a mirror over a wire pattern is a straight forward procedure but requires careful processing. The mirror surface is typically attached with EpoTex 353 ND vacuum compatible epoxy that is degrades at the anodic bonding temperatures (> 400°C) so this process is not well suited to anodically bonded cells but is amenable to epoxied cells. The integrated

mirror does not involve epoxy so it is compatible with anodic bonding and works well for a mirror MOT away from the wire surface. However, when the atoms are moved close to the surface the optical field is significantly affected by the gaps in the mirror and the mirror MOT is degraded. The mirror MOT is sensitive to the cell alignment because the lasers are reflected off the chip surface so when the vacuum cell is changed the lasers must be carefully realigned to the new cell position. Another disadvantage of the mirror MOT is the MOT coils that are rotated by 45° relative to the cell. This results in an awkward balance of optical access, coil size, coil position, and cell size that typically results in a coil that is significantly larger than the cell (see Figure 2.10a). These same obervation were independently published in Reference [13] around the same time as the experiment in this thesis switched from a mirror MOT to a six-beam MOT.

2.4.3 Six-beam MOT

The more common configuration for making a MOT is the original six-beam MOT configuration [41] rotated 45° to fit under the chip (see Figure 2.10b). The pros and cons of using a six-beam MOT for chip based BEC experiment are almost exact opposites of the mirror MOT. The larger capture volume of the overlapped beams is able to capture 4-6 times the number of atoms, however the MOT is now an order of magnitude farther away from the chip. The chip mirror MOT was able to mode match the magnetic field of the mirror MOT to the chip Z-wire trap, however in the six beam MOT the tight axis of the MOT is perpendicular to the tight axis of the chip Z-wire. This can affect the direct transfer of atom into a chip Z-wire magnetic trap [13]. While the atoms from the chip CMOT could be magnetically trapped with < 5W, transporting an atom cloud to the chip requires 200–1,000 W of power to generate a high magnetic-field gradient in a large volume.

Using a six-beam MOT is advantageous because the chip processing is significantly relaxed and the alignment of the cell relative to the lasers is significantly easier because

the chip surface is not used as an optical surface. Not using the chip as a reflector also relaxes the chip requirements for anodic bonding. While the MOT alignment is easier the alignment of the transport magnetic trap requires additional optimization to efficiently couple atoms to the chip. Finally the MOT coil is an extra pair of bias coils configured as an anti-Helmholtz pair and mounted with the bias field coils. The extra space of the coils is minimal and improves optical access to the cell compared to the 45° mirror MOT coils (see Figure 2.10b).

2.4.4 Six-beam MOTs with angled beams

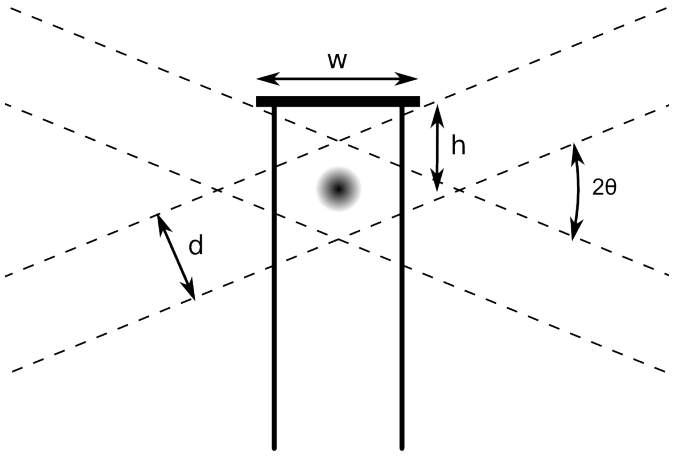

Figure 2.11: The angled six beam MOT configuration showing the factors that determine the distance from the atom chip to the center of the MOT.

As mentioned above a six-beam MOT is desirable option compared to a mirror MOT but one significant drawback is the distance of the atoms from the chip. Other cold atom groups have worked with transfer efficiencies of $\sim 15\%$ from their six-beam MOT to their chip magnetic trap [42, 43], with the highest transfer efficiency of $\sim 50\%$ [13]. In this thesis the atoms are magnetically transfered by a large Z-wire to improve mode matching to the chip. However the external Z-wire has a limited transport distance (< 2 cm). At the time it appeared that the Vuletic group at MIT used a relative beam angle other than 90° (see Figure 2.11) and that it would be possible to bring the atoms close

to the chip without reducing the beam size (i.e. MOT number). In actuality $\theta = 90°$ in the MIT experiment [44], but fortunately the idea of reducing the angle was still viable.

In an effort to improve the MOT loading efficiency Monte-Carlo (MC) simulations of MOTs in vapor cells were used to evaluate potential mirror MOT configurations (e.g. a 20 cm long wire plus bias field will make a long skinny mirror MOT unfortunately the number is small). This same MC simulation shows a MOT with angled beams is number stable until $< 20°$ (see Figure 2.12). This allows the MOT to be closer to the chip by a factor of 1.8-2 which significantly reduces the current required to transport the atoms to the chip.

A first it is surprising that the MOT is stable to such a shallow angle but considering a few relevant MOT parameters it is not surprising. Other MOT configurations have been successfully implemented with non-orthogonal beams [45], and as mentioned the mechanisms of cooling the atoms and the trapping the atoms can be considered separate processes. These steps have been separated from some of the earliest laser cooling experiments and are still in use today where the cooling is a 1D process (i.e. Zeeman slower) followed by trapping in a MOT [9] or a shallow magnetic trap [35]. An atom experiences a force of roughly 1,000 g during cooling so a shallow angle MOT should hold against gravity with $\theta < 1°$. Another consideration in a MOT is the depth of the trap potential after the atoms are cooled. It is somewhat hard to define a potential depth in an overdamped system but an atom must have a few K of energy to escape from a MOT [46] and the typical Doppler temperature is < 1 mK so it is possible for the beam angle to be reduced without reducing the MOT number. The other consideration is the size of the MOT due to photon reradiation but any loss from photon reradiation would be linked to the size of the beams which in the current case are made larger to collect more atoms out of the background.

What are the limits and mechanisms of the shallow angle MOT? The consistency of the MOT number over a wide range of angles can be attributed to the atom version

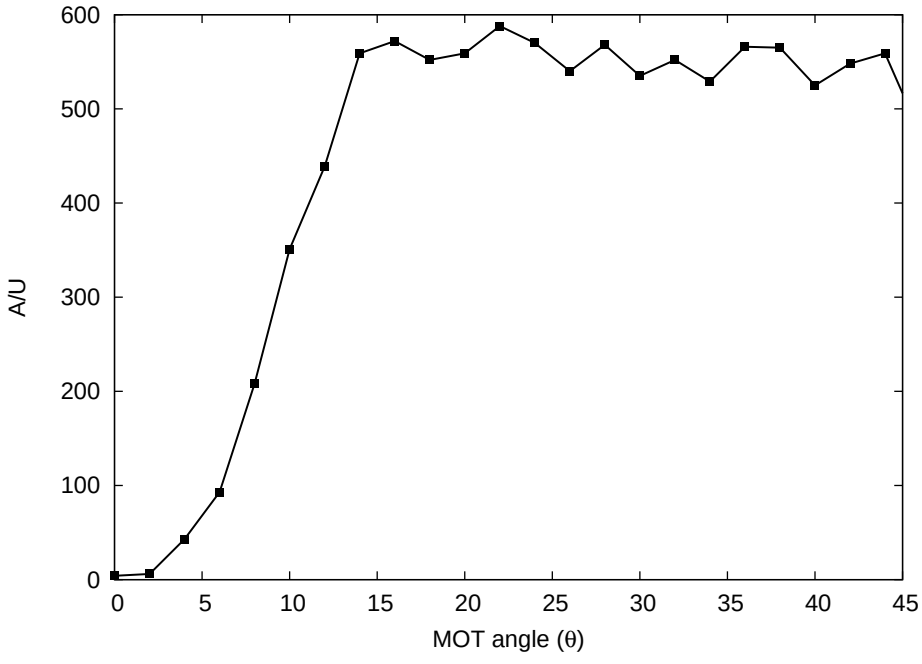

a.)

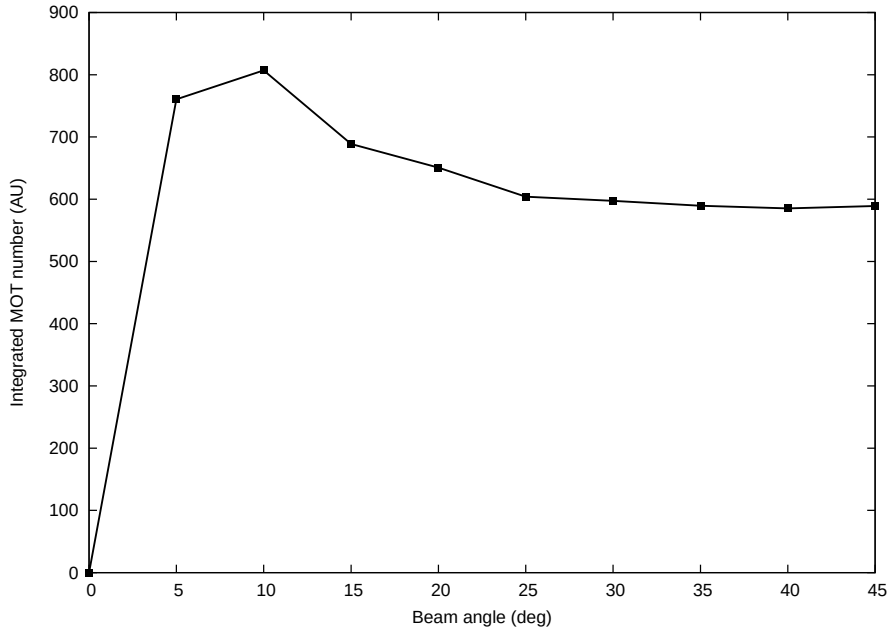

b.)

Figure 2.12: Simulations of MOT number versus the angle of the 3D MOT beams. Figure a shows a 3D calculation that includes the momentum kick from recoiling photons. It is interesting to note the MOT number is saturated up to $\theta \approx 20°$. Figure b shows a 2D numerical ODE calculation that does not take the photon recoil into consideration.

of Lambert's cosine law that the apparent brightness of a beam will be independent of angle if the scattering surface is perfectly random. This type of surface roughness is know as Lambertian roughness and the light scatting will have a $\cos(\theta)$ dependence that exactly cancels the change of viewing angle. From an atomistic point of view the randomness of an atom bouncing off a wall is described by the accommodation coefficient α. There are several sub-versions of α [47] but the simplest form is

$$\alpha \equiv \frac{E_i - E_f}{E_i - E_w} \tag{2.52}$$

where E_i is energy of the atom before hitting the wall, E_f is the energy of the atom after hitting the wall, and E_w is the energy of the wall. If the atom specularly reflects off of the wall then E_f will have some dependence on E_i and $\alpha < 1$, but if the atom has no dependence on the previous state then the wall will determine the state of the atom and $E_f = E_i$ and $\alpha = 1$. Atomic specular reflections are more probable when the atoms are light and/or non-interacting (e.g. helium or nitrogen) and $\alpha > 0.8$ for specular tending atoms incident on specially prepared surfaces. In most cases it is a good approximation to consider the walls of the vacuum chamber to be atomically Lambertian. In this approximation the angular distribution of atoms leaving the walls of the vacuum chamber has a $\cos(\theta)$ dependence where θ is measured relative to the wall normal.[1]

Figure 2.12b shows a calculation of MOT number assuming probablity of atoms coming off the wall has a $\cos(\theta)$. In this calculation the capture velocity is determined using a 2D numerical ODE solver ignoring the random recoil of the photon leaving the atom (see Appendix A for code). This calculation has a different curve then Figure 2.12a where a 3D MC was performed using the Verlet method to integrate the atom's trajectory [48]. This simulation included a random recoil force that would cause loss at lower MOT beam angles. Due to the difference in the simulations the photon recoil

[1] This is also the starting point for calculating the conductance of long pipes and such in the molecular flow regime.

appears to be the limiting factor that determines that minimum MOT beam angle that will support a large MOT.

2.4.5 2D MOT

A 2D MOT is more than just a high aspect ratio 3D MOT. In a 3D MOT the magnetic field gradient is truly 3D, but in a 2D MOT there is no magnetic field gradient along the longitudinal axis because of the symmetry of the four coil or magnet configuration. In a 3D MOT there must be lasers with some projection onto every axis in order to trap atoms. In a 2D MOT the lasers only propagate along two axes and leave the third axis with no optical or magnetic forces. Along the X and Y axes the 2D MOT can be considered 1D cooling so the projection of velocity will be cooled similar to Figure 2.9. Along the Z-axis there is no cooling and the Z-component of the velocity acquired when the atom left the wall will carry the atoms toward one end or another of the 2D MOT cell. In a slightly modified version of the 2D MOT an additional laser is propagated along the Z-axis of the 2D MOT. This laser does not provide confinement but rather molasses cooling along the unconfined axis creating what is called a 2D+ MOT. The velocity of atoms exiting a 2D+ MOT is significantly slower than the pure 2D MOT configuration [49].

The atoms in a 2D MOT are typically extracted from the 2D MOT chamber via an aperture. The length and width of the 2D MOT, the aperture diameter, and distance from the 2D MOT will determine the velocity distribution of atoms exiting the aperture. Specifically there is a cutoff velocity above which atoms will not be extracted from the 2D MOT where the maximum velocity is directly related to the diameter of the exit hole. This happens because atoms with greater longitudinal velocities will not spend as much time being cooled in the transverse direction. The variance in cooling determines the solid angle of the beam exiting the 2D MOT. At the same time atoms with higher angles will tend to be atoms with higher longitudinal velocities, so the exit

aperture of the 2D MOT cell can be used to filter high velocity atoms at the cost of total flux. Additionally the size of the aperture determines the pressure differential between the two systems. The velocity filtering depends on the solid angle so a small aperture directly after the end of the 2D MOT will limit vacuum conductance and still allow a high atom throughput.

The optimal aspect ratio of the 2D MOT cell depends if a 2D or a 2D+ MOT is used. For a 2D MOT a longer cell will allow more atoms to be captured and be used in the flux. If a 2D+ MOT is used a longer cell will allow the atoms more time in the center of the cell where the radiation imbalance will increase the atom velocity. The 2D+ MOT increases the capturable flux by a factor of 3-4 because the atoms are colder and the radiation pressure improves the aiming of the atom flux [49]. A 2D MOT is desirable over a 2D+ MOT when on axis light is an issue.

There are other configurations that can be used to produce a cold beam of atoms specifically Zeeman slowers [50], a 3D MOT with a hole in an optic (LVIS)[51], and a pyramid MOT with an open tip [52, 53]. Zeeman slowers tend to be long devices (> 30 cm) and need a counter propagating on-axis slowing laser. The LVIS configuration is a 3D MOT with a quarter waveplate and mirror mounted inside the vacuum chamber. The waveplate and mirror have a hole drilled in the center so the atom beam can be extracted from the MOT. From a practical device standpoint the pyramid MOT is the best option because only one laser is needed to provide cooling in all directions, however the 2D+ MOT has the largest capturable flux relative to the physical size and complexity.

2.5 Vacuum

In a compact BEC system a high performance vacuum system is a key element. Compared to larger BEC systems chip based BEC experiments operate at much higher pressures ($< 10^{-12}$ versus 10^{-9} torr). Even though the vacuum requirement is relaxed

Vacuum	Vacuum Units	Electical
Outgassing rate per area	[torr][ℓ]/[s]/[m^3]=[atoms]/[s]	Current
Pressure $\times$ Pumping speed	[torr][ℓ]/[s]=[atoms]/[s]	Current
Conductance	[ℓ]/[s]	1/Resistance
Pressure	[torr]= [atoms]/[m^3]	Voltage

Table 2.1: Comparison of vacuum to electrical parameters. The unit of torr will be used instead of using particles/volume.

the high surface area to volume ratio of small vacuum systems and isolating a region of high rubidium pressure ($\sim 10^{-7}$ torr) less than 10 cm from a low pressure BEC region ($\sim 10^{-9}$ torr) are important design considerations. The pressure in a multi-chamber vacuum system can be modeled as an electrical circuit with the various vacuum parameters directly correlating to electronic parameters (See Table 2.1).

The vacuum circuit analogy can be used to make order of magnitude estimates. For example, the pressure in the 2D MOT chamber is $\sim 10^{-7}$ torr (largely rubidium) and the pumping rate of the upper chamber is $\sim 4\,\ell$/s assuming $2\,\ell$/s pumping each from the ion pump and the rubidium sticking to the walls of the BEC region. Assuming the pressure in the BEC chamber is 10^{-9} torr then the conductance between the two chambers can determined using Ohm's law.

$$C = \frac{4\ell/s \times 10^{-9}\,\text{torr}}{10^{-7}\,\text{torr}} \tag{2.53}$$

$$= 4 \times 10^{-2}\,\ell/\text{s}. \tag{2.54}$$

Assuming a plate thickness of $l = 1$ mm what diameter hole will achieve this pumping speed? From $C = 12d^3/l$ [54, 55] then $d \approx 0.7$ mm. This is slightly smaller than the acutal size of the pinhole used in the final two chamber design (see Section 4.1).

The electronic circuit analogy can be extended to more complicated systems. There is one difference that is worth mentioning, while most electronic devices are thought of as fundamentally constant voltage devices while most UHV systems are fundamentally constant current devices. Specifically outgassing from the walls is the

major contributor in UHV systems. This outgassing rate (current) is independent of the local vacuum pressure or conductances so the walls of a vacuum system should be modeled as constant current sources. These calculations can be performed using the method of Reference [56]. A key parameter in these calculations is the wall outgassing rate. The outgassing rate of glasses and silicon are dependent on the preparation and it is difficult to find similar conditions bakeout conditions (300° for weeks) in the literature [57, 58], but it may be assumed the outgassing rate is comparable to metals with similar vacuum preparation ($\leq 10^{-9}$ torr $\ell/s/cm^2$).

2.6 BEC

The essential characteristics in the formation of a BEC can be understood using the DeBroglie wave model (fuzzy balls in a jar). The formation of a BEC can also be understood from the level occupation and Bosonic stimulation picture. This quantum model is used in References [59, 60] to evaluate evaporation trajectories and is a reasonable explanation of the quantum formation of a BEC.

The DeBroglie wave model assumes atoms are wavelike object where the wavelength of the atom is proportional to the inverse of the atom's momentum

$$\lambda_{DB} = \frac{h}{mv} \tag{2.55}$$

where h is Plank's constant, m is the mass of the atom, and v is the atomic velocity. This is of course without relativistic corrections because the velocities are significantly less than the speed of light. As the velocity of the atoms decreases via cooling the effective size of the atom (i.e. wavefunction) increases and can become significantly larger than the physical size of the atom. Often the cartoon picture shows atoms initially as point particles and as the temperature drops the points become little waves that are increasingly larger as the temperature drops [61]. But the atoms are 3D objects and cold atoms can be thought of as fuzzy balls that don't have well defined boundary

much like a wavefunction, but can still be described by an effective radius. Because atoms are trapped in a 3D trap for most operations performed on a BEC the atoms can be thought of being placed in a container with volume V_c filled with N atoms.

A Bose-Einstein condensate forms because Bosons are indistinguishable particles [62] and if the spacing between two Bosons is smaller than λ_{DB} of the individual Bosons then the two particles will occupy the same space and appear to be a single particle. Invoking the fuzzy ball picture the volume occupied by the balls is $V_{DB} \sim N\lambda_{DB}^3$. If there are enough atoms at a cold enough temperature then $V_{DB} > V_c$. All of the fuzzy balls will overlap inside the jar and be indistinguishable thus forming a condensate. The key result of this analysis is that to form a BEC the atoms need to be more than just cold. The atoms also need to have a high density. The combination of high atomic density **a**nd large wavefunction (i.e. low temperature) lead to BEC.

The concept of total wavefunction volume versus the confining volume is called the phase space density (PSD)

$$PSD = n\Lambda_{DB}^3 \tag{2.56}$$

where n is the density of atoms in the trap and Λ_{DB} is the thermal deBroglie wavelength. A more rigorous derivation [63] shows a condensate is formed when the PSD$\geq$ 2.61.

2.7 Evaporative cooling

As explained in the previous section a BEC is formed when there is a high atom density and the atoms are cold. Current laser cooling techniques cannot cool atoms at a high density, because at high densities a photon in the center of the cloud may recoil with several atoms as exits the cloud. This outward photon pressure prevents high densities at low temperatures. Laser cooling is key step toward BEC but must be followed by another cooling mechanism to achieve BEC.

Evaporative or forced evaporative cooling is based on selectively removing a few

of the hottest atoms from the Maxwell-Boltzmann (MB) distribution. As seen in Figure 2.13a the product of energy ($\propto v^2$) and the MB distribution shows the fraction of the total energy in the cloud is shifted toward the highest energy atoms. By removing a few atoms from the high energy tail of the MB distribution a significant portion of the energy in the cloud can be removed with minimal atom loss.

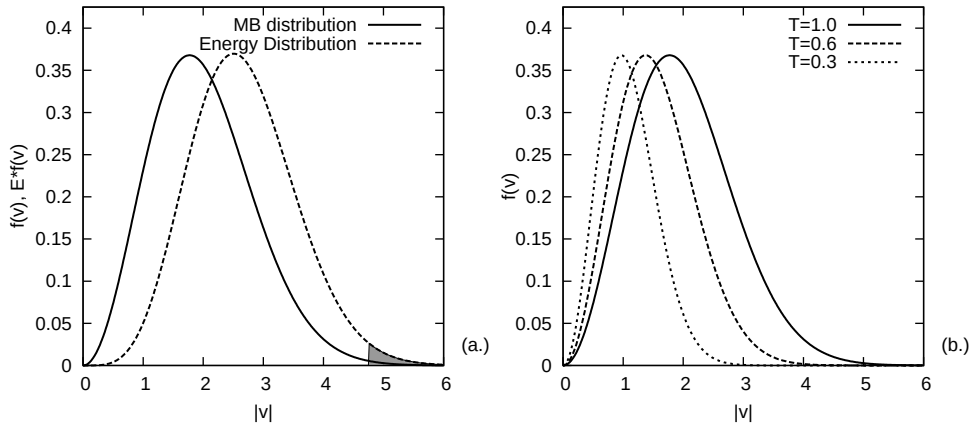

Figure 2.13: Maxwell-Boltzmann velocity distributions and energy distribution. The shaded area in Figure a.) shows how a significant portion of the total energy can be removed from an atom cloud without large number loss by evaporating on tail of the distribution. Figure b.) shows various distributions for various relative temperatures.

The atom distribution is truncated by removing the hottest atoms but the peak velocity of the cloud is the same. Removing more atoms from the high energy tail of the MB distribution will remove more energy at the cost of significantly more atoms. However is a few high energy atoms are removed and the remaining atoms are allowed to redistribute their energy and smooth out the velocity distribution the peak velocity of the cloud will drop (see Figure 2.13b). The dynamics of the redistribution of energy is described by the Boltzmann transport equation [63] and knowing the energy levels of a trap and the initial energy distribution the details of evaporative cooling trajectory can be numerically solved [64]. While this numerical analysis can predict the number, temperature, etc. of an atom cloud as it is evaporated Monte Carlo models showed a truncated MB distribution would essentially rethermalize if each atom on average

underwent three collisions [65]. From an experimental point of view the thermalization time can be calculated from the classical collision rate

$$\tau_{col} = n\, v_{rel}\, \sigma \tag{2.57}$$

where n is the atomic density, v_{rel} is the relative velocity of the atoms, and σ is the cross section of the atom. This equation is directly related to the mean free path, monolayer formation time, and other common high vacuum parameters [54].

To maintain the high energy tail of the MB distribution the rate of evaporation τ_{evap} should not be faster than the rethermalization rate or the evaporation will be inefficient. So in general

$$\tau_{evap} < 3\,\tau_{col} \tag{2.58}$$

but τ_{col} can increase or decrease during evaporation depending on several considerations. If there is little atom loss as the atoms are cooled the atomic density will increase as the atoms settle into the bottom of the trap. The physical size of atoms in a trap (e.g. linear or harmonic) will occupy less volume at lower temperatures than at higher temperatures simply because the less energy the atoms have the less the atoms will push against the spring constant of the trap. Again that assumes the relative low atom number loss. This effect of increasing density and collision rate, even as the total number decreases, is called runaway evaporation and is a key requirement for BEC production [65].

If there is a loss mechanism, other than evaporating only the hot atoms, it is possible that after evaporating for some time the density of the atom cloud will decrease. In this case τ_{col} will drop and will continue to drop because the parasitic atom loss rate is greater than the gains made by cooling the atom cloud. In most BEC experiments the dominant loss mechanisms are collisions with background thermal atoms (i.e. vacuum pressure), resonant light scattering, and at high densities three-body loss [6]. Of these mechanisms vacuum loss is ubiquitous in BEC experiments and the most significant in compact BEC systems. The minimum requirement is $\tau_{vac} < \tau_{evap}$ for runaway evapora-

tion and for optimal performance $\tau_{vac} \ll \tau_{col}$ so the only significant source of atom loss is forced evaporation.

Using chip based BEC systems relaxes the vacuum requirement compared to non-chip BEC experiments by trapping the atoms in a tightly compressed magnetic trap. Tight trap compression increases τ_{col} because compressing a gas will increase n and the overall temperature of the cloud or v_{rel}. If the compression is adiabatic then the PSD will not change but the collision rate will increase allowing faster evaporation (see Equation 2.57). The trap compression is proportional to effective trap frequency because a high trap frequency is a result of a tighter trap. See Table 2.2 for a comparison of chip based versus more traditional BEC machines.

	Typical	Compact
τ_{vac}(s)	∼100	∼10
$\bar{\omega}_{\perp}(Hz)$	∼100	∼1,000
N_{MOT}	$10^9 - 10^{10}$	$10^7 - 10^8$
T_{RF}(s)	~ 50	1-4

Table 2.2: Comparison of evaporation parameters (e.g. evaporation time) for chip based and traditional BEC machines.

2.7.1 Evaporation trajectories

Optimizing BEC number and production largely falls into three main categories: initial number, vacuum lifetime, and evaporation trajectory. This section will cover the evaporation trajectory as the first two are covered in previous sections. As mentioned in the previous section the rate at which atoms can be evaporated off the tail of the MB distribution depends on how quickly the atoms thermalize or the inter-atomic collision rate. The collision rate depends on n and v_{rel} and as the atoms are evaporated N and v_{rel} both drop but because the atoms are in a linear or harmonic trap the effective volume V_{eff} decreases at the same rate or faster than the decrease in N and V_{rel} so the collision rate is maintained.

Optimizing the evaporation trajectory starts by assuming the atom cloud energy distribution is close to equilibrium and that some fraction of the atoms are evaporated from the MB distribution tail. The fraction to evaporate is choosen to maximize the largest energy loss while minimizing number loss. After the fraction to evaporate has been determined the fraction is converted into the appropriate loss mechanism: change in RF frequency for RF evaporation, decrease in laser intensity for optical evaporation [11], or distance from hard surface for surface evaporation [66]. It has been shown that optimizing each fractional evaporation step will optimize the whole evaporation trajectory [67]. Several optimized evaporation trajectories have been published [68, 69, 67] and a simple evaporative model that can be used for a qualitative understanding of the evaporative process [65]. These models are largely semi-classical and do not take into account Bosonic stimulation at the end of the evaporative trajectory. From these models the optimal evaporation trajectory is an exponentially decreasing energy truncation.

Recently an evaporation trajectory was calculated taking into account the Bosonic stimulation of the atoms especially towards the end of the evaporation when the ground state begins to have a significant population [60]. At this point in the evaporation trajectory any two atoms that scatter will have final states that are significantly affected by Bosonic stimulation. One of the atoms will scatter into the ground state and the other atom will receive the excess energy and will be evaporated. The cloud's overall temperature will drop at an accelerated rate as the condensate forms. This evaporation has two essential trajectories: an initial exponential sweep to a point where $PSD \sim 10^{-1}$ and then a rapid linear sweep to just above the trap bottom that sweeps the atoms into the ground state. This method improves the final number in the BEC by avoiding vacuum related losses of a longer evaporation trajectory.

As mentioned once a BEC begins to form it dramatically changes the behavior of the system, this similar to a laser at threshold. As the laser pump is increased above

threshold a single mode becomes dominant due to cavity selectivity. This dominant mode will pull gain from other potential modes and will result in a macroscopic occupation of a single mode. The behavior of a BEC is similar, once a small condensate is formed Bose statistics rapidly enhances the state with the largest occupation. In the case of a BEC the only state that can easily have a macroscopic occupation is the ground state of the magnetic trap where in an optical cavity the dominant mode is determined by cavity mode with best gain/loss ratio.

In the experiment described in this thesis linear evaporation sweeps are used instead of exponential sweeps. Linear sweeps have been successfully used to achieve BEC in other experiments [13]. While the exponential sweep is the most efficient trajectory an optimized linear trajectory can also achieve BEC as long as the runaway evaporation condition is met, especially at the end of the evaporative cooling. This can easily be achieved if the initial atom number is large so there is a reasonable number at atoms in the final stage of the magnetic trap and the trap frequency is high so the thermalization rate is high enough to be efficient over a large range of time scales. Typically there are two linear evaporation stages; The first stage cools the atom cloud with higher atom loss compared to an exponential trajectory, but still maintains a reasonable collision rate. The final linear evaporation stage is optimized to maintain the collision rate of the 1st sweep though the final linear sweep thus maintaining the runaway evaporation condition to achieve BEC.

Chapter 3

Au_xRb dispensers

In 2003 CU collaborated with Sarnoff Corporation on improving cold atom technologies. One of Sarnoff efforts was an enriched ^{87}Rb dispenser using a gold/rubidium alloy. As will be explained pure rubidium can be evolved from a gold/rubidium alloy by simply heating the alloy. Sarnoff made dispensers by mixing liquid rubidium and powdered gold and then pressing the mixture in a mold to form pellets. The alloy was stable in air because the gold and rubidium formed a stable alloy. When the pellets were heated in a vacuum rubidium was released because of its higher vapor pressure. At the same time other groups also used gold used to dispense alkali metals but under significantly different circumstances [70].

Around the same time a CU Mechanical Engineering student was integrating MicroElectro-Mechanical System (MEMS) into cold physics experiments [71]. In one of the cold atom MEMS devices were little magnetic coils (< 1 mm^2) made by patterning a gold wires on silicon. When the coils were energized in vacuum with a resonant laser shining though the cell a brief puff of fluorescence could be seen around the coils. It was soon realized how little power was used by the MEMS device and also how quickly the rubidium pressure was modulated. At the time anodically bonded cells were just beginning to be used and rapidly rubidium dispensing without UV light was an open question. Rapid rubidium dispensing from a thin gold wire appeared to be a potential solution. After several tests it was determined that the rubidium partial pressure did

not recover fast enough to be useful for rapid BEC production, however the technique and results are worth documenting for future dispensing needs.

3.1 Binary phase diagrams and vapor pressures

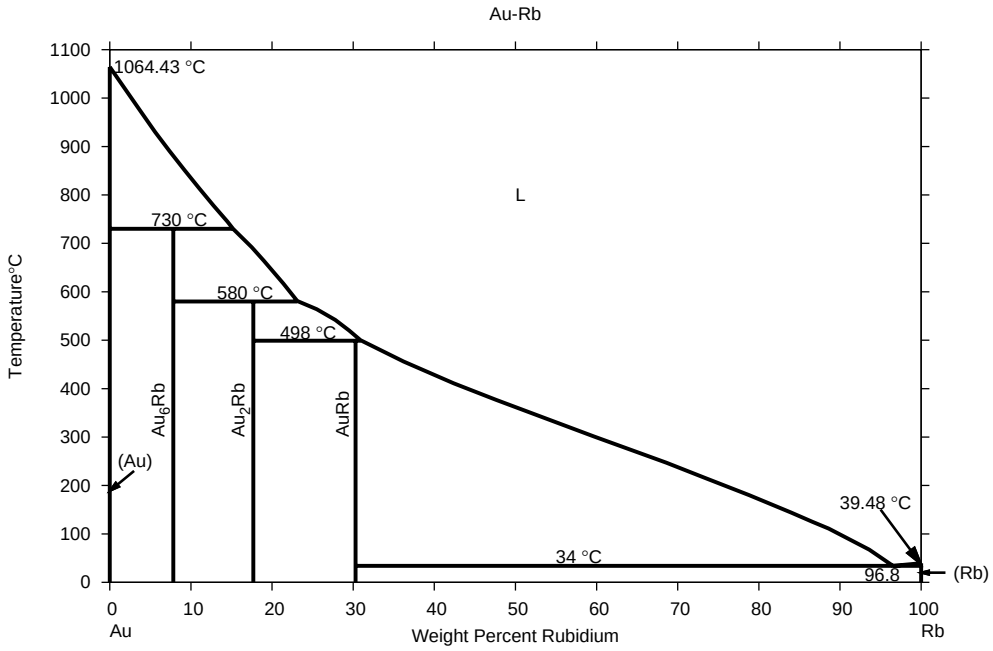

Figure 3.1: The binary phase diagram of gold and rubidium [72].

Phase diagrams are a pictoral representations of the properties of a material as a function of temperature, pressure, composition, etc. Specifically binary phase diagrams represent the alloys, melting temperatures, and crystal phases of a two elements as a function of the composition and the temperature (see Figure 3.1 for the phase diagram of gold and rubidium).

As seen on the left hand side of Figure 3.1 there is pure gold and as more rubidium is added to the gold an alloy of gold and rubidium is formed. If the percentage of rubidium by weight increases beyond $\sim 30\%$ then an alloy is no longer formed and the two materials will coexist in mixture but will not be alloyed.

If pure rubidium is placed in a UHV chamber the partial pressure of rubidium

will typically be 10^{-7} torr which is significantly higher than the pressure required for making BEC (even on a chip). In physical chemistry Raoult's and/or Henry's Law describes the behavior of a solution composed of a low vapor pressure solvent (gold) and a low concentration of a high vapor pressure solute (rubidium). In this case the vapor pressure of the solute will be suppressed by the solvent. Because of Henry's Law the vapor pressure of rubidium in a gold alloy is suppressed so the net vapor pressure of the gold/rubidium alloy is sufficiently low to be compatible with producing BEC.

To dispense the rubidium from the gold the alloy should be heated to the approximately to the temperature where the gold is still a solid but the rubidium has started to liquefy. This is called the $L + \alpha$ phase where part of the phase is liquefied and the other is still solid, in this case the α constituent (gold) has the higher melting temperature. For example in Figure 3.1 at 10% rubidium the alloy will transition from a solid to the $L + \alpha$ phase at 580°C. Above this temperature the partial pressure of rubidium will increase because of the phase change and the rubidium is be dispensed from the alloy. No gold will be dispensensed at < 1000°C because the vapor pressure of gold is significantly lower than than rubidium's, especially below the melting point of pure gold.

3.2 Rapid dispensing

One crucial element in small BEC cell type system is quickly (< 1 s) modulating the partial pressure of rubidium. It is important for the alloy to rapidly cool below the dispensing point to reduce the overall vacuum pressure to a point suitable for BEC production. Most of the cooling happens via radiative loss because the alloy and heating element are in a vacuum with poor thermal conduction to the ambient temperature though thin wires. Determine what wire configurations will have the most rapid wire cooling for rapid rubidium pressure modulation.

3.3 Radiative heat loss

Assume at the temperatures for rubidium dispensing the significant heat loss mechanism is radiative heat transfer. The heat loss of a system due to radiation is

$$\frac{dQ}{dt} = \sigma \epsilon A \left(T^4 - T_{RT}^4\right) \tag{3.1}$$

where σ is the Stefan-Boltzmann constant, ϵ is the emissivity of the surface, and A is the total surface area. The total heat in a system is

$$Q = c\, m\, T \tag{3.2}$$

where c is the specific heat of the material and m is the mass of the object. Combining Equations 3.1 and 3.2 the change in temperature of a system is

$$\frac{dT}{dt} = \frac{\sigma \epsilon A}{c\, m} \left(T^4 - T_{RT}^4\right) \tag{3.3}$$

This can be simplified in the case of a round wire by replacing $A = 2\pi r l$ and $m = \rho \pi r^2 l$, where r is the radius of the wire, l is the length of the wire, and ρ is the mass density. Equation 3.3 becomes

$$\frac{dT}{dt} = \frac{2\sigma \epsilon}{c\, \rho\, r} \left(T^4 - T_{RT}^4\right). \tag{3.4}$$

There is no simple solution to Equation 3.4, but assume $T^4 \gg T_{RT}^4$ so the approximate solution to Equation 3.4 is

$$T(t) \approx \frac{1}{\sqrt[3]{\frac{6\,\sigma\,\epsilon}{c\,\rho\,r}\, t + T_0^{-3}}} \tag{3.5}$$

The only geometrical factor that comes into play is the radius of the wire. The emissivity can be increased by making the surface as rough as possible especially when using a noble metal like gold. The other parameter that can be somewhat varied is the material dependent factor $c\,\rho$ (see Table 3.1). Choosing the right material will improve the cooling rate, but less than a factor two. Tungsten is assumed in all the calculations because it is readily available, strong, and has a high melting temperature (3680 K).

Material	$c(J/g/C)$	$\rho(g/cc)$	$\rho\, c$
Ti	0.523	4.5	2.35
Al	0.897	2.7	2.42
Ag	0.235	10.5	2.46
Au	0.129	19.3	2.49
W	0.132	19.3	2.55
Mo	0.272	10.2	2.77
Pt	0.133	21.4	2.85
Pd	0.24	12	2.88
Cr	0.45	7.19	3.24
Cu	0.385	8.96	3.45
NiCr	0.414	8.4	3.48
Fe	0.449	7.86	3.53
SS	0.5	7.7	3.85
Ni	0.44	8.9	3.92

Table 3.1: Specific heat and mass density of a variety of materials. Sorted by $\rho\, c$ smallest to largest, or most desirable to least desirable for rapid cooling.

3.4 Optimal wire radius

Using Equation 3.5 solve for the required wire radius given a cooling time. The radius for a given cooling time, initial temperature, and final temperature is

$$r \approx 6\frac{\epsilon\,\sigma\,t}{\rho\, c}\,\frac{T_f^3\,T_0^3}{T_0^3 - T_f^3} \tag{3.6}$$

Assume a 1 s cooling time and a tungsten filament. What radius is required to cool from 10% above the $L + \alpha$ phase to 20% below the phase? This will give a relative estimate of what would be required to strongly modulate the Rubidium pressure in the cell. Table 3.2 shows the wire diameters to cool from the three gold/rubidium phases. The wire diameter is small but still reasonable.

3.5 Other geometries

As seen in Equation 3.3 the heating rate is largely affected by the ratio of mass to surface area and a round wire actually has the worst ratio of mass to surface area.

$T_p(C)$	$d(\mu m)$
730	22
580	14
496	10

Table 3.2: Calculated radius to achieve cooling in 1 s from 10% above to 20% below the $L + \alpha$ phase assuming Tungsten filament for the three gold/rubidium alloys.

3.5.1 Mesh

A wire mesh has a large surface area, but if the wires in the mesh are round there is actually no gain in the surface area to mass ratio over a long wire with the same radius. There is a small loss also because the active area is reduced where the wires touch. Otherwise the mass to surface area is the same as a long wire of the same radius. The potential benefit of mesh is greater structural strength, and in general thinner wires are found in mesh or Litz type wire, so a fast cooling rate may possibly be obtained without sacrificing structural integrity.

3.5.2 Foil

A flat wire is an easy to fabricate structure with a large surface area and small mass. Define the aspect ratio as $\alpha = h/w$ where h is the height of the wire and w is the width of the wire. Now with $A = 2w(1+\alpha)\,l$ and $m = \rho\,\alpha\,w^2\,l$ Equation 3.3 becomes

$$\frac{dT}{dt} = \frac{2(1+\alpha)\,\sigma\epsilon}{\rho\,\alpha\,w\,c}\left(T^4 - T_{RT}^4\right). \tag{3.7}$$

The wire width as a function of cooling time assuming $T \gg T_{RT}$ is

$$w \approx 6\frac{\epsilon\,\sigma(1+\alpha)\,t}{\rho\,\alpha\,w\,c}\,\frac{T_f^3\,T_0^3}{T_0^3 - T_f^3}. \tag{3.8}$$

See Table 3.3 for what wire width is required for a 1 s cooling time assuming $\alpha = 0.1$ and Tungsten wire. There is an approximate factor of 10 improvement for a given wire thickness. This improvement factor can be used to decrease the cooling time, expand the cooling rate, or use a more robust wire.

$T_p(C)$	$w(\mu m)$
730	123
580	76
496	56

Table 3.3: Calculated wire width to achieve cooling in 1 s from 10% above to 20% below the $L+\alpha$ phase assuming Tungsten filament for the three gold/rubidium alloys. Assume a 10:1 height to width aspect ratio.

3.6 Readsorption

Another factor to consider is the readsorption of the radiated energy. Any emitted radiation should have a direct line of sight to the walls of the chamber. The effective area will be reduced by the any parts that face each other. The magnitude of the effect may be determined by multiplying the interfacing areas by the emissivity. If the surface has a low emissivity it also means the same surface has a high reflectivity, so there is still a chance for the radiation to be adsorbed by the walls even if it hits part of the wire or foil first.

3.7 Bulk versus surface effects

The long term operation of a gold/rubidium dispenser depended if the interaction of gold and rubidium was a surface or bulk effect over the time scale of a few hours. Based on the behavior of the bulk Sarnoff dispenser the diffusion rate would need to be high to explain the dispenser behavior, so several experiments were performed to determine the diffusion rate of rubidium into a gold surface on the time scale of a few hours. The basic experimental setup is a thin piece of gold coated Nichrome in a glass vacuum chamber with a rubidium dispenser. The process of activating the dispenser (4-5 A for 2-3 mins 3-5x) deposits an unknown amount of rubidium on the gold. After the dispenser was activated the gold is heated for a few hours to remove any rubidium deposited on the gold. The process of heating the gold does not completely remove the

rubidium but sufficiently cleans the gold surface to mimic typical operating conditions.

The time evolution of the gold/rubidium dispenser is determined by measuring the absorption of a resonant laser though the glass cell. The laser beam is swept over Doppler broadened ^{85}Rb peaks and the signal measured by a photodiode is sent into a lock-in amplifier. The absorption was not calibrated to an absolute pressure for this experiment because the qualitative effects of surface or bulk effects could be determined by the shape of the rubidium dispensing curve. The scanning range of the laser (New Focus Vortex 780.24 nm) drifted slightly over the course of an hour and the drift was manually corrected every ~ 10 minutes.

The experiment starts by coating the surface of the gold with a layer of rubidium by heating the SAES rubidium dispenser. The amount of rubidium deposited on the gold is qualitatively monitored via the absorption signal from the laser passing through the cell. The rubidium is allowed to diffuse into the gold by waiting for some amount of time typically less than two hours because the dispenser reload time should be significantly less than two hours for reasonable operating conditions. In some experiments the gold and rubidium are heated to increase the diffusion rate of rubidium into the gold. Heating will also increase the vapor pressure of the rubidium on the surface of the gold but assuming the diffusion rate is higher than the increased loss then more rubidium will be diffused into the gold.

The amount of rubidium diffused into the gold can be qualitatively assessed assuming there are two regimes of rubidium dispensing when the gold and rubidium are heated by running current though the nichrome foil. First assume a thin layer of rubidium will be sorbed onto the surface of the gold. This surface layer will produce an initial spike of rubidium that is rapidly evaporated off the surface with an exponential decay. After this rapid spike and decay of surface rubidium the diffused rubidium would then dominate the dispensing. This diffusion based dispenser should have a characteristic $\sqrt{t}$ dependence of a typical diffusion process. The transition between the surface and

diffused rubidium would have a change in slope and in extreme cases a knee when all of the surface rubidium was expelled [73, 74]. Varying the diffusion time and/or the diffusion temperature would lead to an effective diffusion rate for the given gold area and thickness.

All of the result from the diffusion experiments appeared to have a single curve and did not display the two regimes of operation for diffusion times of several hours. Experiments when the gold is slightly heated reduced the total amount of rubidium dispensed from the gold including the brief burst of rubidium from the surface layer. No rubidium is detectable if the gold was heated too much ($\sim$50% dispensing current) during the gold coating phase.

The qualitative room temperature results indicate significant diffusion of rubidium into gold takes places on a time scale longer than several hours. The heated results indicate the effective time rubidium spends on the surfaces of heated gold is significantly less than the time required to diffuse into the bulk of the gold. While this method for determing diffusion rates is in principle reliable the diffusion rate of rubidium in gold is short compared to the desired experimental time scale. For short term diffusion rate other methods (i.e. sputter Auger spectrocopy [75]) could be used). After these results it was assumed diffusion did not play a significant role in reloadable rubidium dispensers and the surface effect would be the dominant dispensing mechanism.

3.7.1 Gold pulsing

Based on the results of Reference [71] it appeared that a rubidium dispenser could be made with a dispensing time constant of $\sim$ 1 s. The pulsed operation of a gold/rubidium dispenser is tested in using the same experimental setup as the gold/rubidium diffusion experiment. In a typical pulsed experiment the gold is coated with rubidium using the same process as the diffusion experiment. The gold coated tungsten foil is then heated by a pulse of current. The rubidium pressure rise and decay

are monitored by the absorption of a laser passed though the cell. Immediately after the gold is coated with rubidium a low current pulse increases the rubidium partial pressure as high as $\sim 3 \times 10^{-8}$ torr (see Figure 3.2. As the dispenser is pulsed the rubidium is depleted such that longer pulses or higher currents are needed to obtain the same pressure modulation. The gold is quickly reloaded with rubidium by heating a SAES rubidium dispenser to 4.5 A for 5 minutes and then letting the pressure recover for 15-20 minutes.

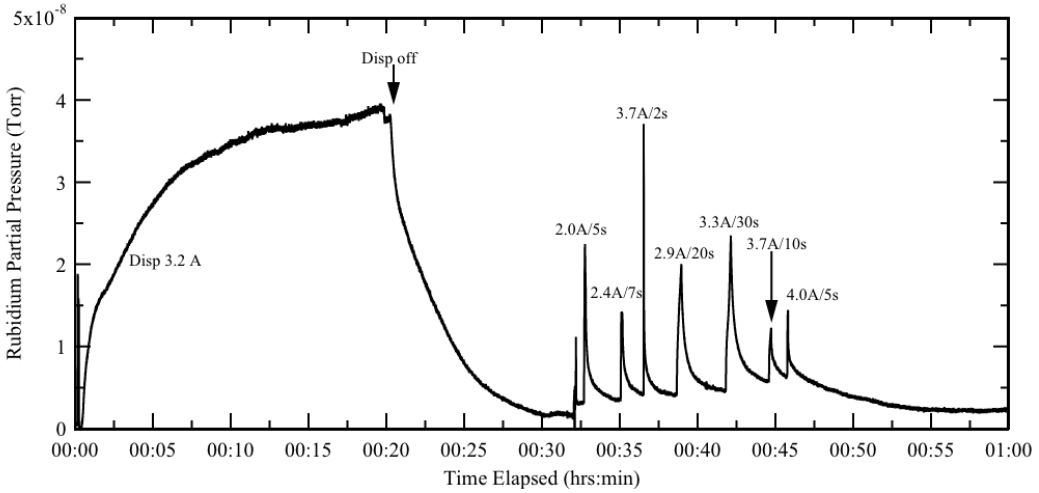

Figure 3.2: This shows pulsed rubidium dispensing from a gold coated Nichrome foil. This is data of a typical data run with gold evaporated on a Nichrome foil ($50 - 100\,\mu$m thick and an area of 5×15 mm). The foil is heated with a square pulse of current (labeled on each pulse) and as the rubidium is depleted from the gold higher currents longer pulses are needed to achieve the same pressure modulation.

As seen in Figure 3.2 typical pulses are a few amps at 1-5 s. The pulses decay time constant is a few seconds and the rubidium pressure significantly dropped on the order of 10 s. From this experiment modulating the rubidium pressure by rapidly heating a gold coated foil appears to have all of the right characteristics for a BEC compatible rubidium dispenser: a time constant of a few seconds, the pressure dropped significantly in $\sim$10 s, 10-20 pulses without reloading the gold, and a fast method for reloading the dispenser with rubidium.

3.8 MOTs and Au/Rb dispensers

While the gold and rubidium experiment using laser absorption to measure the transient response of the gold/rubidium dispensers the true test was putting a gold/ rubidium dispenser in a cold atom experiment. The first test used a gold coated (evaporated on both sides) stainless steel mesh about 1×5 cm long in a square glass cell with a plain piece of silicon anodically bonded to the top of the cell. The rubidium dispenser was activated before the vacuum cell was pinched off from the vacuum station so the gold was already exposed to rubidium. The MOT beams were aligned with the rubidium dispenser at a few amps and was then turned off to allow the vacuum to recover. The gold mesh was then pulsed for ~ 1 s at an experimentally determined current and the MOT number immediately increased. A few seconds after pulsing the mesh the MOT was emptied and the MOT loading rate was measured repeatedly over several minutes. In UV light induced desorption experiments a few seconds was enough time for the rubidium pressure to drop by an order of magnitude. However, with a gold coated mesh it took on the order of a half hour for the rubidium pressure to drop by an order of magnitude. There were multiple hypothesis as to exactly why the recovery time was so long but they all pointed to the large gold surface area of the wire mesh.

Several MOT based test were performed with gold coated $20 - 40\,\mu$m Nichrome foils that were 3-5 mm in width and 10-15 mm in length. The surface area and thermal mass of the Nichrome foils were significantly less than the gold coated mesh. The rubidium pressure modulation using the foils was faster than the gold mesh but the rubidium pressure recovery still took 10s of seconds to minutes. Additionally because of the a smaller surface area and faster pulsing the maximum number loaded into the MOT significantly dropped.

In another experiment an atom chip with electroplated gold wires was used in a mirror MOT configuration. When the external mirror MOT was transfered to the

chip mirror MOT a puff of rubidium was visible around the chip because rubidium was dispensed from the trapping wires on the chip. The possibility of using a gold coated atom chip as a rubidium dispenser was explored but the chip must also be used to magnetically trap the atoms and the resulting lifetime was too short ($\ll 1$ s) to produce BEC.

3.8.1 MOT N versus τ

As explained in Section 2.7 an important metric in evaluating potential feasibility of a compact BEC system is sufficient atoms to maintain collision rate and a long lifetime to avoid density loss. Over a reasonable range low atom number can be directly compensated by a longer lifetime and vice-versa. This balance of number and vacuum lifetime is called Nτ. Instead of using a mirror MOT and a SAES dispenser with a low Nτ a six-beam MOT and a gold/rubidium dispenser were used to increase both N and τ. While the six-beam MOT loaded more atoms the long vacuum lifetime using the gold/rubidium dispenser was critical because the magnetic trap is more sensitive to vacuum pressure by a factor of 4-6 [14].

As seen in Figure 3.3 the Nτ product could be increased by a factor of nearly two by using a heated gold strip to increase the rubidium pressure. The SAES rubidium dispensers were characterized using a SRS residual gas analyser. When the SAES dispensers are heated a significant amount of hydrogen is released along with rubidium. Using a gold/rubidium dispenser will reduce the background hydrogen by first coating the gold foil with rubidium and then allowing the pressure to recover. When the gold is heated only rubidium is released because hydrogen will not readily sorb to the gold surface. The improved vacuum performance seen in Figure 3.3 is attributed to reduced hydrogen background.

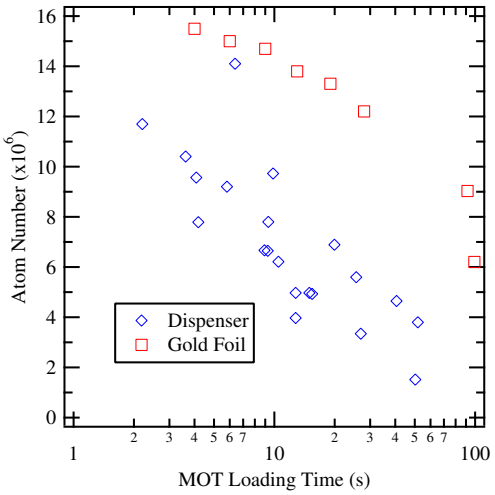

Figure 3.3: The squares show the rubidium dispensing with the gold foil and the diamonds show the rubidium dispensing with a SAES dispenser. The MOT number is measured using a mirror MOT for both the SAES and gold dispensing data. The improved $N\tau$ product of the gold/rubidium alloy indicates the improved vacuum quality using the alloy dispenser relative to the SAES dispenser.

3.8.2 Gold as a rubidium pump

While I did not perform the final experiments on the gold rubidium dispensers the results will briefly describe it here for completeness. There was evidence from Sarnoff that a fresh layer of gold would act like a rubidium pump. In an effort to make a gold/rubidium dispenser without bulk processing gold was sputtering onto a Nichrome surface in the presence of rubidium vapor. The rubidium pressure was roughly monitored by the absorption of a laser beam passed though the cell. As soon as the gold was sputtered the rubidium signal immediately dropped. The gold deposition was stopped but the rubidium dispenser was left on. After approximately one hour the rubidium pressure recovered to the original pressure. The assumed pumping mechanisms was rubidium immediately forming an alloy with the freshly depositied gold, effectively creating a rubidium pump.

At CU the experiment was replicated by using small gold evaporators made by melting gold onto twisted tungsten filaments. The gold evaporator plus a Nichrome

strip, and a rubidium dispenser were put inside glass cell. In all of the experiments the rubidium dispenser was activated before the gold was evaporated on the cell so only the surface of the gold was exposed to rubidium. As with previous experiments the rubidium vapor pressure was monitored by passing a laser though the cell while being swept over a rubidium transition. The rubidium dispenser was already activated so running a few amps though the dispenser would immediately increase the rubidium pressure in the cell. The SAES rubidium dispenser was run until the rubidium pressure in the cell reached steady state. With the dispenser held at the same current the gold was evaporated onto the walls of the vacuum chamber. The experiment was built so the evaporated gold would not coat the region where the laser passed though the cell. Immediately after the gold evaporation the rubidium signal dramatically dropped to background levels (see Figure 3.4). After the gold was evaporated the SAES rubidium dispenser current was increased and gradually the rubidium pressure rose as the rubidium coverage on the gold surface reached equilibrium. This data was fit to a model that assumed there were a finite number of occupation site on the gold and in the rest of the vacuum cell, and that the rubidium had different affinities/binding energies for each surface. Specifically it was assumed that rubidium had a much greater affinity for gold than for the other materials in the system. The results of the fit are shown in Figure 3.4 [76].

From the results of the gold/rubidium diffusion experiments and the gold pumping experiments it is reasonable to conclude that on the time scale of hours the dominant mechanism in the gold rubidium interaction is a surface effect, otherwise the gold would act as a weak pump before the evaporation. On a final note about diffusion, the color of the gold coated Nichrome foils has been observed to change from bright yellow to a silver color over several weeks to months. While there is no data other than visual observation is reasonable to assume that rubidium and gold would interdiffuse on a longer timescale and that a visual change in the color due to alloy formation would be seen by eye.

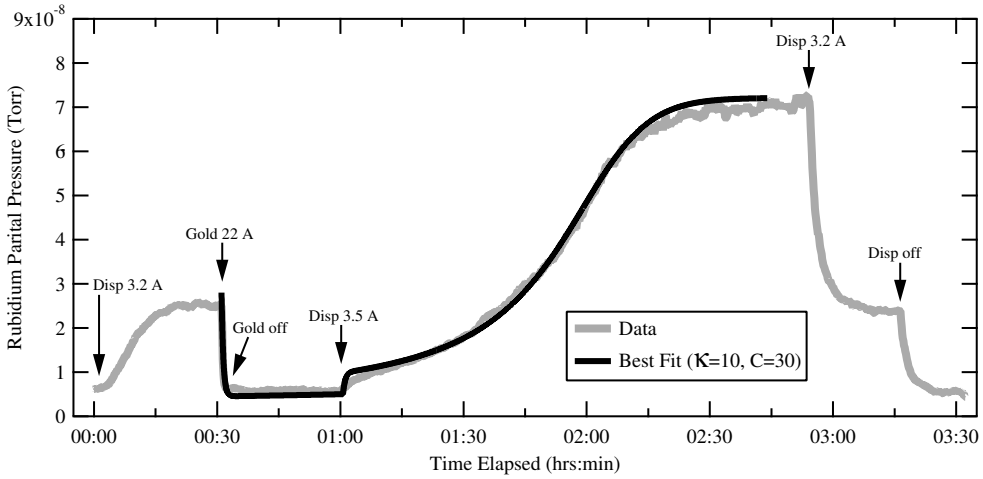

Figure 3.4: Best fit of gold pumping data showing rubidium gold interaction is well fit by a surface interaction model [76].

3.9 Gold versus other metals

What about the behavior of other materials for dispensing rubidium? In one experiment two identical pieces of Nichrome foil were placed in a glass cell. One of the pieces was coated with evaporated gold and the other piece was left uncoated. The rubidium dispenser was positioned so the dispensed rubidium hit each foil equally. The two foils were exposed to the rubidium at a pressure of $\sim 10^{-7}$ torr for approximately 5 minutes. After the rubidium dispensing one foil is heated with a constant current while the rubidium pressure is continuously monitored until the rubidium is emptied from the first foil. The process is then repeated for the second foil. This procedure is repeated several times, each time switching the order that the foils were activated to remove systematic effects related to one foil dispensing onto the other foil. On average the Nichrome foil dispensed about 1/5th the rubidium as the gold coated foils. This shows rubidium will sorb onto any cold surface which can be later dispensed by heating the substrate, but the increased rubidium dispensing from the gold shows the increased sticking coefficient due to the gold/rubidium alloy even at short time scales.

Chapter 4

Experimental setup and operation

4.1 Vacuum cell design and construction

The design of this compact vacuum system is similar in many ways to the construction of chip based and larger BEC systems; however there are a few key features that are noteworthy. First, the cell is assembled without the vacuum being exposed to epoxies that were used in the original chip based BEC systems [1, 14]. The anodic bonding process [77] makes this possible and allows the vacuum cells to be processed at much higher temperatures than was possible with earlier cell fabrication techniques [18]. Anodic bonding has been used in previous atomic physics experiments [78] but we are not aware of anodic bonding being used in BEC systems especially to construct a UHV system. The majority of the differential pumping between the two chambers is accomplished by a single 0.75 mm aperture and the higher pressure region utilizes non-evaporable getters to maintain the vacuum pressure. Also, the system features an atom chip with electrical feedthroughs or vias though the atom chip which simplifies electrical connections to the vacuum regions of the system. The vacuum chamber (see Figure 4.1) has four general parts: the atom chip, the BEC cell, the center six way flange, and the 2D MOT cell. Each of these parts, their construction, and assembly will be described. The basic process of anodic bonding will also be discussed in Section 4.2.

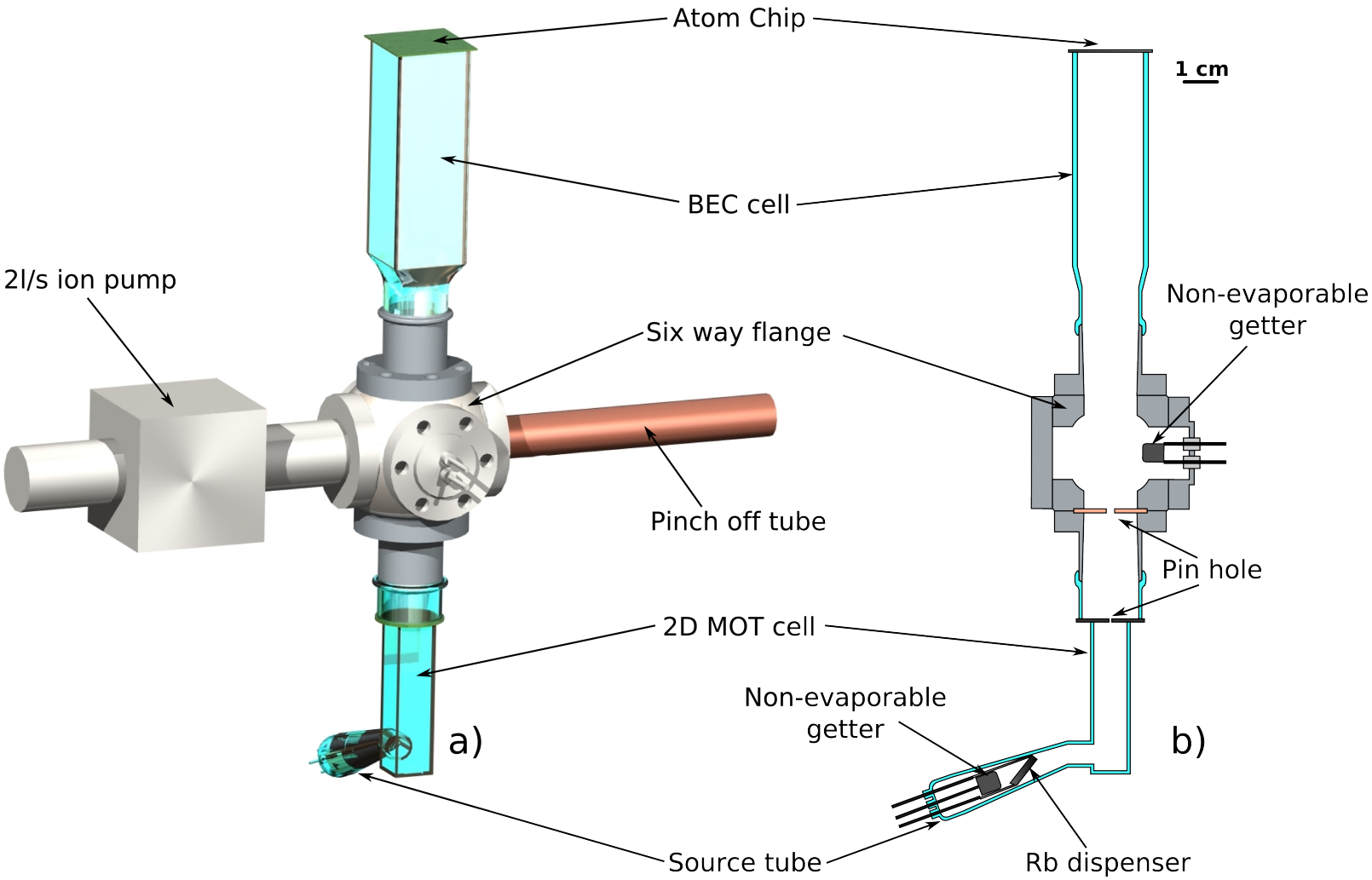

Figure 4.1: Views of a two chamber cell. Figure a.) shows an isometric view of the cell construction including the placement of the ion pump and pinch off tube. Figure b.) shows a cross section of the cell including the placement of the apertures, the NEG for the BEC region, and the configuration of the rubidium dispenser and the 2D NEG.

4.1.1 2D MOT cell

The 2D MOT cell is made from a 1 cm Pyrex flourimeter cell (Starna Cells 3-Px-10). The cell is lapped and polished on the open end, and a rubidium source tube is glass blown to one of the side walls of the cell. The source tube is a 12 mm Pyrex tube that is closed by a Pyrex disk with four pin press electrical feedthroughs [6]. Attached to the pin presses are a non-evaporable getter (SAES getters HI/7-6) and a SAES rubidium dispenser. The getter is used to pump the hydrogen released by the rubidium dispenser and to help maintain the vacuum in the 2D MOT cell. The 2D MOT cell is isolated from the ultra high vacuum regions of the system by a 1 mm thick silicon disk with a 0.75 mm diameter aperture in the center of the disk. This aperture reduces the conductance between the 2D MOT region and the BEC chamber to $< 0.1\,\ell/\mathrm{s}$, allowing us to maintain a pressure difference of two orders of magnitude between the two chambers of the vacuum system. One face of the silicon disk is anodically bonded to the polished end of the 2D MOT cell and the other side of the silicon disk is bonded to a lapped and polished glass to metal transition on a mini-conflat (1.33") flange. The second bond is done in such a way that it does not apply a significant electric field across the first bond to avoid de-bonding. The details of the anodic bonding process are discussed in Section 4.2.

4.1.2 Spherical cube / pinch off

The 2D MOT assembly is bolted to the center vacuum flange with a solid copper conflat gasket with a 3 mm diameter hole in the center of the gasket. In principle the flourimeter cell could be directly attached to the glass to metal with the copper gasket providing all of the differential pumping. However, the silicon disk also acts as a mirror surface so the cell may be used in a 2D+ MOT configuration [79].

The 2D MOT cell is joined to the BEC cell and vacuum pumps by the center vacuum flange. The flange itself is a six-way mini-conflat cube (Kimball Physics

MCF133-SC6). A 2 ℓ/s ion pump mounted perpendicular to the MOT cells maintains the pressure in the BEC cell. Additionally a second non-evaporable getter (SAES getters HI 7/6) is connected to a conflat mounted power feedthrough and is used in lieu of a titanium sublimation pump. A copper pinch off tube is brazed to a welding lip on a mini conflat flange. The brazing material is a UHV compatible silver solder and all brazing flux is removed to ensure low operating pressures. The conflat copper tube assembly is bolted to one of the remaining ports on the spherical cube. The location of the 2 ℓ/s ion pump and copper pinch off are determined by the position of pre-existing mirrors and beam paths.

4.1.3 Pumps

Because the vacuum system is pinched off from the pumping station any pump used in the vacuum system must permanently capture the gas that it pumps. There are three basic pumps in the compact vacuum system. Ions pumps for all species of gas, getter pumps for chemically active gases like oxygen, and the walls of the system for rubidium.

Ion pumps work by ionizing gas inside the pump and then accelerating the ion into the walls of the pump by a voltage of a few kV. In a diode pump once the ions strike titanium plates in the walls they are pumped by two processes: chemical adsorption and burial. Atoms are chemically pumped when a chemically active gas (i.e. nitrogen, oxygen, hydrogen) is exposed to fresh titanium which is extremely reactive. Once these nitride, carbides, etc. are formed they are assumed to be stable and will be permanently removed from the system [80]. The surfaces of the titanium plates in the ion pump constantly refreshed and scrubbed ion bombardment but over time the sputtered and reacted metal will cover all pump surfaces reducing the pumping speed. This process will continue to pump until all the titanium has been chemically reacted with active gases. Normal pump lifetime is on the order of 40,000 hours at 10^{-6} torr.

Fortunately ion pump lifetime is inversely proportional to pressure so at 10^{-9} torr ion pump lifetimes are approximately 1,000 times longer (thousands of years). If there is a catastrophic failure and the ion pump is exposed to air the ion bombardment will be stopped by the reduced mean free path at a pressure of less than 1 torr. The shutdown will happen very quickly so a rapid venting should not significantly shorten the lifetime of an ion pump. That being said a new ion pump will have the best performance because all of the metal surfaces are clean and available to sorb gases.

Chemically inert or noble gases (He, Ne, Ar, etc.) are pumped by being buried in the titanium plates. As more metal is sputtered (ejected by ion bombardment) it will increasingly bury the gas below metal. The burial process only happens in new pumps, if the system is exposed to a high noble gas load eventually the noble atoms in the plates will come into equilibrium with the gas pressure. For every noble gas atom that is accelerated into the plates it will eject a previously buried atom. This equilibrium is called saturation and to a lesser extent occur for active gases. For active gases the titanium will continue to chemically sorb active gases, however when the plates fill with a noble gas the pumping speed is significantly reduced. This noble saturation effect can be mitigated by using two different metals (titanium and tantalum) so there is a differential sputtering rate that will preferentially bury the noble atoms on one side of the pump. The other method commonly used for pumping noble gases is a triode pump. In a triode pump the sputtered material does not fall back onto the plates but is deposited behind the titanium plates on the walls of the pump. Because this material is outside the sputtering zone the buried gases cannot be reemitted.

For portable vacuum systems made from glass helium diffusion is a problem worth considering, because helium is present in the atmosphere in concentrations of $\sim 4 \times 10^{-3}$ torr. Helium is small and non-reactive so it can diffuse into a glass envelope to a steady state pressure of a few militorr if the helium is not pumped away [57]. An earlier experiment with increased local helium pressure around a quartz cell showed the

pressure in the cell rapidly increased and when the helium was taken away the pressure in the cell dropped [14]. The cell was made from quartz which has a higher diffusion rate than Pyrex. It is possible that after several years the ion pump will be saturated with helium but that can be improved by using a noble diode or triode pump. Completely removing the ion pump is not a good option because uncompensated helium diffusion will degrade vacuum quality.

In the current configuration a 2 ℓ/s ion pump is attached to the side of the spherical cube and significantly increases the overall size of the vacuum system. The position of the ion pump relative to the chip is important because the vacuum system was retrofitted into the pre-existing opto-mechanics for a single cell vacuum system. The total size of the vacuum cell can be reduced farther if the spherical cube and the ion pump are integrated. This could be accomplished assuming a SHV connector is used instead of the new Varian style ion pump connector and the ion pump was integrated into the spherical cube with a hole though the center of the ion pump interior to allow atoms from the 2D MOT to propagate to the upper chamber. This ignores the effect of the electrical field on the atoms [81]. Another consideration in compacting the ion pumps is shielding the ion pump's magnetic field from the BEC experiment. Excellent magnetic field shielding has been accomplished at CU by using a clamshell type μ-metal shield around the ion pump.

The other pump that is used in the BEC system is a non-evaporable getter (NEG). Getter pumps work by chemically absorbing active gases into a metal with a high surface area. The method of capturing and removing atoms from the vacuum is the same chemical pumping mechanism in ion pumps. The difference between an ion pump and a NEG is the NEG has a high surface area achieved by sintering a finely powdered metal alloy around a heating element. In air a thin oxide layer is formed over the entire surface of the NEG. Once the NEG is installed in the vacuum it is activated by heating it to $600 - 800°$C. This diffuses the surface oxide into the bulk of the material and exposes

fresh metal to the vacuum. Any gases that are adsorbed on the fresh NEG surfaces are permanently removed from the vacuum.

The other gas that is pumped by a NEG (and ion pumps) is hydrogen, however its sorption is reversible because it is favorable for the hydrogen to diffuse into the NEG, but not permanent. Before, during, and after activation the NEG is heated to a few hundred degrees celsius to drive off hydrogen. Hydrogen pumping is a key requirement for vacuum system with rubidium dispensers because tests of dispensers show rubidium dispensers release a significant amount of hydrogen when heated. The rubidium dispensers release hydrogen because they are also made with a getter like material that traps hydrogen. Non-evaporable getters have been used in every compact vacuum cell built at CU, so it is difficult to tell if NEGs play a significant role in the vacuum quality but in principle removing them from the vacuum system should only degrade the vacuum quality.

The final pumping mechanism in a compact BEC system is rubidium adsorbing onto the walls of the vacuum chamber. Rubidium has a bulk vapor pressure of $\sim 10^{-7}$ torr at room temperature, but when rubidium interacts with a clean vacuum wall the rubidium is effectively pumped away. It is plausible that the rubidium interacts with the oxides in the wall and forms RbO_x. It is generally accepted that no rubidium will be seen the first time a new vacuum chamber is exposed to rubidium because a thin layer (presumably a few monolayers) of rubidium must coat the chamber to suppress the pumping action of the walls. In a two chamber system the walls of the upper chamber will act as a rubidium pump for a finite time but will eventually saturate. This saturation effect was not seen in two different cells with both cells being operated for several months. The presence of free rubidium in the upper cell is determined by turning the 3D MOT on with the 2D MOT off and loading for several minutes; At the end of several minutes of loading no is MOT seen. An alternative rubidium pump with increased capacity is graphite. Atomic fountain clocks use a graphite tube to pump

residual cesium atoms with a large pumping capacity [82].

4.1.4 3D MOT cell

The BEC cell is made by glass blowing a custom made (New Era Enterprises) square 2 cm ID Pyrex cell to a Pyrex glass to metal mini-conflat adapter and then anodically bonding an atom chip to the top of the glass cell. However the cells are not immediately ready to be used when they arrive and require several processing steps. The original joining method leaves residual stress in the edges of the cells that caused cracking after anodic bonding. Sarnoff found the stress could be removed by fusing the edges of the cell with a torch. The entire cell is annealed after the edge fusing to remove the stress of the glass blowing [83]. After the cells are lapped they are glass blown to a Pyrex glass-to-metal transition. The cell should be consistently aligned with the bolt hole pattern to avoid changes later during assembly. The cell and glass to metal are annealed again to remove residual stress that would affect the lapping, polishing, or anodic bonding.

The lapping and polishing was done by hand at Sarnoff and made a flat and smooth surface for anodic bonding but the polished surface was not always at right angles relative to the cell. Recently CU built an apparatus for lapping and polishing cell in a pre-aligned jig to lap cells at right angles to the conflat flange. After lapping and polishing the cell is throughly cleaned for UHV and anodic bonding. Then a silicon atom chip [1] with UHV electrical vias is anodically bonded to the lapped and polished surface.

A few notes that may be useful for future cell design. The walls of the cell are not anti-reflection (AR) coated because of the large number of processing steps that includes glass blowing. The few percent reflection from the walls has an impact on the imaging quality and reproducibly splitting a BEC [84]. In principle the exterior of the cell can be AR coated after the cell is anodically bonded. Coating the interior walls of

the cell is more difficult but could be accomplished by one of the many chemical vapor deposition processes.

The length of the cell is chosen to be able fit a MOT with right angle beams directly below the chip. Because of the success in a MOT with angled beams (see Section 2.4.4) the length of the cell could be shortened. Current cells have not been shortened because of the opto-mechanical setup based on the original size of the vacuum cell.

4.1.5 Atom chip

The atom chip is a 400 μm thick silicon wafer with a silicon oxide layer for electrical isolation. The wires are formed by electroplating copper into a photoresist mold the shape of the final wire pattern. The resulting wires are typically 10 μm tall and 100 μm wide. The chip is patterned with a 15 mm wide Z-wire with crossing wires every 1 mm (see Figure 4.2). The areas between the copper wires are also electroplated with copper to form an "optical metal" that could be used as a mirror surface for a mirror MOT or reflection imaging [18].

The largest chip Z-wire is connected to two vias and can support up to 5 A. The remaining wires are each connected to a single via and can support 2.5 A. A variety of Ioffe-Prichard (IP), quadrupole, dimple, and waveguide geometries can be configured depending on where the currents are sourced and sunk. As mentioned previously, the electrical connections to the vacuum side chip wires are made though the silicon chip by UHV compatible vias [85]. Each via can support 2.5 A, and the vias can be joined together to support higher currents. The vias are made to withstand the high temperatures (> 400°C) required for anodic bonding and vacuum processing. The connecting pads on the ambient side of the chip are coated in gold to prevent oxidization during high temperature processing. To protect the copper on the vacuum side of the chip during anodic bonding the bond is performed in a reducing gas atmosphere (4-6% H_2,

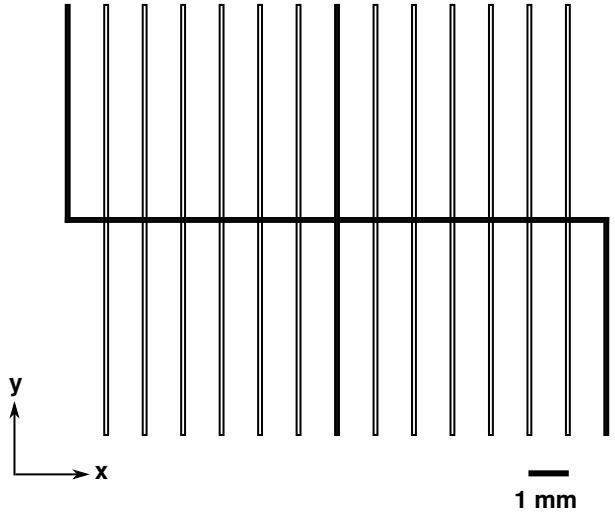

Figure 4.2: Schematic wire pattern of the chip used to produce BEC. Depending on where the currents are sourced the chip can be configured as a large Z-wire trap with many crossing wires, a variety of H-traps, a long waveguide, etc. The wires with the filled pattern show wires used in experiment. The experiment was also performed using wires other than the center vertical wire and minor adjustment of the other experimental parameters with the same results. The leads that form the outermost legs of the Z-wire are connected to two vias so the maximum possible current in the Z-wire is 5 A. All other leads are connected to a single via that can support 2.5 A. On the actual chip the regions between the wires are filled with "optical metal" that can be used as a mirror surface if necessary. The optical metal is not shown in this figure for clarity.

94-96% N_2). To prevent explosions the hydrogen should be kept below 10%.

The thickness of the silicon (400-500 μm) will easily hold against ambient air pressure over 2 cm^2 because chips as thin as 100 μm will hold atmospheric pressure over a 2 cm^2 area. Despite the physical strength of the silicon the atom chips flex when heated due to current in the chip wires. This mechanical flexing interferes with imaging and the general stability of the atom trapping. The stability of the chip is enhanced by attaching a 1 mm thick disk of silicon to the back of the atom chip with a high temperature compatible epoxy (EpoTek 383ND). The extra support increases the thermal mass of the silicon chip and reduces the chip deflection (see Figure 4.4). The ambient side of the chip is patterned with pads positioned directly above the cell wall so electrical contact may be made to the pads without risk of fracturing the chip (see

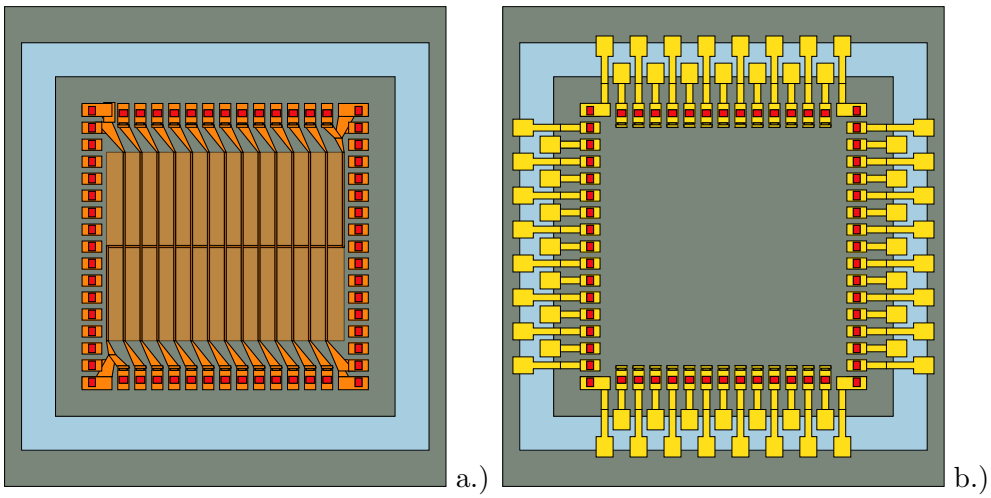

Figure 4.3: The vacuum (a.) and air (b.) sides of the atom chip. The grey area is the size and shape of the atom chip. The light blue area just inside the rectangles is the position where the Pyrex cell is anodically bonded to the chip. The red boxes around the inside perimeter of the chip are the locations of the UHV compatible vias. In Figure a.) the all of the shaded areas are electroplated copper. This image shows the location of the optical metal between the traces. In Figure b.) the shaded traces show gold pads that connect the vias to pads positioned over the cell location for additional strength when connecting to the cell.

Figure 4.3). The pins (MILL-MAX M09922) provide good electrical contact without applying excessive force to the chip.

4.1.6 Bakeout and pinch off

After the vacuum system has been assembled it is attached to a pumping station via a copper pinch-off for vacuum bakeout. Bakeout is a critical part of making it possible for a vacuum system to achieve UHV ($< 10^{-9}$ torr). The main goal of a bakeout is to heat the vacuum system above 100°C so water adsorbed on and into the interior surfaces of the vacuum chamber will be "boiled" off and pumped out of the system. Not only water will be boiled off but any contaminant with a high vapor pressure. Higher temperatures are better for preparing a vacuum system for UHV because the contaminants in the system are not only adsorbed onto the surfaces in the vacuum chamber but can also be deeply diffused into the bulk of the materials in the

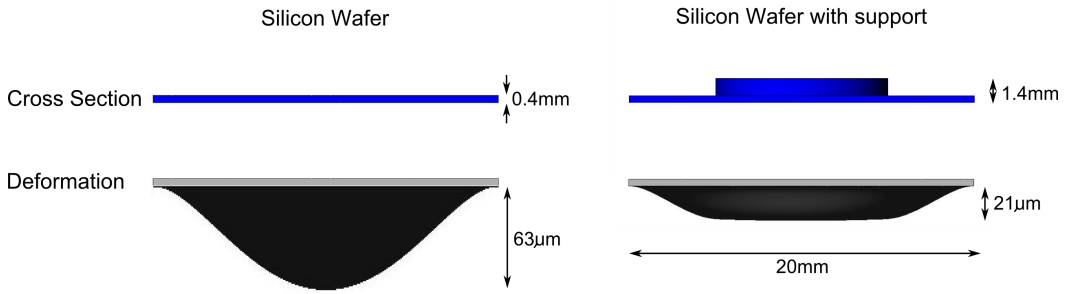

Figure 4.4: Deflection of a 2 cm square silicon chip with and without a 1 mm thick, $\phi = 1$ cm silicon disk that is attached to the back of the chip. The disk improves mechanical stability and reduced the deflection of the silicon chip. Calculations performed with the COSMOSXpress tool in SolidWorks.

chamber. Glass is known for holding a significant amount of diffused water. During baking the cell is maintained at the highest possible temperature because the diffusion rate increases with temperature. In the early cells the highest bakeout temperature was limited to less than 200°C by the epoxy (353ND) that was used to attach the atom chip to a quartz cell [14]. In current cells the atom chip is anodically bonded to a Pyrex cell at > 400°C and the cells are baked out at a lower temperature of ~ 300°C to avoid heating the cells above the bonding temperature and to reduce thermal mismatch stress.

Qualitatively the vacuum pressure is significantly improved in the vacuum cells that are baked at higher temperatures. The rough metric for vacuum quality is the MOT loading time and lifetime. In a single chamber configuration epoxied cells typically had MOT loading times of 30 s and $1 - 2 \times 10^6$ atoms loaded from the background rubidium after the SAES dispenser was turned off [14]. These numbers were typical for immediately after bakeout however the MOT loading time typically degraded as the cells aged. Anodically bonded cells have MOT loading times 2-3 times longer than epoxied cells and 2-4 times the atom number. The longer lifetimes and increased MOT number are both a result of the higher bakeout temperatures made possible by anodic bonding.

The baking process for the vacuum cells assures thermal gradients over the vac-

uum cell are minimized. The copper pinch-off tube on the cell is attached to a compression port (Varian FCP0075UHV) on the bakeout system. The cell is then encased in an aluminum sheet metal box with an interior support structure to hold the cell within the enclosure. All electrical connections to dispenser, getter, thermocouples, etc. are made by barrel connectors, stainless steel crimps, or wire wraps. Wire wrapping the connections is the least invasive and most reliable of all the connection methods. Solder can be used at low temperatures but at $< 300°$C the solder melts and cannot be used inside the bakeout box. After the electrical connections are strain relieved the aluminum box is wrapped in heater tape and insulation. The heat from the heater tape is spread by the aluminum and uniformly heats the whole cell. The only significant thermal gradient is the area of the copper pinch-off, but there are few problem with leaks in this area.

The temperature of the cell is gradually increased, typically at $1-2°$C/min, up to the bakeout temperature. Cells have been baked for as short as two days with excellent results. For example the high duty cycle, number optimized, and speed optimized results of Chapter 5 were produced with a cell that was baked two to three days. Cells have also been baked for longer periods typically two weeks with the lifetime improving by about 50%. The cell that was used for the atom splitting experiments in Section 6.1 was baked for several weeks. During the bakeout the various dispensers, getters, gold coated pieces, etc. are degassed and activated according to the manufactures specifications. The cell is then cooled at the same $1-2°$C/min to room temperature. After the cell is cooled the ion gauge on the bakeout station will typically have a pressure $< 4 \times 10^{-11}$ torr (actually is goes off scale low at this point).

If the system does not go off scale there is typically a small leak. If the leak is in the vias it can be sealed by VacSeal (distributed by SPI) diluted with acetone and then the system should be baked again for a few days. After the vacuum pressure is acceptable the rubidium dispenser is turned on for 10 mins until rubidium florescence is visible with a sweeping laser. This ensures the cell walls are coated with rubidium while

the cell is still attached to the pumping system. The system is then pinched off (CHA Industries pinch off tool) leaving approximately 0.75–1 inches of clearance between the braze joint and the pinch off to avoid cracking the braze.

4.2 Anodic bonding for UHV construction

Anodic bonding in used in the BEC cell construction because of its excellent vacuum properties and high temperature limits. Anodic bonding has been used before in atomic physics experiments [78] but we are not aware of anodic bonding being used in BEC systems.

Anodic bonding is a low temperature process for bonding two dissimilar materials using an electric field to assist in the bonding. It is considered a low temperature process because the bond is performed below the annealing temperature of the glass. Anodic bonding is typically performed at a temperature close to 400°C and requires materials with matched coefficients of thermal expansion. Silicon and Pyrex are used in the BEC apparatus because both materials are readily attained and UHV compatible. Ultra-high vacuum compatible Pyrex to metal transitions are available from a variety of vacuum component distributors. Anodically bonded parts will not leak ($< 10^{-10}$ torr ℓ/s) after repeated baking and cooling cycles. While some extra care is required to prepare the surfaces for anodic bonding, once the parts are joined the bond is stronger than the constituent materials. Anodic bonding can be used to build custom glass UHV vacuum chambers without significant labor and the parts can be easily manufactured by standard glass and silicon processing. A wide variety of UHV chambers and structures have been constructed by anodically bonding silicon wafers to Pyrex wafers, tubes, and cells.

The process of anodic bonding starts with clean, flat, and polished surfaces. The components are cleaned using standard optical cleaning techniques and are placed together with a slight amount of pressure (typically a mass of a few kg is used to apply pressure). The parts should be flat enough to see a few interference fringes across the

sample. Flatter is better but the electric field will pull the parts together during bonding. The parts are then heated to 400°C. Heating the Pyrex is critical because it increases the mobility of the sodium ions in the Pyrex. After heating, a voltage of approximately 1 kV (it depends on the thickness of the materials) is applied across the silicon and glass (see Figure 4.5). There are two signs of a successful bond. Because bonding involves a migration of ions in the glass [86] there is a small current that is generated during bonding. The current will start around a few hundred μA at the beginning of the bond process and will fall to the background level as the bond is completed. The other sign of successful anodic bonding can be seen by looking at the silicon/Pyrex interface. Areas that have bonded will appear dark as the bonding draws the two parts together without an air gap. It is possible to visually monitor the progress of the anodic bonding by watching the progression of the dark areas. Once all of the areas to be bonded are dark and the current is steady then the parts can be cooled. The heaters can simply be turned off and the parts allowed to cool at $10 - 20$°C/s without the bond failing or the parts cracking.

A successful anodic bond relies on a large electric field at the bond interface to promote ion transport. If the electrode is placed too far from the glass the electric field will be weak, and the bond will be weak or fail. If the electrode is too close to the silicon it will arc, which can be dangerous (especially in a hydrogen atmosphere) and damage the part. When bonding cells a wire or BeCu foil is wrapped around the glass cell 2-3 mm from the bond interface. In general, anodic bonding is an irreversible process. However, for double sided bonds it is important not to apply the field the wrong way across a bond that has already been formed, as this can cause de-bonding.

4.3 Control and imaging systems

The control and imaging system are important from the practical point of view as they are the interface to the operation of the experiment. A new linked control program

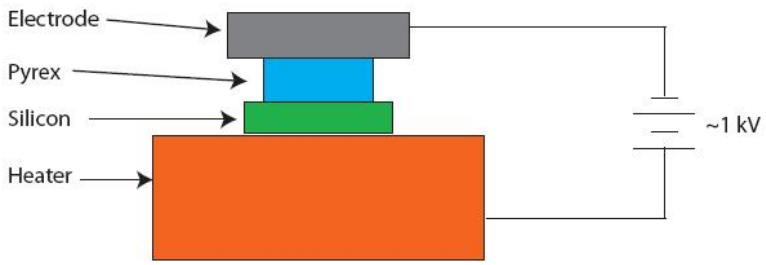

Figure 4.5: Schematic diagram of anodic bonding especially the polarity of the bond relative to the silicon and Pyrex.

and imaging software were developed for operating the BEC experiment because rapid MOT loading and BEC production lends itself to rapid and semi-autonomous optimization [87]. The semi-autonomous operation includes a "good" shot algorithm to trigger the next data run if the experiment was operating properly and to beep if the last data run was poor (see Figure 4.6).

4.3.1 Control system

The production of BEC has many steps that involve controlling the multiple aspects of the laser, magnetic, and imaging systems at various times. Along with the complexity there are often various modes of operation including testing and diagnostics that require various aspects of the experiment to be turned on or off while maintaining the behavior of the rest of the experiment.

The original control software was channel based and sometimes required multiple changes across various channels depending on task [14]. The new control software is task based and once a task is configured in the software it is possible enable or disable an entire task with a single click. This is achieved by using the tree structure (new in LabVIEW 7) with the main nodes used to define the main tasks (e.g. CMOT or imaging) and the sub-nodes to define the individual parts of the main tasks (e.g. laser detuning, bias field, etc.). As seen in Figure 4.7 the program is written so that all nodes

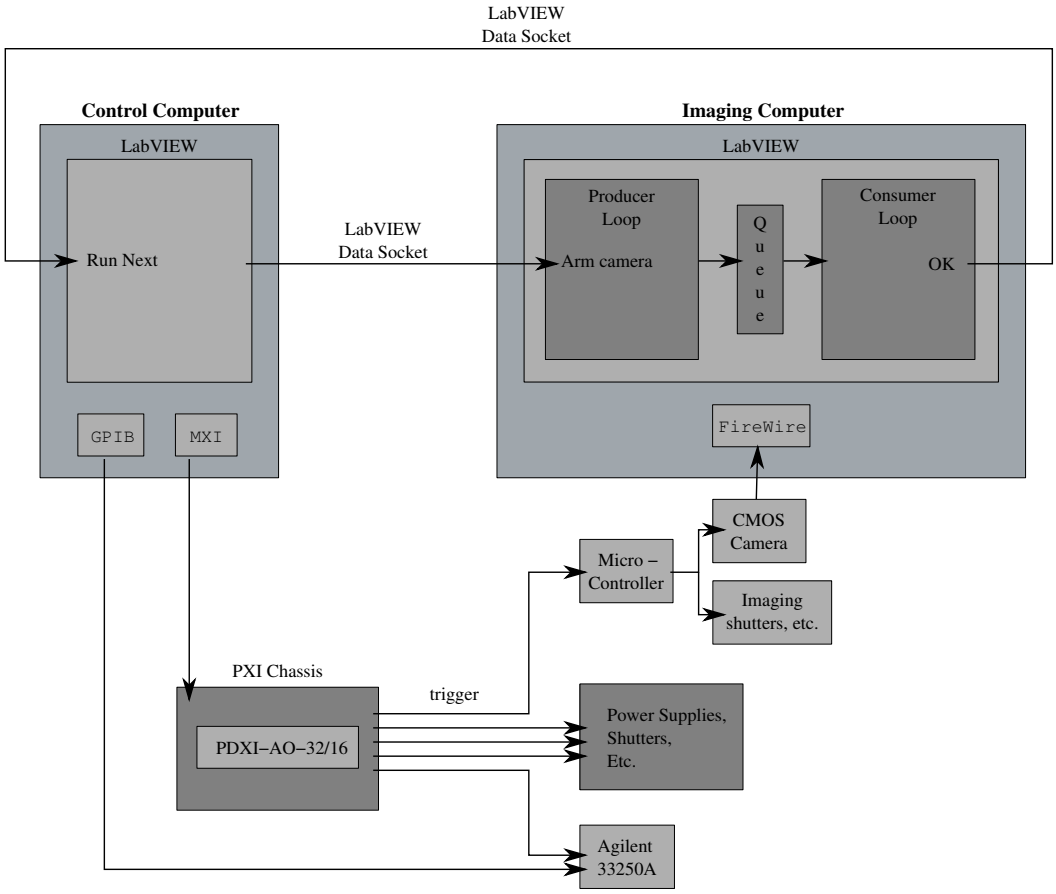

Figure 4.6: Diagram of control and imaging systems with connections to external hardware. When the control computer starts processing a data file it sends a command over the LabVIEW Data Socket to the imaging computer to wait for a sequence of 3-4 images. After the images are taken the control computer calculates the OD and determines if the shot was well behaved (as determined by the atom number). If the shot was well behaved the imaging computer triggers the control computer to run the next experiment.

can be activated or disabled so a main node like optical molasses can be disabled so the CMOT performance can be evaluated. Disabling the optical molasses node (PGC) is accomplished by disabling the main optical molasses node and every sub-node is automatically disabled (see Figure 4.7). Additionally each sub-node can be individually enabled or disabled. For example, the dimple channel can be turned off to effectively create a hold phase to evaluate the chip Z-wire compression.

Stage	Start	Duration	Channel	Value
TestMOTs	0	0		
Repump Shutter	0	TtotalMOT+	11	5
Cooling Shutter	0	TtotalMOT-	9	5
ExternalZ	0	TtotalMOT	30	-1
Collection	0	0		
2D MOT Cooling Sh	0	Tcollect-50	21	5
2D MOT Repump Sh	0	Tcollect-50	18	5
MOTCoils	0	Tcollect	0	motMOT
Xbias	0	Tcollect	19	XbiasMOT
Ybias	0	Tcollect	2	YbiasMOT
Zbias	0	Tcollect	3	ZbiasMOT
RepumpPower	0	Tcollect	10	0
CoolingFreq	0	Tcollect	8	11.5
Compression				
Hold	0	0		
PGC	0	0		
OP	0	0		
MT	0	0		
XferAtomsUp	0	0		
Xfer2Chip	0	0		
Dimple_1	0	0		
Hold1	0	0		
DISABLED - RFSweep1	0	0		
DISABLED - RFSweep2	0	0		
DISABLED - MTHold4	0	0		
Decompress	0	0		
Image				

Figure 4.7: Example of a LabVIEW tree used to control experimental BEC production. This example shows control over major section (e.g. the entire RFsweep1 is disabled), the use of variables (e.g. Tcollect is used several times but can be changed in the global variable section), and sub-elements (e.g. Xbias branch) that can be disabled without affecting other sub-elements.

As seen in Figure 4.7 variables can be used in the program to link different stages of the experiment. Along with the tree structure there are global and local variable sections in the control program. A typical local variable would be the MOT field gradient (motMOT) because it is used only in the MOT loading section and is not needed for the

rest of the program. The global variables are typically time variables because subsequent sections need the timing information of previous sections. In principle the timing can be configured so when one section ends the next section begins and there is no need to communicate timing information between the different sections. It is practically easier to pass timing information with global variables. The global variables are also useful for linking variables in optimization (e.g. fix the ratio of the chip wire current and transverse bias field to maintain the trap height but vary the trap gradient).

The control program is able to semi-autonomously vary variables over a user defined range. The user defines the variable and the range of values for the experiment. The order of the values is randomized so systematic effects like heating and rubidium pressure will be suppressed in the data. After one value is run the Imaging computer will determine if the number of atoms falls within an acceptable range. If the experiment is well behaved then the Imaging computer will set a network variable high (via the DataSocket connection) that triggers the next value to be run on the Control computer. If there was a problem with the data the user has the option of repeating the experiment with the original value or ignoring the error and continuing with the next value. This semi-autonomous system is very productive with a rapid BEC production system. This semi-autonomous system could be expanded if two technological issues were solved: the stability of the laser locking and safety systems for the chip and external Z-wires. Improvement in these areas could lead to a multidimensional optimization routine that could be left to take data or find an optimal experimental condition.

The individual experiments are saved in XML like files that have an organizational structure similar to the tree structure. The files save all of the variables and timings exactly as they were represented in the tree. These timing files can be edited by hand if needed and in some cases (i.e. duplicating whole stages) it is easier to edit the timing files by hand than to use the LabVIEW tree interface.

Where it is possible a calibration is used to go between the physical units (Gauss,

MHz, etc.) and the control voltages. This allows the equipment in the experiment to be switched without changing the control values. For example a new coil power supply only needs a new calibration to create the same magnetic field as the previous power supply. The calibration is saved in calibration file that is based on the zero and five points of the signal and assumes the relationship between the control voltage and the output is linear. The basic calibration involves adjusting the control voltage until the signal is zero (e.g. laser frequency is on resonance with a peak). The control voltage is then adjusted until the signal is at 5 (e.g. 5 MHz detuned from the resonance peak) then these values are put into the zero and five columns respectively. The calibration file also includes limits for each channel as a layer of safety to prevent accidentally overdriving the system.

4.3.2 Imaging system

The imaging system consists of a microcontroller shutter/trigger sequencer, a CMOS camera, and a dedicated imaging computer and software. The microcontroller shutter/pulse controller is used to produce the same pulse train for the imaging shutter, AOM driver, and camera trigger. A dedicated microcontroller is used because the DAC card (UEI PDXI-AO-32/16) changes the timing resolution depending on how many channels are being used. A PIC microcontroller was used because it easily has the timing resolution (1 μs) and was easily programmed by the JILA electronics shop. The imaging pulse train is triggered 10 ms before the atoms image to allow enough time for the shutters to open before the image is taken. The shutter/pulse controller can also be run without opening the imaging shutter allowing cleaning and dark images to be taken with the same timing.

A separate computer from the Control computer is used for taking pictures of the BEC and processing the images. A second computer is traditionally used in BEC experiments for imaging because the Control computer uses a large amount of computer

resources to run the experiment and when the camera is triggered it is important that the data can be downloaded as fast as possible and without glitches. The fitting routines are typically computationally intensive so a second Imaging computer is a good practice.

The Imaging computer runs a LabVIEW program that controls the camera data capture, the data processing, and communication with the Control computer. The imaging software is based on a Producer/Consumer model where two loops run in parallel. The producer loop controls the camera, downloads the data, and then calculates and saves the OD to disk. The consumer loop waits until a new OD file is available, fits the OD to a 2D Gaussian fit, and then from the fit determines the atom number, cloud size, peak OD, etc. The two loops run independently so in principle the producer loop can record images as fast as possible while the consumer/fitting loop processes the data at a slower rate.

While it is possible for the producer loop to process data at a rate greater than the consumer loop the two loops nominally work sequentially because part of the consumer loop includes a rudimentary error detection calculation. After the cloud parameters are fit the atom number is used to make sure the system is working correctly. First the atom number must be above a minimum threshold value and once that condition is satisfied the current atom number is compared to the distribution of previous shots. If the atom number is within reasonable bounds then a network variable is set high and the Control computer starts the next experimental run. If the current atom number lies more than 1.5σ outside of the distribution then a beep is sounded and the data taking stops until there is human intervention.

The OD calculation follows most standard OD calculation methods [88, 6] but with an extra data processing step for getting clean images close to the chip. Because OD is a relative estimate there is a very high probability of shot noise introducing large errors in the dark regions (i.e. chip shadows) of the images. Rogue pixels will interfere with the integrated number and if a rogue pixel has a high enough value it will interfere

with the fitting results because each pixel is weighted equally. This spurious noise is removed by thresholding any pixel with a count less than 10% of the maximum pixel count (determined by the Light image) to one. Any position where the pixels are equal will result in an OD of zero so regions of low intensity will not contribute to the fitting or the integrated number. The OD fitting will be more reliable if a reasonable starting condition is given to the fitting algorithm. The JILA method of calculating the center of mass of the cloud is used to get a reasonable center for the cloud and then calculating the first moment of the cloud to get a reasonable estimate of the size of the cloud. This method provides very good starting values for the fitting routine and requires no user input.

4.4 Apparatus setup and operation

4.4.1 2D MOT

The 2D MOT beams consists of two pairs of counter propagating beams with an aspect ratio of 5:1. The laser is split into two beams that are retroreflected to effectively double the available cooling power. Retroreflecting the beams in a 2D MOT effectively doubles the cooling power and works as well or better than a non-retroreflecting configuration because the 2D MOT is optically thin. A small fraction of the 2D MOT laser power ($\sim$3 mW) is split off and is propagated along the axis of the 2D MOT. This extra push beam plus the mirror created by the silicon disk used at the top of the 2D MOT chamber creates the 2D+ MOT configuration and provides molasses cooling along the axis of the trap. This reduces the velocity of the atoms out of the jet and increases the capturable flux out of the 2D MOT [79]. The optimal laser intensity of a 2D MOT tends to be higher than the optimal intensity for a 3D MOT [89]. A commercial ($>$ 300 mW) and home built lasers have been used with equal success. Currently a tapered amplifier [90] is used to deliver 60 mW to the 2D MOT.

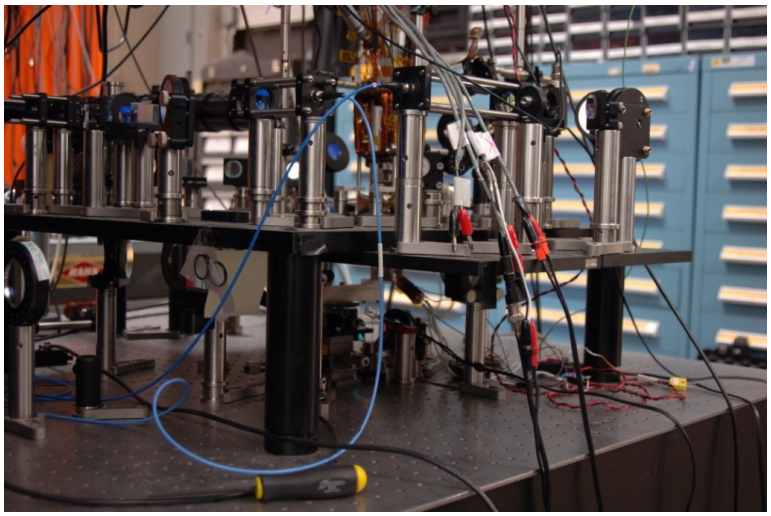
a.)

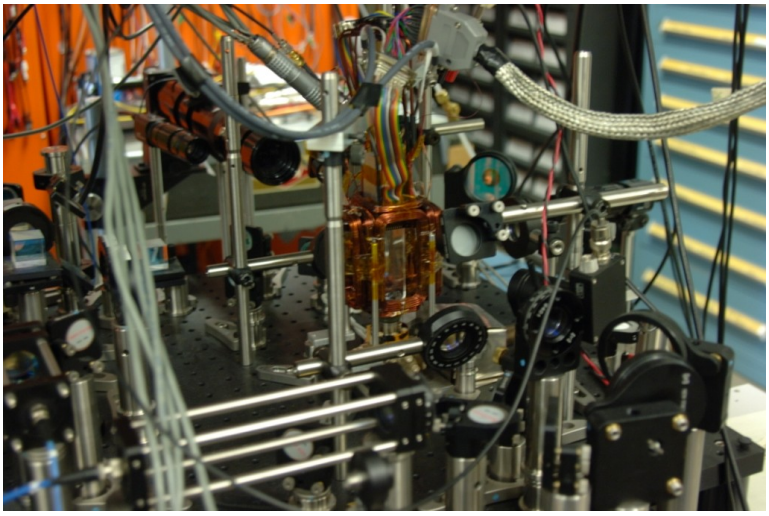
b.)

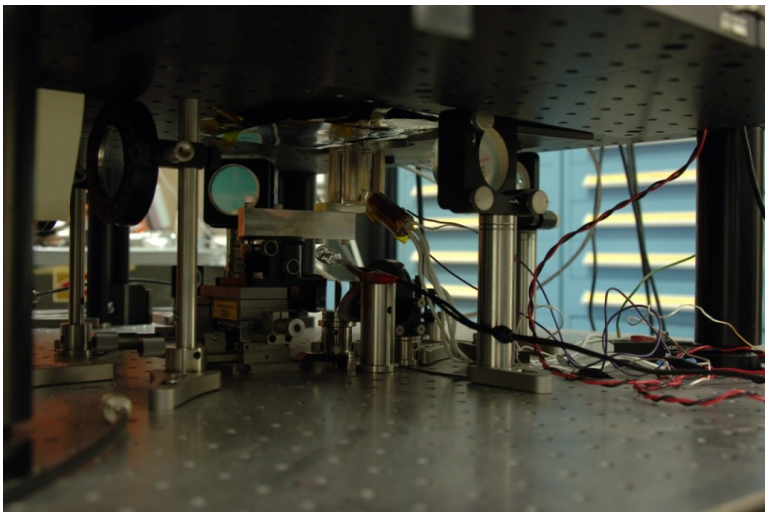
c.)

Figure 4.8: Pictures of the experimental layout: a.) shows the relative position of the upper 3D MOT chamber and the the lower 2D MOT chamber, b.) is a closer picture of the 3D MOT and imaging opto-mechanics, c.) shows the optomechanics and heaters for the 2D MOT.

The first step of aligning a 2D MOT is to center two pairs of retroreflecting beams on the 2D MOT cell. The beams are retroreflected by placing an iris in the center of the main beam before it is split. The retroreflecting mirror is adjusted to send the reflected beam back though the iris. The iris reduces the size of the beam so it is easier to see small misalignments. With an iris in the beam the power balancing of the two split beams is balanced by adjusting the half waveplate before the splitting polarizing beam splitter (PBS). The beams should have the same height as they pass though the cell so the force on the atoms is uniform as the atoms propagate along the axis of the 2D MOT. The beams should not clip any part of the cell where the atoms exit the 2D MOT chamber because the scattered light can cause the atom beam to deflect just as it exits the 2D MOT cell.

If the 2D MOT cell is not AR coated there will be a slight beam imbalance because the retroreflected beam has passed though four glass interfaces. Assuming there is a 4% loss at each interface the returning power will be about 85% of the original beam. The positive side of retroreflecting the beams is the total cooling power is nearly doubled. Early 2D MOT experiments found the retroreflected 2D MOT configuration yielded higher fluxes compared to a four beam power balanced configuration using the same initial power [91]. This indicates 2D MOTs are optimized when the total cooling power is maximized (the flux saturates at a total 2D MOT cooling power of about 100 mW in a 1×4 cm cell). The slight power inbalance due to the uncoated cell walls can be canceled by the position of the magnetic field coils or magnets.

The magnetic field of a 2D MOT is symmetric along the axis of the 2D MOT. This allows the atoms to freely propagate along the axis of the 2D MOT. The field can be created by long wires configured as shown in Figure 4.9a. In this experiment the magnetic field for the 2D MOT is produced by permanent magnets configured as shown in Figure 4.9b. Sub-Doppler cooling and BEC are sensitive to stray magnetic fields but 2D MOT permanent magnets do not affect these experimental stages because

the quadrupole MOT field falls off faster than $(w/r)^4$ where w is the distance between magnets. In the current experiment $w \approx 2$ cm and $r \approx 10$ cm so the effect of the continuous magnetic field gradient is negligible. Permanent magnets are used because the 2D MOT field is constant during the MOT loading stage and it reduces the number of power supplies needed to operate the experiment. From the standpoint of a practical device reducing the number of power supplies in the system reduces the net weight and power consumption. From an experimental perspective it is worthwhile to simplify the system but it comes at the cost of not being able to optimize the magnetic field gradient for the greatest flux.

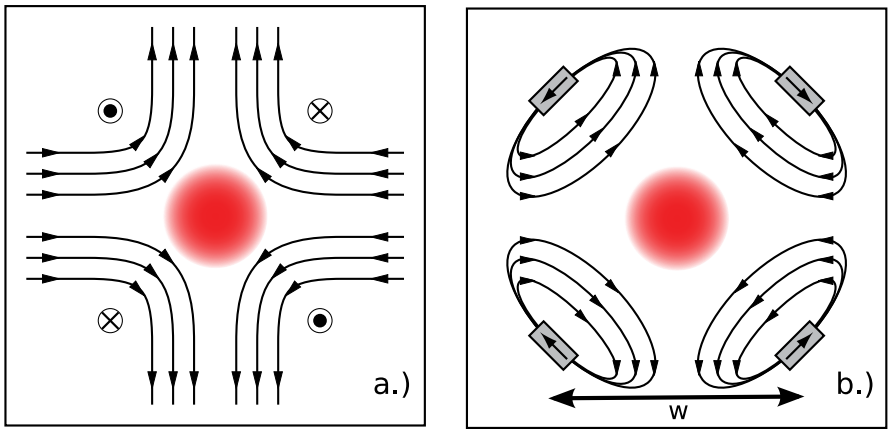

Figure 4.9: Comparison of 2D MOT magnetic field produced with current carrying wires and permanent magnets. Figure a.) shows the field from four parallel wires and Figure b.) shows a similar magnetic field toward the center of the field diagram.

While the 2D MOT magnets do not significantly affect the molasses cooling or BEC production other magnetic fields can affect the pointing of the 2D MOT flux. In particular stray fields from the ion pump magnets have significantly altered the path of the 2D MOT. The interference from the 2D MOT magnets is reduced by improving the magnetic shielding around ion pump magnets. There are a few key elements for shielding the ion pump magnets. First the shielding material should have a high μ to provide a low energy path for the magnetic fields to return to the opposite magnetic pole and a

low residual field after being exposed to an external magnetic field. The low residual field is important because magnetic fields will be switched many times during the course of a BEC experiment and a varying residual field could cause fluctuations from shot to shot. The magnetic shielding should, as much as possible, completely encase the area around the magnets. Because the shielding material has a high μ any magnetic field line that intersects the shielding will have a low energy path to the opposite magnet pole. This can be called a magnetic short circuit. The field lines can escape at any point where there is a direct line of sight.

Finally there should be space between the ion pump magnets and the magnetic shielding. High μ-metals can provide a low energy return path for magnetic fields but are subject to saturation. Saturation happens when all of the magnetic domains in the material align with the external field and cannot increase alignment when the magnetic field is increased. Saturated magnetic shielding effectively loses its high μ properties and will not short circuit magnetic field lines. Saturation can easily be avoided by introducing a gap between the shielding and the ion pump magnets. The air gap allows the magnetic field to spread out so the magnetic-field density is below saturation.

Once the stray magnetic fields have been eliminated the magnetic coils or permanent magnets should be centered horizontally and vertically around the 2D MOT cell. A 2D MOT should be visible when the 2D MOT optics and magnetic field are both centered on the 2D MOT cell. The 2D MOT is most easily seen by looking along the long axis of the 2D MOT with the push beam off so there is maximum integration of the fluoresced signal. It also help to see the 2D MOT when it's moving so the 2D MOT can be moved by translating the 2D MOT coils or carefully moving a magnet around the area of the 2D MOT. The 2D MOT magnet assembly is aligned parallel to the axis of the 2D MOT chamber by centering the 2D MOT cell in the camera's field of view and then focusing the camera on one end of the long 2D MOT and then focusing on the other end of the 2D MOT. If the MOT is parallel to the cell the two ends of the

MOT will be in the same place. If the MOT is angled it can be aligned by adjusting the angle of the 2D MOT magnets. The 2D MOT magnetic structure is typically mounted on a 5-axis stage (XYZ translation + 2 rotational) that allows the the magnets to be precisely positioned. Finally the 2D MOT should be centered relative to the pinhole in the silicon disk.

After the 2D MOT optics and magnetic fields are aligned the push beam is turned on. The push beam overlaps the same axis as the axial imaging camera so it is good to finish the 2D MOT alignment before aligning the push beam. The push beam is aligned by centering the push beam on the bottom of the 2D MOT cell. An iris is the put in the push beam before the final two steering mirrors and is used to retroreflect the push beam off of the silicon disk. The iris should be off-axis so the hole in the center of the silicon does not affect the beam. These two mirrors are iteratively adjusted until the push beam is both centered on the 2D MOT cell and parallel to the silicon disk. The final 2D+ MOT alignment is best aligned with a working 3D MOT to monitor the transfer of atoms to the upper chamber.

4.4.2 3D MOT

The 3D MOT is created with two pairs of beams that are retroreflected (angled beams), plus two counter propagating beams (horizontal beams). While retroreflecting in a 2D MOT improves the MOT performance the same is not true in a 3D MOT because the optical density of a 3D MOT is much higher. A true six beam MOT number is on the order of 10% higher than the retroreflected configuration [91], however in the 3D MOT setup as many beams as possible are retroreflected because the performance difference is small and optical alignment of retroreflected beams is easier. The exception is the horizontal beams because the optical pumping beam (see Section 4.4.5) only propogates along one of the horizontal beam paths. The retroreflected(counter propagating) beams are self(co)-aligned by using an iris to narrow the beam for ease of alignment similar

to the alignment procedure of the 2D MOT. The power in the horizontal beams is balanced with an iris in the beam because the size of the MOT beams is $\sim$ 15 mm and overfills physical size of the power meters. The center of angled beams are easily overlapped with the center of the horizontal beams when the vacuum cell is removed. The cross section and overlap of the beams can be seen on a card placed where the center of the cell would have been. The repump and optical pumping beams are double coupled into the same polarization maintaing optical fiber and are overlapped with the horizontal cooling beams. As mentioned the pumping beam co-propogates with one of the horizontal cooling beams and the repump laser is overlapped with the other horizontal cooling beam. The total MOT cooling power is 28-32 mW, the repump is 6-8 mW, and the optical pumping beam is $\leq$1 mW. More cooling power is available but it degrades the performance of PGC for the available laser detuning [92].

One difference in this MOT configuration compared to other 3D MOT arrangements is the angle of the retroreflected beams. As seen in Figure 2.11 the angled beams are not orthogonal and in the experiment $\theta \sim 20°$. This allows the MOT to be positioned closer to the chip by a factor of 1.6-2 compared to $\theta = 45°$. This reduction in transport distance is significant because the atoms are transported and transfered to the chip with a large external Z-shaped wire. The current required for the transport depends on the transport distance as $1/r^2$. The 25° reduction in angle reduces the current required to magnetically trap the atoms with a large Z-wire by a factor of $1.6^2 - 2^2$. This in turn reduces the dissipated power by $1.6^4 - 2^4$. A Monte-Carlo simulation indicated the beam angle could be reduced (see Figure 2.12) without a reduction in MOT number and in practice the angled MOT has similar performance to a 3D MOT with orthogonal beams. However there are no systematic data taken to compare the MOT performance as a function of MOT angle.

The extent of the testing involved optimizing a six-beam MOT and noting the loading time and number in the MOT. The optical alignment was then modified so

$\theta = 20°$ this included changing several mounts and realigning the retroreflecting optics. Setting the height and angle of the retroreflecting optics is an important detail. The height was determined by simple trigonometry and careful measurement of the initial beam height. The angle of the retroreflecting optics were initially set with a 20° angle block from the machine shop.

After the MOT was configured with angled beams it was optimized for the largest possible MOT number by slightly adjusting the beam alignments and power balancing. The number of atoms in the 20° MOT was essentially the same as a MOT with $\theta = 45°$. There is a caveat to the MOT numbers because it was measured with a CCD camera with an auto gain function. At the time is was assumed that any reasonable MOT would force the camera into a low gain mode making the camera be reasonably accurate for integrated number measurements. A later comparison of MOT numbers using the CCD camera versus a photodiode based measurement showed the CCD numbers were subject to significant error. Given that caveat the apparent size and density of the 20° MOT was the same as the 45° MOT. There was no effort to experimentally map out the MOT number versus θ to compare to Figure 2.12 because of the time it took to realign the MOT at each angle. The lowest possible temperature in sub-Doppler cooling was the other key element besides number that was in question when using angled MOT beams. With the 20° beams the optical molasses stage still cools atoms to as low at 20 μK.

4.4.3 MOT debugging

If the 2D or 3D MOT is not visible there are a few common issues when searching for a MOT in a new setup. First verify there is rubidium in the MOT chamber by increasing the rubidium vapor pressure while illuminating the cell with cooling light. The cooling laser should be scanned over a few hyperfine absorption peaks at approximately 10 Hz. When the rubidium pressure is high enough there should be a noticeable flashing in the MOT cell. Sometime sweeping the laser frequency will also change the intensity

of the laser so it is worthwhile to sweep the laser significantly off resonance to get a feel for the intensity fluctuations of the laser. For a 3D MOT the rubidium pressure should be decreased just below the point of seeing fluorescence. For a 2D MOT the fluorescence should be visible but not too dense because the glow of the background rubidium will make it hard to see the 2D MOT. Verify the lasers are locked on the proper transitions. The cooling laser is particularly sensitive to the locking point. The repump laser locking point is not as sensitive and if there is at least 5-10 mW of repump power the laser can be slowly swept over the $|F = 1\rangle \rightarrow |F' = 2\rangle$ to see a flashing MOT.

The magnetic coils or permanent magnets should create a single zero between the coils for a 3D MOT or a line of zeros for a 2D MOT (see Figure 4.9). The zeros and the magnetic field gradient can be verified with a magnetic field probe. The 3D MOT field gradient is optimized in the 10-14 G/cm range and the 2D MOT is optimized at slightly higher gradients but less than 20 G/cm. The position of the magnetic field zero should be aligned with the desired position of the MOT. This position of the magnetic field zero is most easily determined by the geometry of the coils. For a pair of 3D MOT coils it is the center of the coil pair and for 2D MOT coils it is the center of the four wires or permanent magnets. The width of the coil winding should be taken into account and fixed reference point will help position the coils relative to the cell. For a mirror MOT [26] the magnetic field zero needs to be accurate to less than 1 mm and accurate placement is essential. For a six beam MOT or a 2D MOT in a 1 cm or larger vacuum cell the coils can be centered by eye with reasonable results.

The laser polarization is checked with a simple circular polarization tester made with a quarter waveplate ($\lambda/4$) and linear polarizer rotated 45° relative to the axis of the waveplate. When a right-hand circular (RHC) polarization is incident on the $\lambda/4$ side of the tester the waveplate will convert the polarization from RHC to vertically aligned linear polarized light which will then pass though the linear polarizer. Left hand circular will be rotated to horizontally aligned and will be blocked by the polarization tester.

As a double check the intensity of the beam should be constant as the tester is rotated. If the intensity changes more than a few percent the laser beam is not pure circular polarized but has a significant fraction that is linearly polarized. The polarizations of the various MOT beams are determined by the direction of the MOT magnetic field. Typically a laser polarization is picked for a direction of the magnetic field (e.g. RHC for the magnetic field exiting the coil). Then the polarization of all of the beams that match that same condition are adjusted to be the same. The opposite condition (field entering the coil) is set to the opposite polarization (LHC). It is easy to calculate the polarization needed for a particular magnetic field orientation, but in practice it is very easy to make a minus sign mistake because of the various conventions. If everything else is aligned and there is no MOT it is easy to flip the magnetic field direction by switching the direction of the current in the magnetic field coils. Once a MOT is visible and optimized the magnetic field direction and strength can be measured and depending on the configuration replaced with a set of permanent magnets.

4.4.4 2D → 3D MOT loading

When first looking for a 3D MOT being loaded from a beam out of the 2D MOT it is important to not increase the rubidium pressure in the 2D MOT cell above the typical operating pressure of $\sim 10^{-7}$ torr. Running the 2D MOT cell above this pressure and generally heating the whole vacuum system will force rubidium into the upper chamber. The 2D MOT already runs at high pressure and it would defeat the effect of isolating the two chambers if the 3D MOT chamber was overloaded with rubidium in the initial alignment. If finding the 3D MOT loaded from the 2D MOT is difficult then the 3D MOT should be found and optimized using a single chamber cell at a higher rubidium pressure. Once the optics, polarizations, frequencies, etc. are optimized the single chamber vacuum cell can be traded for the two chamber cell.

A poorly aligned 2D MOT should transfer some atoms into the 3D MOT. Even a

2D MOT with one of the beam pairs blocked has weakly loaded a 3D MOT. Once there is some transfer between the MOTs turn on the push beam. It is not worth optimizing the 2D MOT without the push beam because the optimization of the 2D MOT with and without the push beam is different. The 2D+ MOT is aligned by periodically emptying the 3D MOT and then observing the 3D MOT loading (see Figure 4.10). The MOT number is measured by focusing light from the MOT onto a photodiode and displaying the signal on an oscilloscope for immediate feedback of the 2D+ MOT alignment. Initially the MOT was pulsed by blocking the repump laser with a card. Quickly this transitioned into the Control computer switching the repump shutter but a small amount of light from the repump is reflected from the cell walls which causes a large jump in the photodiode signal and MOT number. Switching the MOT current on and off also empties the MOT and results in a clean photodiode signal. A MOT loading time of 400 ms is good for optimizing the 2D+ MOT. It is long enough to load a noticeable MOT for good signal to noise and is fast enough for optimization. This metric for optimizing the MOT does not optimize the saturated MOT number rather the initial loading rate of atoms into the 3D MOT. However the saturated 3D MOT number strongly depends on the ratio of the MOT loading rate versus the loss rate, so any increase in the MOT loading rate should result in a larger saturated MOT number. The ultimate MOT number not only depends on the ratio of loading and loss rates, but photon reradiation and the maximum MOT density [32, 93].

The 2D→3D MOT optimization is an iterative process and typically starts by adjusting the position and angle of the 2D MOT magnetic field with the push beam. The lateral position of the magnets is scanned until the maximum loading rate is found. The angle of the magnets corresponding to the translation axis is then slightly rotated. The lateral position is then scanned again to find the maximum. If the rotation reduced the atom number then the magnets are rotated the opposite direction. This process is iterated until the any rotation or translation results in a reduction of the loading rate.

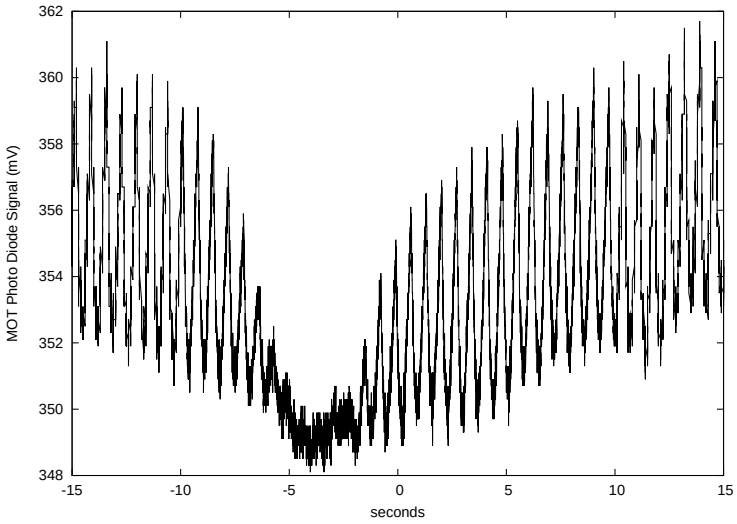

Figure 4.10: Example oscilloscope trace of optimizing the push beam power. The MOT coils are switched on for 400 ms and then switched off for 300 ms. This leads to the pulsed trace that approximates the loading rate of the 2D MOT into the 3D MOT. At t = -15 s the push beam power is nearly optimized, as a check the power is changed by rotating a half waveplate in front a polarizing beam splitter cube immediately before the 2D MOT cell. As the power drops the 3D MOT loading rate and number significantly drop around -5 s. As the waveplate is rotated back the MOT loading rate and number are optimized by adjusting the waveplate to have the largest possible swing.

This same process is repeated for the other lateral axis of the 2D MOT magnets. It is possible that this alignment procedure will significantly change the magnet alignment, but this is typically not the case. If for some reason several adjustments significantly decrease the loading rate then it is best to recenter and align the angle of the magnets as best as possible by eye and then optimize the MOT.

Next adjust the position and angle of 2D MOT cooling beams, power balancing, and quarter waveplates. These adjustments should be incremental because of the alignment performed in Section 4.4.1, but small tweaks will typically improve the MOT number. Any adjustment to the vertical position of the 2D MOT beams should be checked to make sure all of the beams are at the same height and are not scattering off of the silicon disk at the top of the 2D MOT cell. The 2D MOT push beam is optimized by adjusting the angle and position of the push beam in small increments.

The optimized 2D→3D MOT loading is most sensitive to the push beam power. The optimal push beam power is typically a few mW for a 1 cm^2 beam.

After the 2D MOT beams are aligned the 3D MOT can be adjusted. The initial placement of the MOT coils is done with the bias coil power supplies turned off. The MOT coils should be centered and parallel to the MOT cell but can be translated to optimize the number and shape of the MOT. After the MOT and bias coils are fixed to the table the MOT can be moved over a wide range by applying a bias field in the appropriate direction. Before optimizing the bias field values the magnetic field should be calibrated. This basic process is explained in Reference [14]. Once the zero point and B vs. I slope is determined the Zero and Five points are saved in a calibration file in the Control program. See Section 4.3.1 for details of how to determine and set the Zero and Five points. It is important to perform this calibration before optimizing the position of the MOT because changing the bias field calibration will shift the position of the MOT. The MOT position is adjusted for maximum number and shape by adjusting the bias fields.

After the optimal MOT position is set by the bias fields the cooling beams, powers, and polarizations can be slightly adjusted for MOT number and shape. Assuming the 3D MOT cooling beams have been power balanced, overlapped, retroreflected then only small adjustments to the MOT beams should be required. The MOT number and shape can be improved from the basic alignment but large alignment changes will affect later laser cooling stages. In particular the power balancing of the horizontal beams should not be adjusted because the optical molasses is sensitive to power balancing. The relative power balancing between the horizontal and angled beams will change the aspect ratio of the MOT. The MOT should be close to spherical but can be slightly elliptical when optimized for maximum number. All of the 3D MOT alignment is performed with the 3D MOT being loaded from the 2D MOT flux or in a single chamber cell where a high rubidium vapor pressure will not degrade the overall vacuum pressure.

Optimizing the overall MOT loading rate is an iterative process and all of the above steps should be repeated a few times with finer adjustments being made after each iteration. When the 3D MOT is loaded to maximum number sometimes the 2D MOT beam can be seen distorting the 3D MOT. This signature is not a specific sign of a well aligned 2D MOT flux and at the same time it is not a bad sign. The real metrics for optimization are the MOT loading rate, the maximum MOT number, and the visual appearance of a smooth well connected MOT.

The 2D+ $\rightarrow$ 3D MOT transfer also depends on the rubidium pressure in the 2D MOT chamber. The pressure in the 2D MOT cell should be maintain at the highest possible rubidium pressure without significantly increasing the pressure of other gases in the BEC cell. There is an optimal rubidium dispenser current where the ratio of rubidium to all other gases is maximized. This operating current I_{op} is best found experimentally because it varies dispenser to dispenser and with thermal load. The 2D MOT cell is also heated to increase the rubidium pressure without increasing the dispenser current above I_{op}. This does not significantly increase the total pressure because the vapor pressure of rubidium is a strong function of temperature while the other gases (hydrogen, helium, etc.) effectively have negligible temperature dependence at laboratory temperatures. Thus the MOT loading rate is optimized without compromising the MOT lifetime. This shows that the differential pumping allows the pressure in the 2D MOT chamber to be raised to a certain point without significantly affecting the pressure in the 3D MOT cell. This depends on the pressure in the 2D MOT cell, the size of the aperature, and the pumping speed in the 3D MOT cell. Above some pressure in the 2D MOT cell the pressure differential can not be maintained by the pumps in the 3D MOT cell and the MOT lifetime drops (see Section 2.5). In principle a longer differential pumping tube could be used to increase the pressure differential between the cells but the current design errors on the cautious side so the atom flux is not significantly limited by the tube or aperture.

4.4.5 CMOT, PGC, OP

After the 3D MOT is loaded, the atoms are compressed and cooled by a compressed MOT (CMOT) [37]. The CMOT compresses the atoms by increasing the field gradient from 10-14 G/cm to 20-30 G/cm. At the same time the atoms are further cooled by detuning the cooling laser frequency from 2Γ to $4-5\Gamma$ and reducing the repump power. During the CMOT the atoms are moved toward the chip by a B_z field to reduce the distance the atoms must be transported to the chip. The maximum distance that the atoms can be transported is initially determined in steady state by increasing the magnetic-field gradient but leaving the cooling frequency at 2Γ. The maximum displacement of the CMOT is be determined by the CMOT shape and relative number. As the CMOT is translated the X,Y, and Z bias fields are adjusted to center the CMOT in the MOT cell. This procedure maps out the general magnetic field behavior and the alignment of the MOT beams. The cooling and repump lasers may need to be slightly adjusted to optimize both the MOT and CMOT. It is important to optimize the shape of the CMOT (i.e. a smooth well connected MOT) because the optical molasses stage will be optimized at this position. The atoms are displaced (5-10 mm) to the final CMOT position in 20–40 ms. If the atoms were transfered this quickly in a magnetic trap it would introduce a significant slosh mode in the atom cloud. This does not happen when moving the atoms in the CMOT because the CMOT is a dissipative trap.

The bias fields needed to transport and center the CMOT can be initially determined with a steady state CMOT, but the final behavior of the CMOT is transitory and optimization requires imaging the atoms via adsorption or fluorescence imaging. Adsorption imaging is used exclusively to evaluate the CMOT optimization. Typically the atoms are allowed to expand for a few ms to qualitatively determine the atom temperature because hotter atoms in the cloud expand more when the trapping fields are turned

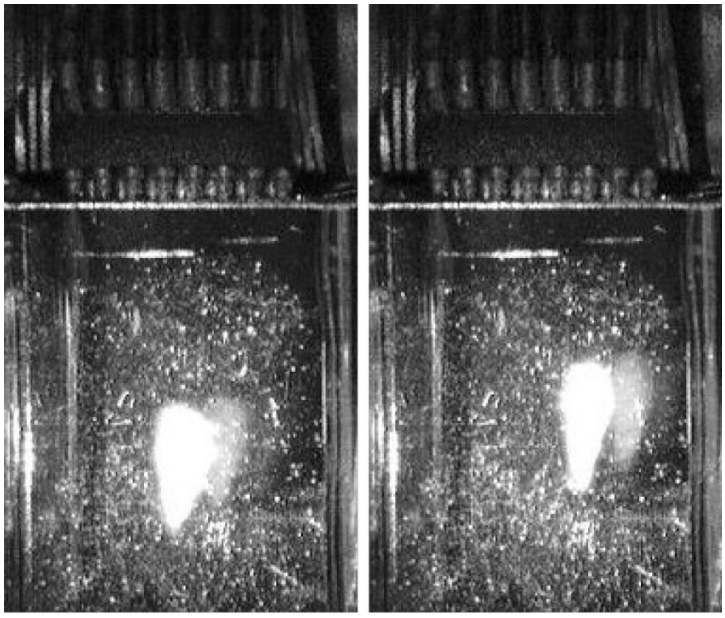

Figure 4.11: Images of maximally loaded MOT (a) and translated CMOT (b) in a 2 cm cell. The translation and differences in size and shape of the two MOTs can be seen. Additionally the atom chip can be seen sealing the top of the cell and the spring loaded pins for making connections to the external pads can be seen above the atom chip. Three loops of the compression wires can be seen outside of the spring loaded pins.

off. This ballistic expansion is typically known as time of flight imaging (TOF). After a long TOF (the linear expansion regime) the size of the cloud is directly proportional to the temperature of the cloud. The temperature of the CMOT and optical molasses are optimized by imaging the atoms after a long TOF and then optimizing the various cooling parameters for the smallest cloud size while maintaining atom number. While compressing the atoms increases the transfer into the magnetic trap it is important to reduce the temperature of the atoms after the CMOT to $\sim$125 μK in preparation for optical molasses. The temperature of the CMOT depends on the detuning of the cooling lasers, the repump power, and the total CMOT time. When the CMOT is positioned at the center of the lasers it is relatively easy to achieve temperatures below 125 μK. However, when the CMOT is positioned in the outer extents of the lasers achieving lower

temperatures is not as simple. In the displaced condition the final CMOT temperature can be reduced by increasing the cooling laser detuning to 10-11 Γ in the last 1–2 ms, with the magnetic field and repump power being held at the same values.

After the CMOT the atoms are then further cooled by optical molasses also known as sub-Doppler cooling or polarization gradient cooling. In a typical MOT the overall lowest attainable temperature is 140 μK and is typically called the Doppler limit [94]. There is some sub-Doppler cooling near the magnetic field zero but it is only in a small region of the MOT. The Doppler temperature is determined by the balance between cooling via the Doppler shift and heating due to reradiated photons. In a CMOT the temperature can be lower than the Doppler limit because the photon heating is suppressed by detuning the laser [37]. The final temperature after optical molasses in the current experimental setup is 40 μK. This is far above the theoretical limit of 4 μK but more than adequate for magnetic trapping on a chip. There are BEC experiments that do not use optical molasses [6, 95]. These experiments are typically use large coils to create deep magnetic traps, however in the chip and external-Z wire based magnetic traps the trap depth is approximately an order of magnitude less than the macroscopic traps. Reducing the temperature of the atom cloud below 80-100 μk significantly improves the initial loading of the magnetic trap.

Optical molasses is the most sensitive of all post-MOT loading cooling steps. It is sensitive to zeroing the bias fields to the tenth of a Gauss level and depends on the repump power and the cooling laser power [92]. Similar to the CMOT optimization the optical molasses is optimized by imaging the atoms after TOF (typically 5-15 ms). The cooling laser is typically set to 11 Γ detuning, all of the bias fields are set to zero (assuming they are calibrated), the MOT magnetic field is set to zero, and the optical molasses time is 3-5 ms. The optical molasses should be optimized with power balanced cooling beams or the atoms will cooled in a moving reference frame. The power balancing can be tested by increasing the optical molasses stage time to 10-15 ms

and looking for the atom cloud to be pushed off center. The power in the cooling beams is adjusted until the atoms remain centered. The optical molasses is then optimized by varying the magnetic field, laser power, laser detuning, etc. for the minimized cloud size. The value where the size of the cloud is smallest is the new optimal value. Similar to aligning the CMOT this is an iterative process of varying all of the parameters to find a new set of optimal values. The same parameters are then varied again, preferably in a different order, to further optimize the optical molasses. As stated above it should be relatively easy to reduce the temperature to 40 μK or less.

The final step before the magnetic trap is optically pumping the atoms into the strong field seeking state. Immediately after or a few 100 μs before the end of optical molasses the cooling light is turned off to avoid pumping atoms into a random m_F states. It is important to measure the time when the cooling laser switches off with a photodiode because there is an unknown delay between when the signal is sent to the shutter to the point when the shutter occults the laser. The atoms are optically pumped into the $|2,2\rangle$ state with the pump beam slightly detuned from the F=2→F'=2 transition. The laser is directed though the cloud in only one direction determined by the B_x field. The B_x field shifts the atoms into resonance with the pump laser and defines a quantization axis. The repump laser is left on to pump atoms out of the F=1 state. Optical pumping is optimized after seeing at least a small magnetic trap. Optical pumping is sensitive to B_x, the repump power, and the pumping power. While B_x and the repump power are varied via the control software the pumping power is set by hand in order to reduce the number of DAQ channels. Unfortunately the optical pumping power drifts over time, especially because the optical pumping beam is double fiber coupled with the repump laser. In the current experimental configuration there is no passive or active monitoring of the pumping optical power. For improved BEC production stability, on the time scale of days, the optical pumping power should be monitored to maintain the same power.

4.4.6 External Z-wire magnetic trap

The initial magnetic trapping, transport, and coupling of atoms onto the chip are accomplished with a Z-shaped wire (see Figure 4.15) positioned just above the atom chip. The main reason for using a Z-shaped wire is to improve mode matching to the chip Z-wire trap. The external Z-wire has essentially the same shape and magnetic field as the chip Z-wire trap. In the adiabatic transfer limit the size and shape of the Z-wires would smoothly transfer from a slightly larger wire to a slightly smaller wire. In this limit there would be no atom loss and the adiabatic compression requirements would limit the transfer speed. In reality the change in size from the external Z-wire trap (width$\sim$32 mm) to the chip Z-wire trap (width$\sim$17 mm) is not adiabatic and the transfer efficiency is less than 100%, but has been as high as 70-80%. Other atom chip experiments with a six-beam MOT have reported low transfer efficiency ($\leq$ 50% often $<$ 25%) from a quadrupole magnetic trap to the chip magnetic trap [13, 43, 42].

The external Z-wire is constructed by shaping a piece of enamel coated magnet wire into a Z-shape with long tails and then flattening the center section with a hydraulic press. The wires are flattened so the center of the current distribution is closer to the position of the atoms inside the cell (see Section 2.2.1) and it is easier to stack the wires. Flattening the wires must be done with some caution, because deforming the wires beyond a certain point will crack the enamel coating on the wire. The maximum deformation of the wires is determined empirically because it depends on the type of coating on the wire. The total area of the wire that can be flattened depends of the maximum pressure of the hydraulic press. In our experimental setup only the center 10 cm of the wire could be flattened. This makes a transition region where the wire changes from rectangular to round. Despite the abrupt transition the Z-shaped wires are robust, however any break in the wire is typically at the flat to round junction so care must be taken when bending the wires. The first wire is bent around a rectangular

form (see Figure 4.12a) and is held in place with tape. A second wire is then bent over the first wire and is also taped in place. This is repeated for five wires to increase the total effective current for maximal magnetic field gradient and trap depth. For a given power supply the limit to the number of wires is the resistance of the Z-wire coil and the voltage of the power supply. After the wire are bent around the form each is checked for shorting to the other wires and the form. The wire are epoxied (EpoTex 383ND) to the form to maintain shape and for a mounting point. The leads of the wires are then soldered in series with the total height of the external Z-wire and return coil is 18 cm (see Figure 4.12a). Also attached to the eternal Z-wire mounting block are the spring loaded pins plus leads, the compression wires, and the RF coil (see Figure 4.12b).

4.4.6.1 Switching mode power supplies

The external Z-wire is driven by a switching mode power supply (Xantrex XHR series 130A/7.5V). The current in the external Z-wire needs to be switched on the order of 1 ms and to be continuously varied so the atoms can be transported from the final CMOT position to the chip and adiabatically transfered to the chip. The XHR power supply has an internal current control mechanism that can be used to control the current, however there is a delay of 25-75 ms between the time when the signal is sent to the power supply to when the current output changes. In principle this delay can be subtracted out in the control system timing file, unfortunately the power supply updates the current every 25-75 ms leading to a chopped waveform that would be unacceptable for transporting a cold cloud of atoms.

Instead of using the internal control circuitry the external Z-wire crrent is controlled by a current servo (similar to the circuit in Reference [96]) driving a fan cooled MOSFET bank (IRFP3703). These MOSFETs can drive 130A for a few hundred ms but care should be taken because MOSFETs short circuit when they fail and will continue to conduct current until the MOSFET burns/melts. The MOSFET bank can support

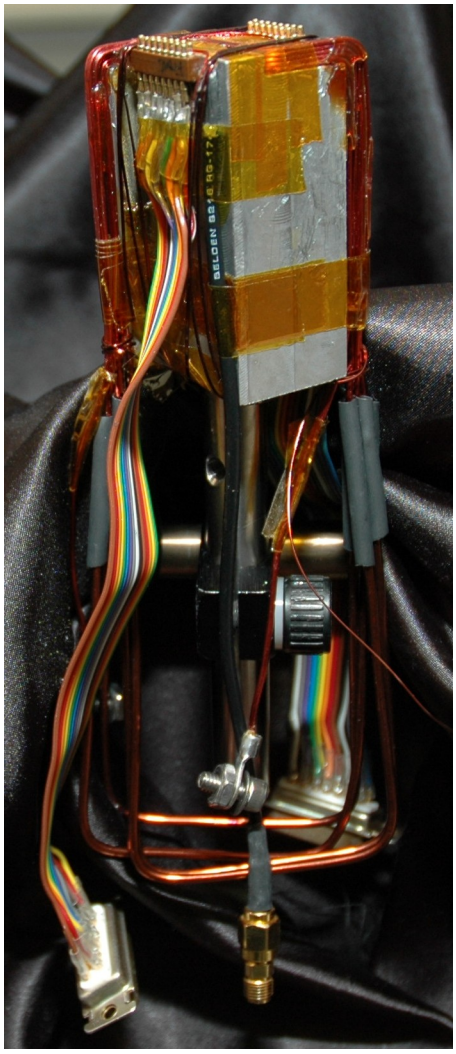
a.)
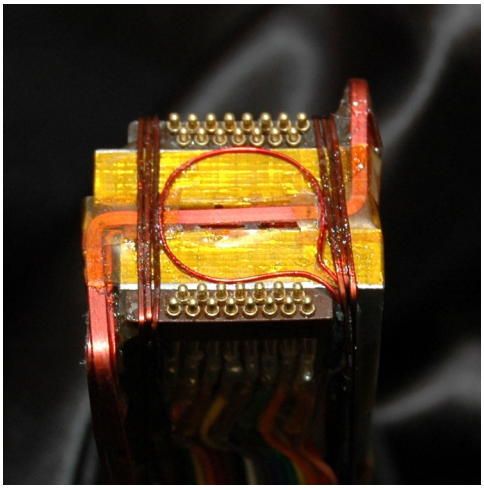
b.)

Figure 4.12: Pictures of the external Z-wire assembly. Five flattened Z-shaped wires (originally 16 AWG) are bent around an aluminum form and then connected in series to effectively increase the total trapping by a factor of five. Spring loaded pins are press fit into a piece of Vespel, soldered to ribbon cable, and then epoxied to the side of the aluminum block. A single turn of 22-24 AWG wire forms the RF coil. The diameter of the coil is large enough that it does not contact a 1 cm silicon disk that is epoxied to the back of the atom chip. The compression wires are two sets of three parallel wires just outside of the RF coil and parallel to the legs of the external Z-wire. The top of the aluminum block is tapped for an 8-32 screw and the assembly is mounted to a 0.5" post that is then attached to a frame around the cell.

up to 50 A for >5 s repeatedly but have failed for times longer than 7 s. During typical operating conditions (< 1 s) no discernible heat is transferred from the external Z-wire to the cell structure.

Even though this high current driver can control a commercially available power supply this setup effectively duplicates the high power control circuitry. Switch mode power supplies (SMPS) are known for better conversion efficiency than linear power supplies, but it comes a the cost of additional high frequency noise. Switch mode power supplies are efficient because they chop the voltage to a transformer with a MOSFET at high frequencies, typically 100's of kHz, and then low pass filter the signal to remove the high frequency chopping. This is efficient because the switching MOSFET dissipates no power when it is full off and dissipates very little power when the MOSFET is full on. The output current/voltage is controlled by pulse width modulating the control signal to the MOSFET. If the power supply is supposed to deliver full voltage then the MOSFET will be continuously on. If the voltage is set at 50% of the max voltage then the MOSFET will be switched on for half of the time and off for the other half of the time. When this chopped waveform is low pass filtered the resulting voltage is half of the max voltage with a small amount of ripple. From an eletrical design perspective a SMPS is more complicated to build, but there are many companies that sell high quality SMPS that are more cost effective than a linear power supply with the same voltage and current.

The real issue with SMPS in BEC experiments is noise. The electrical signal is chopped at 100's of kHz and this noise could cause parametric heating. Fortunately typical SMPS frequencies are in a 'sweet' spot for use in BEC experiments. There are basically three regimes where noise would cause significant heating or loss. They are the 1-200 Hz range for weak magnetic traps, 1-5 kHz for tight magnetic traps, and 1-100 MHz for transitions between hyperfine levels in atoms. The SMPS frequency is at least one order of magnitude away from all of the critical frequency bands. Because of this

SMPS can be used for high current applications like magnetic trap transfer and may even be suitable for BEC power supplies.

How could the current configuration be better? In the current setup the pulse width modulation servo that drives the output of the SMPS is set to maximum voltage and the external servo drives a MOSFET bank as a linear control so there are two servos controlling the same power supply. The linear MOSFET operates at a low duty cycle so there is little heating, but ideally the pulse width modulation servo would be directly used to control the current. Actually a current to voltage converter (shunt resistor or Hall probe) would be used to provide control feedback to the power supply. This would most likely involve significant modification of the SMPS electronics and limits the casual modification of a SMPS but these modification could be important for future applications. From the experimental point of view it is reasonable to treat the SMPS like a high current battery and build a linear servo to control the current.

4.4.6.2 Initial external Z-wire trap

The initial external Z-wire magnetic trap condition is found by exploiting the Zeeman shift of the atoms in the magnetic trapping field. The external Z-wire current is turned to the maximum value and B_y to some value. The hold time is 1–2 ms, long enough that the fields have reached their final values but not too long such that the atoms are moving in the magnetic trap potential. An absorption image is taken with the probe laser on resonance with the $F = 2 \rightarrow F' = 3$ transition. Atoms that are in the weakest field will scatter the most light and show the greatest signal on the absorption image. By varying B_y the vertical position of the magnetic trap is moved though the position of the atoms. The B_y field with the largest apparent number is where the minimum of the magnetic field overlaps with the cloud center (see Figure 4.13). The other bias fields can be optimized in the same way but they are not as important as B_y in the initial alignment of the external Z-wire magnetic trap.

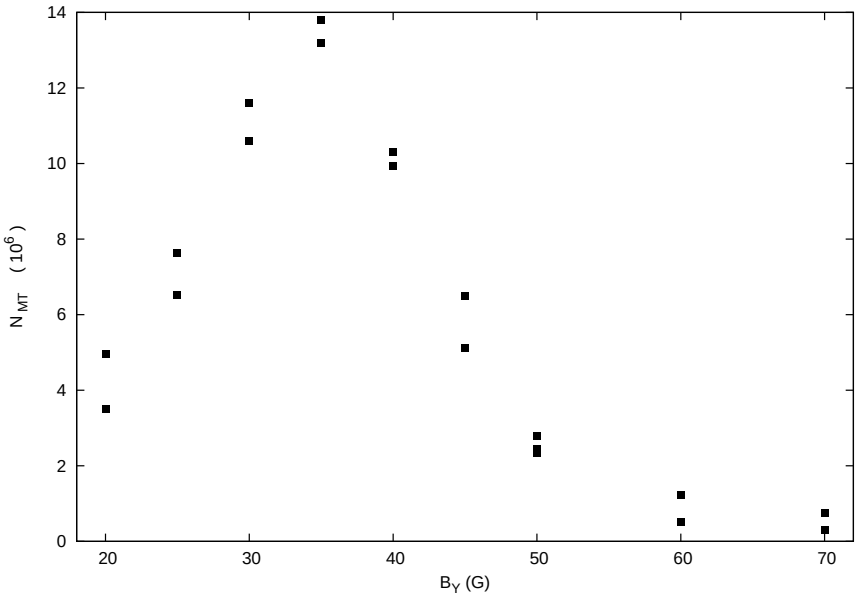

Figure 4.13: Example data showing parameter search for the initial external Z-wire magnetic trap by imaging the atoms with a resonant probe laser immediately after the external Z-wire magnetic trap is turned on. Atoms that are positioned away from the bottom of the magnetic trap will be Zeeman shifted out of resonance and will not contribute to the signal. The B_y with the greatest signal is the starting parameter for the next optimization. In this example the external Z-wire is turned to 120 A while B_y is varied in each shot.

4.4.6.3 External Z-wire magnetic trap optimization

Once atoms are in a magnetic trap there are several optimization steps. The initial magnetic trap curvature is empirically matched to the size and temperature of the atoms. This can be accomplished two ways: the ratio of the B_y and the external Z-wire can be varied together or B_x can be varied to change the trap bottom and loosen the trap frequency at the bottom of the trap. Both methods will reduce the trap gradient and depth, but increasing B_x will relax the trap gradient only around the trap bottom and will leave the gradient nominally the same at other locations. In the initial external Z-wire magnetic trap it is important to maintain a high trap gradient to hold atoms against gravity so the longitudinal bias is increased to reduce the trap frequency because it leaves a higher gradient at regions away from the trap bottom.

The initial position of the atoms when they are captured in the magnetic trap is varied by adjusting the final bias field of the CMOT. There are two critical axes: the first and most obvious is the B_z field that adjusts the vertical position of the CMOT. Increasing B_z will move the atoms closer to the chip which should improve the initial external Z-wire magnetic trap. However, moving the atom up in the optical fields changes the optical intensity experienced by the atoms and can affect atom number and temperature after optical molasses. On the flip side if the atoms are too far away then the magnetic-field gradient of the external Z-wire will not be able to capture a significant fraction of the atoms. Additionally changing the position of the CMOT without changing the position of the initial magnetic trap will reduce the transfer efficiency. Given these constraints the CMOT B_z is easily optimized; A reasonable B_y is picked for the initial external Z-wire magnetic trap and then the CMOT B_z is varied to map the transfer efficiency. Change B_y and again sweep B_z until the parameter space has been mapped out and the optimal final CMOT and initial magnetic trap parameters are determined. The other parameter that affects the transfer to the chip magnetic trap is the CMOT B_x field that determines the position of the atoms along the weak axis of the trap. Atoms that are displaced along the weak axis of the trap will be excited into a low frequency slosh mode. While this may seem trivial because it is not along the tight axis of the trap at low frequencies it takes several periods at the longitudinal oscillation frequency to damp out. The oscillation is most detrimental when the atoms are transfered from the external Z-wire magnetic trap to the chip Z-wire magnetic trap because of the width mismatch between the Z-wires. If the atoms are longitudinally sloshing they can be caught outside of the chip Z-wire width and be lost. The CMOT B_x is optimized by measuring the longitudinal position of the cloud a various times and adjusting the CMOT B_x field. This is a necessary step before the atoms are transfered into chip Z-wire magnetic trap. After some atoms are transfered into the chip Z-wire magnetic trap the CMOT B_x bias is optimized by maximizing the number in the chip

Z-wire magnetic trap. The CMOT B_y value can be varied but the atom number of the various magnetic trapping stages is not a strong function of the transverse displacement.

The transfer efficiency into the initial magnetic trap depends on the turning on timing of the external Z-wire and the B_y bias field. If the fields are ramped faster than the Larmor frequency it will cause significant loss because the atoms will have a random m_F projection on the new magnetic trapping field. To prevent this a small bias field (typically 1-2 G of the B_x field from optical pumping) is maintained during the initial magnetic trap. Because the Larmor frequency is a relatively high (1.4 MHz/G for the $|2,2\rangle$ state) a fraction of a Gauss is sufficient for atoms to adiabatically follow the changing magnetic field. The other consideration is the different time constants to ramp on the external Z-wire on versus the current in the B_y coil. If the currents ramp on at different rates the position of the initial magnetic trap will be swept around the area of the atoms. The movement of the initial magnetic trap is reduced by individually optimizing the external Z-wire and B_y ramping rates for optimial number and cloud temperature. The initial ramping time is on the order of 1 ms.

4.4.7 Transfer to chip

Once the atoms are magnetically trapped they are transfered to the atom chip where they are evaporatively cooled. The atoms are transfered to the chip by adjusting the ratio of I_{EZ} and B_y. Initially B_y is increased because it moves the atoms closer to the chip and at the same time increases the depth of the magnetic trap. Then I_{EZ} is reduced to bring the atoms even closer to the chip and to reduce heating in the external Z-wire and the power MOSFETs. See Figure 4.14 for a typical currents and bias fields during initial magnetic trap and transfer to the chip. Ramping the various currents and bias fields is done slowly relative to the trap frequencies of the external Z-wire trap to avoid inducing a slosh mode in the cloud. A weak transverse slosh mode will not significantly affect the behavior of the atoms in the eternal Z-wire magnetic trap,

but any transverse slosh mode present during transfer to the chip Z-wire will cause significant heating and atom loss. The B_x field is varied as the atoms move close to the chip and the external Z-wire wire to maintain a single magnetic trap. If B_x cancels the field from the endcaps of the external Z-wire then two traps will be formed close to the endcaps of the external Z-shaped wire.

The atoms are typically transfered to approximately 300 μm from the chip in the external Z-wire magnetic trap. While the external Z-wire can support significant amounts of current the maximum trap compression is significantly less than compression achievable with wires on the chip. The chip is a 400 μm thick silicon wafer with a silicon oxide layer for electrical isolation. The wires are formed by electroplating copper in a photoresist mold that is the shape of the wire pattern. The chip is patterned with a 15 mm wide Z-wire with crossing wires every 1 mm (see Figure 4.2). The resulting wires are nominally 10 μm tall and 100 μm wide and can continuously support 5 A for several minutes in ambient. Previous tests had shown that approximately 10×100 μm wires on aluminum nitride can maintain 4.5 A under vacuum before failing [14]. Based on those results the total current in any part of the wire pattern is maintained below 4.5 A for long times (i.e. evaporation). The total current includes the wire crossing where the current in each part of the cross may be less than 4.5 A but the total current in the junction is greater than 4.5 A. In previous BEC experiments [1, 14] the chip is epoxied to a quartz cell with the spaces in the wire pattern being sealed by epoxy. In this setup the outer edge of the silicon chip is anodically bonded to the Pyrex 3D MOT cell. Instead of the electrical connections being made though the epoxy seal the electrical connections are made **t**hough the silicon chip by UHV compatible vias. These vias are make by Teledyne Scientific and Imaging LLC (formerly Rockwell Scientific) by a proprietary process. Each via is actually an array of several hundred small (a few μm^2) vias that are connected by an metal overlayer. Each via can support 2.5 A and the vias locations can be joined together to support higher currents. For the chip pattern

used in this thesis the largest chip-Z is connected to two vias and can support up to 5 A (see Figure 4.2). The remaining wires are each connected to a single via and can support 2.5 A. A wide variety of IP, quadrupole, dimple, and waveguide geometries can be configured depending on where the current is sourced and sunk. The areas between the copper wires are filled with "optical metal" (shown in Figure 4.3a) that could be used as a mirror surface.

The UHV vias connect the vacuum side wires to the ambient air, but power supplies need to connect with the chip in a way that is compatible with anodic bonding, the bakeout process, and does not apply stress to any unsupported region of the chip. The air side pads are positioned directly above the cell wall so the majority of the pad is supported by the cell wall (see Figure 4.3b). Soldering and conductive epoxy were both considered but rejected because of reproducibility and high temperature stability. Silver loaded epoxy will handle 4 A of CW current for more than a day and can be applied after bakeout with little applied force or heat. However it is difficult to apply the epoxy reproducibly to the pads on the back of the chip without shorting neighboring pads. Soldering connectors to the back of the chip is a higher risk process and should be done prior to final assembly. However typical solder melts below the bakeout temperature of 300°C. Higher melting temperature solders were not used to avoid thermal gradients across the chip. Additionally each of these methods permanently modifies the chip pads and are not compatible with rebaking cells. Instead of permanently attaching connectors to the chip spring loaded pins (MILL-MAX M09922), held in a machined piece of Vespel, are used to connect to the chip. The pins provide good contact without excessive force and can be easily changed and reused. In the current experiment the Vespel holder is epoxied to the external Z-wire so the entire apparatus is referenced to the air side electrical pads (see Figure 4.3b).

Transferring from the external Z-wire to the chip Z-wire is relatively simple because the shape of the two wires is the same except for their sizes. In principle trans-

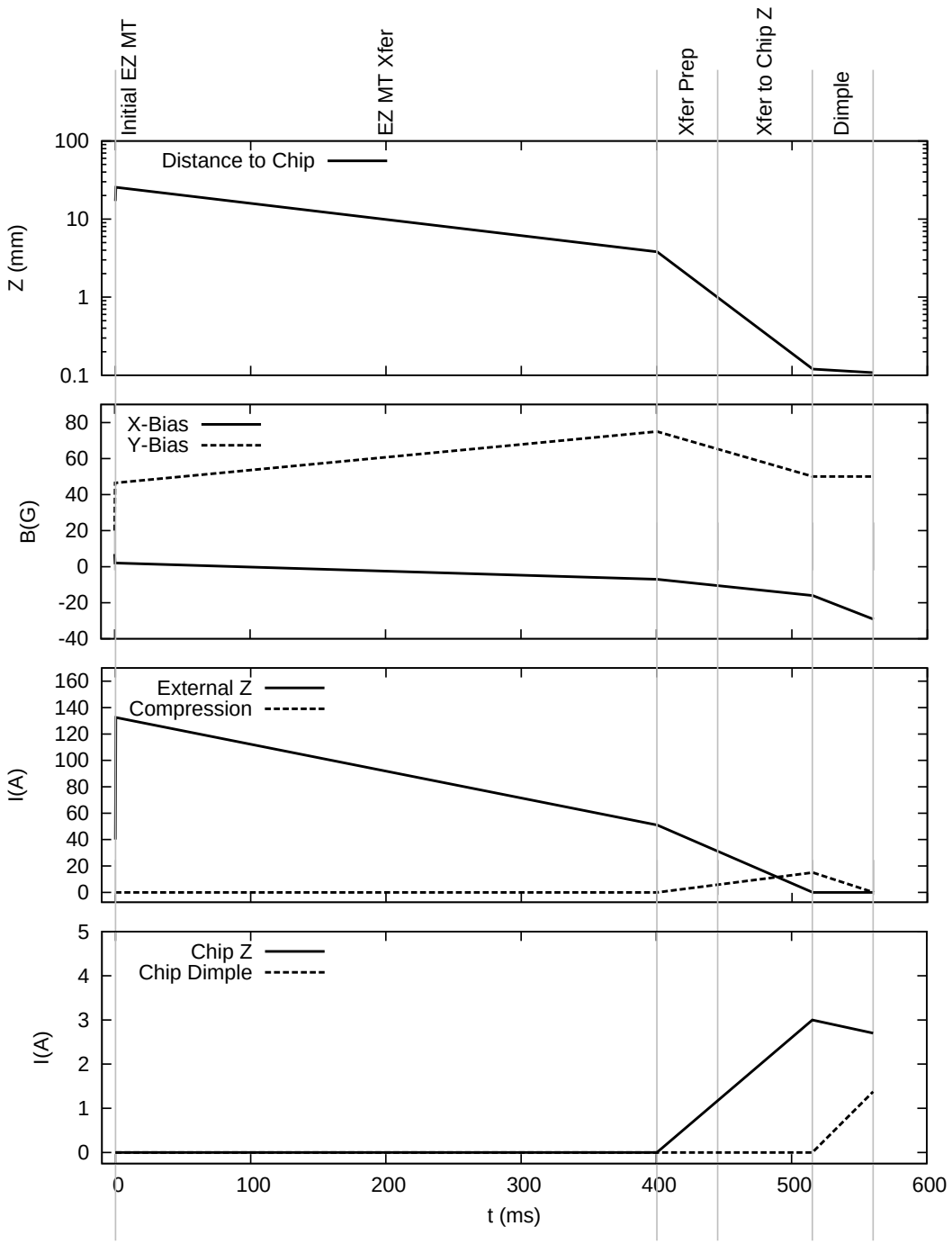

Figure 4.14: Basic timing of the initial magnetic trap, ramping atoms to the chip, adjusting the external Z-wire magnetic trap for transfer to the chip, transfer to the chip, and compressing atoms in the dimple. This shows the calculated distance from the chip surface, the B_x and B_y bias fields ($B_z = 0$), the currents in the external Z-wire, the compression wires, the chip Z-wire, and the dimple wire.

fering from one Z-wire trap to another Z-wire trap should be optimal for a wide variety of parameters but the transfer is surprisingly sensitive to B_y because for a fixed chip current B_y will determine the final height of the chip Z-wire trap. If B_y is too large the atoms will be non-adiabatically transfered into the chip magnetic trap because the trap gradient scales as r^{-2} and there is a factor of four difference between the heights of external Z-wire and the chip Z-wire. The rapid change in trap frequency at this point of the experimental process is more sensitive to sloshing and breathing modes than at any other experimental step. The causes and process for eliminating these modes is explained in Section 4.4.6. A non-adiabatic transfer and/or sloshing/breathing modes are manifest by heating and large number loss in the transfer to the chip magnetic trap.

The transfer between two similar Z-wires is affected by the relative change in width between the two Z-wires and in the current experimental setup the change in width is too large for optimal transfer. An additional set of wires that parallel the Z-wire endcaps aids the transfer from the external Z-wire to the chip Z-wire as seen in Figure 4.15. The additional wires were added to the external Z-wire assembly after the chip and cell were built and baked out. The ease of adding these wires (a few hours) demonstrates the flexibility of having a chip seal the vacuum because the atoms are close ($<$1 mm) to the ambient where significant experimental modifications can be made without making significant changes to the vacumm system. While the compression wires significantly improve the unoptimized transfer of atoms into the chip magnetic trap the improvement for an optimized magnetic trap is $\sim$10%. The small improvement in the transfer effeciency by using compression wires shows the robust nature of transfering between two Z-wire magnetic traps even when the change is width is nearly a factor of two (32 mm to 17 mm).

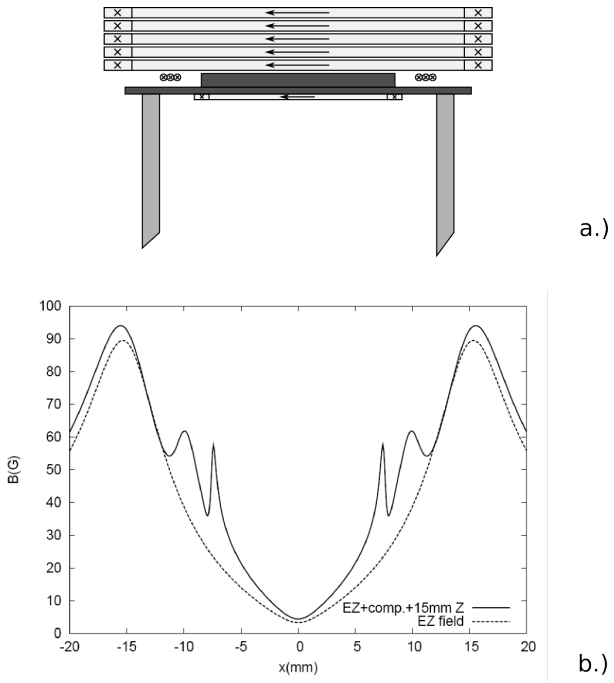

Figure 4.15: Figure a.) Show the relative placement of the external Z-wire, the compression wires, and the chip Z-wire relative to the chip plus backing plate. Figure b.) shows mode matching the external Z-wire field to the chip Z-wire with the addition of the compression wires.

4.4.8 Chip Z

Once the atoms are transfered from the external Z-wire magnetic trap into the chip Z-wire magnetic trap they are compressed close to the final transverse trap frequencies. Even though the transfer from the external Z-wire trap happens at a modest compression for the external Z-wire trap ($\omega_\perp \sim 75$ Hz, $\omega_\parallel \sim 5$ Hz), the initial chip magnetic trap is tight compared to macroscopic trap standards ($\omega_\perp \sim 1$ kHz, $\omega_\parallel \sim 10$ Hz). The B_y bias field and the chip Z-wire current are essentially at the final trap values but the B_x field is configured for loading the dimple trap and reduces the transverse trap frequency at this point in the trap compression. For other experiments that use Z-wire magnetic trap to make BEC see References [1, 10, 13, 18].

4.4.9 Dimple

Once the chip Z-wire trap has been loaded the dimple trap is turned on by increasing B_x and I_d [26]. Using a dimple trap significantly increases the compression of the longitudinal trap frequencies typically from a few Hz to nearly 1 kHz. However not all of the atoms will be trapped in the highly compressed dimple. Atoms not trapped in the dimple will still be trapped by the chip Z-wire magnetic trap but will have a low collision rate and will not significantly contribute to the high speed evaporation. In some of the evaporation schemes (see Chapter 5) these atoms are quickly (< 100 ms) evaporated away in the first evaporation sweep that starts at 50 MHz. In other evaporation schemes the upper lying atoms are ignored and the first evaporation sweep starts in the middle of the Boltzmann distribution (typically about 33 MHz) and assumes the higher lying atoms will eventually be ejected from the trap. A fast evaporation from 50 MHz to the mid 30 MHz improves the overall number and temperature and is worth the extra 100 ms. A combination of the chip Z-wire and the dimple parameters define the trap bottom and changes to either can significantly change the bottom field thus

affecting the RF knife (see Section 2.3.1). Making large changes to the chip Z-wire or dimple traps is avoided when performing RF evaporation to avoid changing the trap bottom.

The optimization of chip Z-wire and dimple compression is essentially the same. The magnetic trap parameters (chip Z-wire current, B_y, etc.) are chosen based on the maximum possible trapping frequencies that maintain the chip currents below the maximum current limits. Additionally most chip based magnetic traps perform forced RF evaporation at a distance of 50-150 μm. Moving hot atoms closer than this to the chip typically results in a loss of atoms due to uncontrolled surface evaporation. After compressing the atoms to the final trap parameters the combined magnetic trap is held for several hundred ms to allow the atoms to thermalize and show the effects of the trap compression. The compression times are varied to maximize the atom number and the peak optical density (OD) of the atom cloud. At a few ms TOF the OD is proportional to the collision rate of the atoms in the magnetic trap. Starting with and maintaining a high collision rate (i.e. OD) is a key element of efficient evaporation.

The current chip (see Figure 4.16a) has interconnected wires and the dimple configuration needs to run current independently though the dimple wires. There are two basic ways to drive crossing wires that require independent current. The first way is to define a common grounding point often called a star ground. From that common ground point determine if a lead should be driven with a positive or a negative voltage (see Figure 4.16b). The current limits in the wires and the vias are always maintained below the damage limit. While this configuration is optimal this configuration is not used because the current safety trips in the chip power supplies (built at JILA) are very sensitive and trip when configured with a star ground.

The other solution works on the principle that voltage is a relative measure and as long as the references of the power supplies are independent the voltage difference between leads on the chip can be completely arbitrary. However the power supplies are

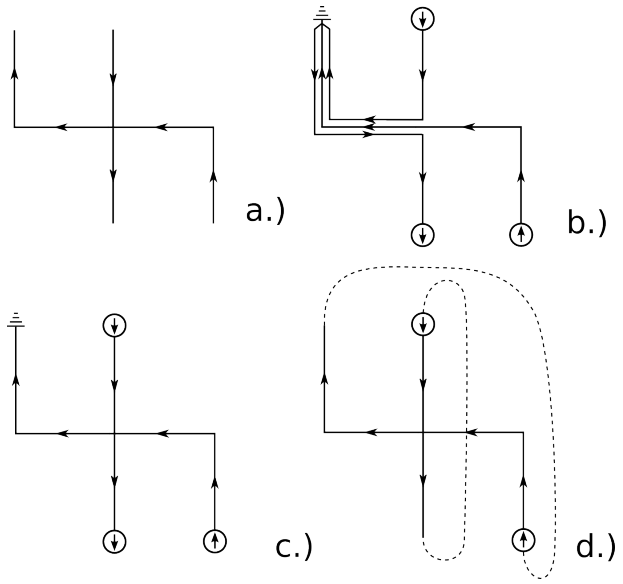

Figure 4.16: Schmatic diagram of current paths for driving interconnected wires on a chip.

not completely isolated as shown in Figure 4.16d. The power supplies are driven by a DAC in an electronics chassis so the voltages that are used to control the various power supplies are referenced to the same ground. Depending on the input configuration of the current driver the previously isolated supplies may be referenced though the control system. There are two basic ways to isolate the current drivers from the control ground: an isolation amplifier or an optical isolator or optocoupler. Each has its disadvantages in isolating analog signals because it involves chopping the input signal to capacitively isolate the signal. Because of the noise issues isolation amplifiers are not used in the current BEC system. For the data used in this thesis JILA built power supplies are used that are power isolated either by batteries or transformers. The control inputs are not isolated with a isolation amplifier or optical coupler but are isolated to a degree by using a differential amplifier on the control input. While the control inputs are not ideally isolated the current configuration of Figure 4.16d is faithfully reproduced in the experiment. This configuration has not been tested with other power supplies so caution should be used when trying this with other power supplies.

4.4.10 Evaporation

Linear instead of exponential RF sweeps are used to make BEC because evaporation is efficient when starting with a large initial atom number and tight magnetic trap. Additionally another group has used linear RF ramps to make BEC [13]. Because the trap consists of a larger IP trap with a dimple trap there are two regimes of RF evaporation and two RF sweeps. The RF sweeps are optimized at the beginning and end of each sweep for RF frequency and power and the length of each sweep is also adjusted. The metric for optimization depends on the BEC mode, but generally any changes made to the evaporation schedule should maintain peak OD. The process of optimizing the RF evaporation is covered in Chapter 5. While more evaportion stages with exponential ramp could be used two linear evapoartion stages gives a reasonable amount of room for optimization without being too complicated.

4.4.11 Imaging

The various stages of BEC production are optimized via analysis of absorption images of the clouds in time of flight (TOF) images. The atoms are illuminated for 100 μs by light resonant with the F=2→F'=3 transition. The light is sent though a long distance microscope (Infinity Photoptical K2 CF1/B objective with doubler tube) and is then imaged on a 12 bit CMOS camera (Basler 102A).

We are not aware of other groups using CMOS cameras for imaging BEC so we feel it warrants some discussion. CMOS cameras compared to CCD cameras are not known for excellent noise properties because each pixel in a CMOS camera has its own readout circuitry and in particular its own amplifier. In a single image there can be noise from pixel to pixel because of the individual performance of each pixel amplifier. While this noise would be significant in a single image the amplifier noise is not a factor in absorption imaging because each pixel is directly compared to itself

Stage	Time
MOT	1.2-6s
CMOT	25ms
molasses	5ms
optical pumping	0.25ms
Magnetic trap/transfer	300ms
transfer to chip	50ms
dimple	25ms
evaporation	1.2-4s

Table 4.1: Summary of the essential timing for the production of the BEC.

in absorption imaging and the amplifier gain is divided out when calculating the OD. Another potential drawback of the current CMOS camera is a low quantum efficiency 17% at 780 nn, but other CMOS sensors can be found with higher QE but less pixel depth. The readout of a CMOS camera is fast compared to a typical CCD camera (15 f/s @ 1320×1040 vs 2 f/s @ 1024×1024 for the Andor Pixus at 1 MHz readout) but the maximum pixel depth for CMOS cameras is 12 bits, where most CCD cameras start at 14 bits. For higher signal to noise images the CMOS camera falls behind the CCD, but for low cost, high speed, and reasonable images the CMOS camera is a good replacement (or second diagnostic camera) for CCD cameras in atomic physics experiments. In the current experimental configuration the image qualtiy is more limited by interference fringes from uncoated optical surfaces rather than the CMOS signal to noise ratio.

4.5 Typical operating parameters

The general sequence for BEC production is as follows (see Table 4.1 for a timing summary): the MOT is loaded for 1.2-6 s depending on the production mode (see Chapter 5 for the various BEC production modes). The 2D MOT lasers are shuttered 50 ms before the end of the 3D MOT stage to avoid light and atom beam scattering in the other stages of the experiment. Once the atoms are captured in the 3D MOT they are compressed and cooled by increasing the MOT field gradient to 21 G/cm, the 3D

MOT cooling laser is further detuned from 2Γ to 3Γ, and the repump power is reduced. At the same time the CMOT position is shifted ∼8 mm vertically by increasing B_z to ∼ 17 G. In the final 1 ms of the CMOT the cooling laser is further detuned to 10Γ. The 3D MOT magnetic fields are then switched off for 4 ms of optical molasses. After optical molasses the atoms are typically at a temperature of 20-40 μK. The atoms are then optically pumped into the $|2,2\rangle$ state.

The atoms are initially magnetically trapped by a current of 133 A in the EZ-wire, $B_y = 46$ G, and $B_x = 2$ G. In 325 ms the atoms are ramped to the surface by decreasing the current in the external Z-wire to 24 A, B_y to 48 G, and B_x to -22 G. The atoms are not significantly compressed during the transport and the trap depth is ∼ 1 mK so there is negligible loss due to atoms spilling over the top of the trap. At this point the atoms are about 4 mm from the chip surface. The compression wires and chip wires are ramped on as the atoms are moved to approximately 2 mm from the chip surface. At this stage the atoms are held by a combination of the external Z-wire and the chip Z-wire.

The atoms are transfered to the chip by fully ramping off the external Z-wire in 50 ms. After the atoms are transfered to the chip the dimple wire is ramped on in 30 ms. Forced RF evaporation is started immediately after ramping on the dimple trap. The trap is slightly decompressed during evaporation by reducing the dimple and B_x field commensurately. This keeps the trap bottom at nominally the same value but allows the trap frequencies to be slightly modified for optimal number or speed. The initial and final trap frequencies for the different evaporation modes are shown in Table 5.1. Because there are several BEC production modes the specifics of the RF cooling ramps and other evaporation details are detailed in the next chapter.

Chapter 5

BEC production

This chapter mainly covers the final step of BEC production (i.e. RF evaporation) and the final BEC numbers while all of the previous steps of laser cooling, magnetic trapping, etc. that are required to get to this point are covered in the previous chapter. Each of the BEC production modes in this chapter is slightly different because each mode is optimized for a different goal, in particular two modes are optimized for speed which optimization is different than optimizing for number. The first part of this chapter covers the procedure for optimizing for speed while the later sections report the final evaporation trajectories.

There is a direct trade off between production speed and the final BEC number. Increasing the production speed reduces the atom number in two ways: first the MOT

	High Rate	N Optimized	τ Optimized
MOT time (s)	1.7	6.0	1.2
N MOT (10^6)	∼300	∼500	∼200
N MT (10^6)	30-60% of N MOT		
Init. f_{trap}(z,ρ) (kHz)	0.84, 2.28	0.8, 2.3	0.8, 2.3
1st RF (MHz)	33→18	33→20	31→16
1st RF (s)	0.8	1.6	0.5
2nd RF (MHz)	18→3.5	20→3.9	16→3.65
2nd RF (s)	0.6	0.6	0.45
Final f_{trap}(z,ρ) (kHz)	0.76, 2.5	0.7, 2.5	0.8, 2.4
N BEC (10^3)	∼90	∼400	∼50

Table 5.1: Production parameters for the three BEC modes.

is typically loaded for less time resulting is a reduced atom number. The second issue is evaporating faster does not allow sufficient time for thermalization so continued evaporation will evaporate farther into the lower energy portion of the MB distribution. This aggressive evaporation will still cool the atom cloud because an increased amount of energy is removed from the cloud but it also removes more atoms reducing the net cooling efficiency. While the speed optimized evaporation rate is faster than the number optimized evaporation rate it must always be significantly slower than the rethermalization rate (see Equation 2.58). The speed optimized BEC production will start the evaporation at a deeper energy cut because the evaporation will remove a greater fraction of the high energy tail of the MB distribution (compare starting RF frequencies in Table 5.1).

Rapid BEC production starts by determining the start and stop frequencies of the evaporative cooling sweep. The start evaporation time is initially determined by evaporating from the point where evaporation just begins to cool the atom cloud (in this experiment ~ 30 MHz). The stop evaporation frequency is determined by partially cooling atoms and then determining the frequency when all of the atoms are evaporated from the trap. This frequency is the initial trap bottom and the stop frequency is set 200-400 kHz above the trap bottom. After the initial start and stop frequencies are determined the evaporation time is varied while maintaining the start and stop evaporation frequencies. The evaporation time that leaves $\sim 50 \times 10^3$ atoms is a reasonable initial evaporation time.

After the RF start/stop frequencies and evaporation time are roughly determined the evaporation is optimized. The evaporation is optimized by splitting the evaporation into two sweeps and optimizing each sweep for time and frequency, additionally the trap frequencies and RF power are also varied. The optimization procedure is similar to optimizing BEC for number, each parameter is optimized to maintain the final atom number while maintaing peak OD. The main difference is that the final number is

choosen to maintain signal to noise while the timing and RF parameters are optimized to cool the atoms to a BEC as fast as possible.

The optimization for each of the BEC modes in this chapter follows the above description for the speed optimized BEC production or References [14, 96] for number optimized BEC. Other BEC experiments have been optimized for different modes and the modes here are an extension of those experiments with improved speed and number [1, 13].

Results

5.1 30 shots

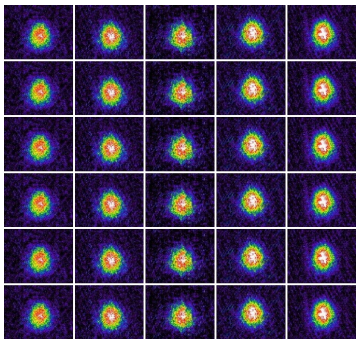

Figure 5.1: Images of 30 BECs made in less than 120 s. Each BEC is produced from MOT loading to imaging in 3.65 s.

In an effort to show the reproducibility of making BEC in a compact system BEC is made 30 times sequentially. This was done without data processing between the shots so the longer term behavior of a high repetition rate system system could be seen. The BEC production was optimized for speed as explained above however the BEC transition was not detected via a bimodal distribution or shape inversion. The bimodal signature was not used because expansion of the BEC due to the mean field was on the same order as the expansion of the thermal cloud [88] making it difficult to isolate the condensate fraction from the thermal fraction. Shape inversion was not used to detect

the transition because the relatively small difference between the trap frequencies of the tight and weak axis necessitated a long TOF which was complicated by the mean field expansion. With slightly different final trap frequencies shape inversion could be seen but the signal to noise made it difficult to accurately determine the BEC transition. The BEC transition was determined by a change in the effective area of the BEC cloud [97]. In the final data run the final RF frequency is well past the transition point so any fluctuations in the atom number will not significantly affect the transition point.

In the first set 30 images the atom number decreases with each successive shot (see Figure 5.2). This number loss is attributed to the silicon chip gradually heating from the Ohmic losses of the chip wires. Under normal operating conditions there is sufficient time for the chip to cool between shots because the process of producing a cloud of cold atoms, taking an image, and then processing takes at minimum 10-15 s. Even with a longer time between shots the slight heating of the chip increases vacuum losses by $\sim 10\%$ when shots are successively taken over a period of several minutes.

The chip is not easily cooled in the current configuration because the external Z-wire blocks access to the back of the chip (see Figure 4.11). Because the heating rate is small the chip was first cooled by flowing air around the chip and external Z-wire structure. The extra air cooling decreased the heating rate, however it increased imaging noise by exciting mechanical vibrations. While air cooling could be a long term solution it would most likely require significant modifications to the vacuum cell mounting and replacing the external Z-wire. Instead of air cooling the chip is cooled over the short term with a few drops of alcohol applied to the edges of the chip. A syringe is used to deliver the alcohol into the gap between the chip and the external Z-wire. The additional cooling from the alcohol significantly decreases the heating rate and 30 BECs are made in rapid succession (see Figure 5.1), but a slight drop in the atom number is apparent from a linear fit of the atom number (see Figure 5.2). The decrease is small over two minutes and may not be significant because of the variation

in the atom number.

The total time to make 30 BECs is less than 120 s. This time includes saving the images, but not image processing which occurs offline. For applications of BEC the data processing would most likely extract a single number that would use significantly less processing resources. Another application minded issue is the shot to shot number stability. As seen in Figure 5.2 the shot to shot variation is on the order of 20%. While 20% variation is less than desirable it is not a significant impediment to the goal of compacting and modularizing the BEC apparatus. Since the 30 shots and the number and speed data were taken an etalon mode was found in the MOT cooling laser delivery fiber that was one souce of noise. This fiber was flat polished on both ends and was replaced with an FC to APC PM fiber which reduced the number instability to $\sim 10\%$.

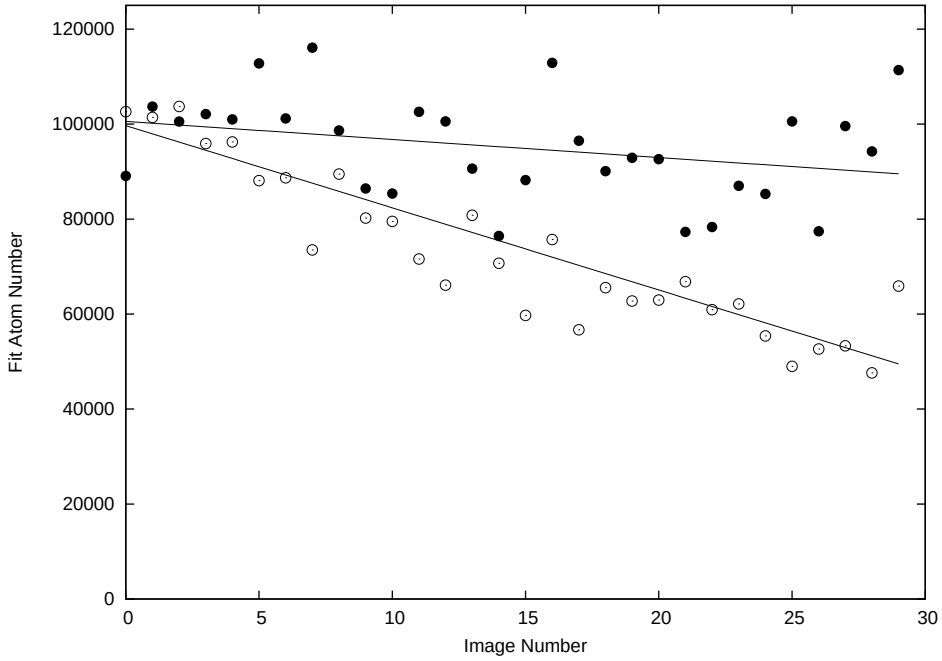

Figure 5.2: Atom number as a function of shot number in a rapid sequence (3.65 s production time per BEC) of 30 BECs. The open circles show mild chip heating as the experiment progresses. A few drops of alcohol applied to the back of the chip provide sufficient cooling to maintain atom number (filled circles).

5.2 Number optimized

After the demonstration of 30 consecutive BECs the apparatus was optimized to produce the largest possible condensate. The first and most obvious change to optimize the number is loading the MOT to saturation including a few extra seconds past the MOT loading exponential roll off to assure the largest possible number is captured in the MOT. Secondly, the RF evaporation sweeps in the optimal configuration were about two times longer than the high repetition rate optimization. However, increasing the evaporation time beyond a factor of two and/or reducing the trap frequencies to avoid three body loss did not improve the BEC number. The limited time optimization was traced to the chip magnetic trap lifetime of $\sim$2 s. Compared to the 7 s lifetime in the external Z-wire magnetic trap the chip Z-wire lifetime is considerably shorter.

This short lifetime in the chip Z-wire magnetic trap prevents a slower, more efficient evaporation that would lead to a larger BEC number. The vacuum cell used in this experiment was baked at 300°C for three days however a cell baked for 10–14 days had a slightly longer external Z-wire magnetic trap lifetime ($\sim$ 10 s) but effectively the same chip magnetic trap lifetime. Initially it would seem that chip heating would directly lead to the short chip magnetic trap lifetime but further experiments did not conclusively identify chip heating as the only source of atom loss. Other possible chip related loss mechanisms are collisions with the surface, Johnson current noise, and parametric heating in tight magnetic traps. None of these mechanisms individually was the most significant contributor to the number loss, so it appears that the loss may be a sum of plausible loss mechanisms.

As mentioned previously there is an approximate 10% atom loss due to residual heating from taking sequential shots every 15-30 s. For the maximum number there was a 10 minute cooling period between mapping out the BEC transition and taking the number optimized shots. The loss associated with residual heating was insignificant in

the second vacuum cell and the improved performace is attributted to the longer baking time.

5.3 Speed optimized

In optimizing the system to produce BEC as fast as possible the rubidium dispenser current was increased from 3.75 A to 3.85 A and a halogen bulb was placed close to the 2D MOT cell without interfering with the optical fields to generally heat the whole 2D MOT cell. These two changes increase the flux from the 2D MOT by 10-20%, but shorten the vacuum lifetime. The shorter vacuum lifetime did not affect the ability to produce BEC because the evaporation time was commensurately reduced maintaining the relative time scales (see Section 2.7). The evaporation trajectory was optimized for rapid evaporation following the procedure explained in the first section of this chapter. See Table 5.1 for final trap and RF evaporation parameters and BEC numbers. The transition to BEC was determined by the appearance of a bimodal cloud distribution. The bimodal shape is more easily seen in the speed optimized BEC production because the reduced atom number leads to a reduced mean field energy.

5.4 Vacuum lifetime, heating rates, and RF shield

As mentioned previously the external Z-wire magnetic trap lifetime is 7 s with the dispenser at 3.75 A and the 2D MOT cell heated to $80 - 90°$C. The 7 s lifetime is assumed to be primarily limited by the background vacuum pressure[1] . Below a rubidium dispenser current of 3.75 A the 2D MOT flux is a function of the dispenser current but the magnetic trap lifetime is constant. This is a result of the differential pumping between the high pressure and low pressure chambers being able to maintain a pressure differential of $\sim 10^3$. Above 3.75 A the 2D MOT flux continues to increase

[1] Stray resonant light was a source of loss after the initial 2D MOT laser setup. An IR viewer was used to search for light leaks that were not obvious. These light leaks were easily remedied by putting curtains around both the lasers and the experimental setup.

but the vacuum lifetime drops because the flux of rubidium atoms reaching the upper chamber is greater than the net rubidium pumping speed.

As mentioned previously the vacuum lifetime depends on the how recently the chip had been used to trap atoms. This vacuum dependence is due to the overall heating of the chip from Ohmic heating. Additionally the chip trap lifetime is 2-3 s shorter than the vacuum limited lifetime. This may be due to chip heating causing a temporary vacuum pressure increase while the chip is energized but efforts to isolate the short chip magnetic trap lifetime to heating were inconclusive.

The heating rate of atoms held in the magnetic trap just above the BEC transition temperature is 2.5(4) μK/s for the compressed(decompressed) trap. It is odd that the decompressed trap would have a higher heating rate but the decompressed trap frequencies may overlap with a mechanical/acoustic/electrical resonance in the experiment. Any heating is eliminated by applying an RF shield to maintain the cloud temperature while maintaining 95% of the atoms compared to no RF shield. When the atoms are evaporated to BEC the 1/e lifetime of the condensate is $\sim$300 ms with an optimized RF shield. The RF shield frequency is determined by looking at a long TOF (10 ms) and reducing the frequency while monitoring size and number. The optimal frequency will maintain the cloud size with the maximum possible number.

5.5 BEC production for atom interferometry

The purpose in compacting and simplifying the experimental aspects of a BEC machine is to enable future applications of BECs, in particular atom based interferometric sensors. Using light pulses to split and recombine atoms has been one of the most reliable implementations of an atom interferometer to date [98, 99, 100, 101, 102]. As a preliminary experiment a light pulse interferometer is implemented in the compact BEC system. A magnetic trap with low trap frequencies ($<$ 100 Hz) is optimal for splitting and recombining atoms with light pulses and some groups have taken considerable effort

to produce the weakest magnetic traps that can still hold against gravity [103]. The magnetic trap frequencies for manipulating atoms with light pulses is diametrically opposed to the conditions for producing BEC. Additionally atoms that have been cooled on a chip must be moved away from the chip (typically $< 100\,\mu$m) to approximately $300\,\mu$m. Translating cold atoms by a factor of three seems trivial but the trap frequencies scale proportional to $1/r^2$ so the trap frequencies can easily change by an order of magnitude during the transport. The atoms are first evaporated nearly to a BEC close to the chip and are then moved to the final position where the final evaporation step creates a BEC.

The magnetic trap is moved by adjusting the relative chip currents and bias fields, however moving the atoms and changing the trap frequency must be adiabatic ($d\omega/dt < \omega^2$) or sloshing and breathing modes will be excited in the atom cloud. The magnetic trap is transported with the trap frequencies as high as possible to avoid exciting other modes in the atom cloud. Once the atoms are translated to the new position a final evaporation sweep cools the atoms to a condensate. The final evaporation sweep is performed with a moderately tight trap to maintain a reasonable collision rate at the final magnetic trap position. The evaporation parameters are optimized similar to any other evaporation stage only the evaporation rate is not as fast.

The final step of preparing a BEC to be split with optical pulses is to decompress the atoms to the final magnetic trap frequencies while maintaining the position of the magnetic trap. After the trap has been decompressed to the final values the atoms are split with an optical standing wave. The trap frequencies of the final magnetic trap were (10, 90) Hz as measured by exciting a slosh mode and then fitting the data to a sine wave.

The timing and values of the currents and bias fields for transporting and decompressing the magnetic trap are shown in Figure 5.3. Additionally shown in the top graph of Figure 5.3 are the calculated trap frequencies. The ramp times for each operation are

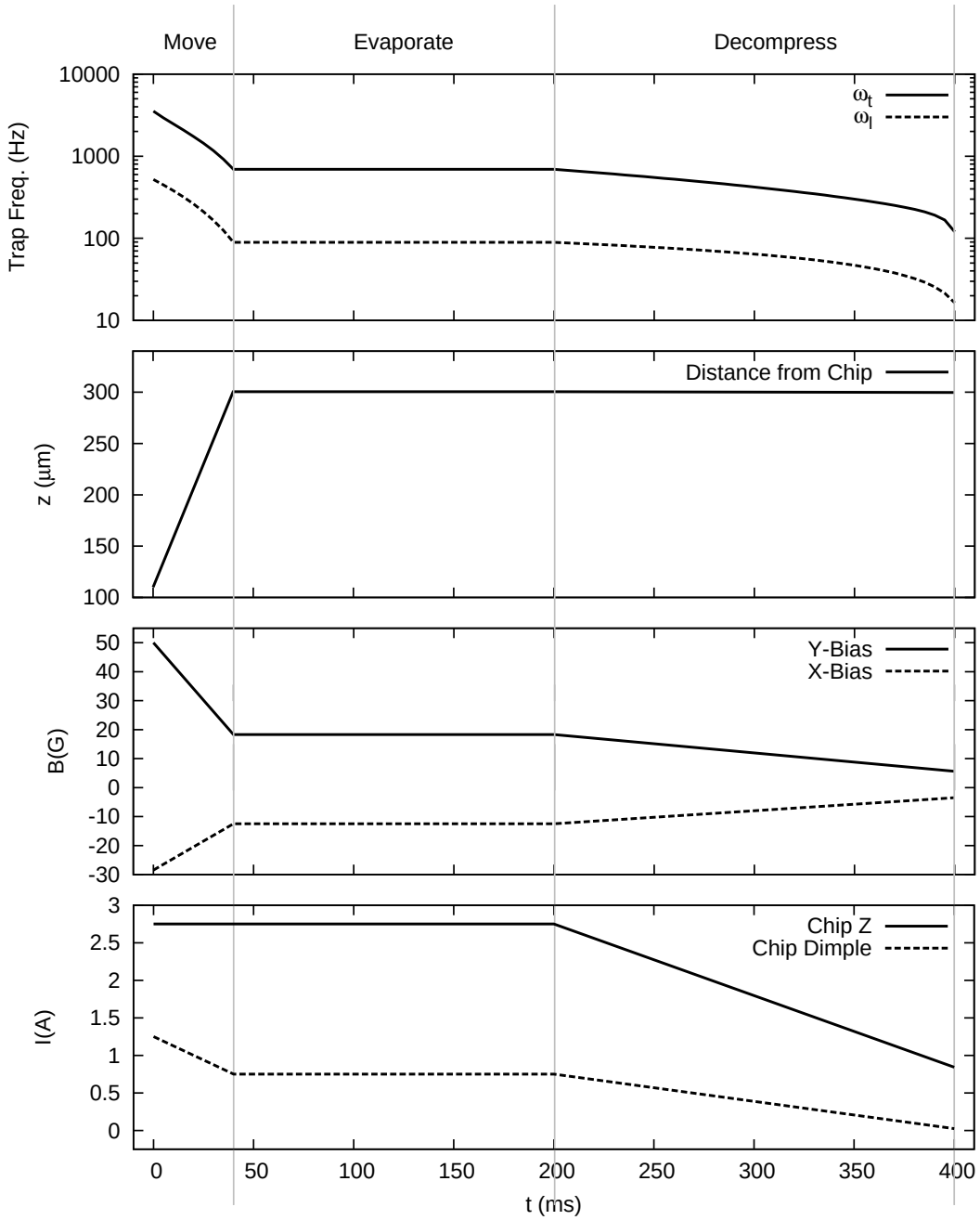

Figure 5.3: Timing and values from decompressing a compressed magnetic trap to a magnetic trap suitable for splitting and recombining cold atom clouds. This shows the B_x and B_y bias fields ($B_z = 0$), the currents in the external Z-wire, the compression wires, the chip Z-wire, and the dimple wire. The trap frequencies are calculated using the known trap parameters and equations from Chapter 2.

optimized by ramping the currents and bias fields to the new values and then holding the atoms at that stage for 0.3-1 s. This allows any breathing or sloshing modes to be damped out and converted to heat. The ramp times are then optimized to minimize heating and preserve number.

Chapter 6

Towards Applications of BEC

As explained in the introduction the purpose of compacting and simplifying a BEC was to enable applications of BEC. Applications involving coherent atom interferometry has attracted a significant amount of interest, specifically for building a rotation sensor based on the Sagnac effect. A Sagnac interferometer implemented with atoms should have an approximated 10^{11} increase in sensitivity compared to a comparable light interferometer [8].

Assuming the atoms already exhibit phase coherence, implementing a Sagnac interferometer requires three to four key components. The first component is a method to split the atoms in a way to preserves the phase for later measurement. The second component is a method to move the split clouds on a path that encloses area. The third component is a method to recombine the atoms in such a way that the output is dependent on the relative phase between the two packets. The final component is a method to detect the relative number of atoms in the output ports.

Each of these steps has been demonstrated previously but generally the steps of splitting, recombination, and detection have been performed without enclosing area. The one notable exception is an rotationally sensitive atom interferometer made by Mark Kasevich using a Bragg diffraction on a cloud or beam of laser cooled atoms [98]. There have been a few demonstrations of guiding atoms on a curved path [21, 22], but guiding atoms though curves has not recently received much attention.

There have been several demonstrations of atom interferometers that do not enclose area. The splitting and recombination mechanisms fall into a few broad categories: physical gratings [104], magnetic field potentials [105], optical double well potentials [106], dressed RF dressed potentials [107], and optical standing waves [99]. Several of these methods have drawbacks that would make it difficult to use these splitting methods in a broadly applicable device. Physical gratings require precise micro/nano machining, coherently splitting with magnetic fields requires precise control of the magnetic fields, and splitting with optical potentials does not exhibit phase reproducibility. Splitting with RF dressed potentials is straight forward and has demonstrated coherent phase reproducibility. Splitting with an optical standing wave is a good splitting method in terms of simplicity and flexibility. The laser frequency requirements are not stringent and a few milliwatts of power is more that enough power to split the atoms. Another benefit of splitting with optical fields is the momentum of the split atoms is >10 mm/s. This is significant because the act of splitting the atoms will separate the atom clouds and if properly configured could enclose area.

While these are the requirements of creating an atom interferometer building an interferometer is not the subject of this dissertation however there are a few preliminary splitting/recombining and interferometry experiments. Additionally a separate curved waveguiding experiment that will be discussed. These demonstrations are preliminary and are meant to be basic demonstration of the technologies required for an atom interferometer with an enclosed area and to debug any potential difficulties due to the compact nature of the apparatus.

6.1 Atom splitting and recombination

As mentioned previously not all methods of splitting atoms split with a reproducible phase. A pulsed light grating has been very successful at coherently splitting and recombining atoms with a reproducible phase up to a few hundred miliseconds when

decoherence or noise become significant [99, 102, 101]. This method is also very straight forward in its setup and operation. The theory of the splitting and recombination can be found in Reference [66]. While splitting with light pulses can be compared to a light transmission grating that diffracts atoms into various orders the behavior of the splitting requires considering the quantum mechanical nature of the atoms.

The setup and the basic operation of the splitting and recombination follow Reference [66]. One significant difference between this experiment and other atom chip based splitting experiments is the use of the atom chip to seal the vacuum system. The chip is slightly bowed in due to the external air pressure (see Figure 4.4). This bowing is unique to the compact vacuum system and is a consideration in the alignment of the splitting beam.

6.1.1 Optical setup

The optics setup for Bragg splitting atoms a few hundred microns from the chip starts with a beam with a waist smaller than half the distance from the chip to prevent light scattering from the chip. A lens with $\mathcal{F} = 500$ mm and an input beam size of 1.5 mm yields a beam with a theoretical beam waist of 280 μm and a Rayleigh range of 40 mm. The atoms are held at 300 μm from the chip to match the experimental parameters of [66], the beam waist of 280 μm should easily pass below the chip with negligible scattering off the chip. The Rayleigh range of 40 mm is chosen to maintain a small beam and flat wavefront over two times the distance between the center of the chip and the retroreflecting mirror (see Figure 6.1). Directly after the focusing optic a pair of waveplates sets the polarization of the beam parallel to the chip.

There are no easy reference marks on the chip and because the BEC is split in a weak dimple trap the trap axis is rotated relative to the chip wires. The position and angle of the splitting beam are adjusted using the optical setup shown in Figure 6.1. The lateral position of the splitting beam is adjusted by translating mirror M1. The

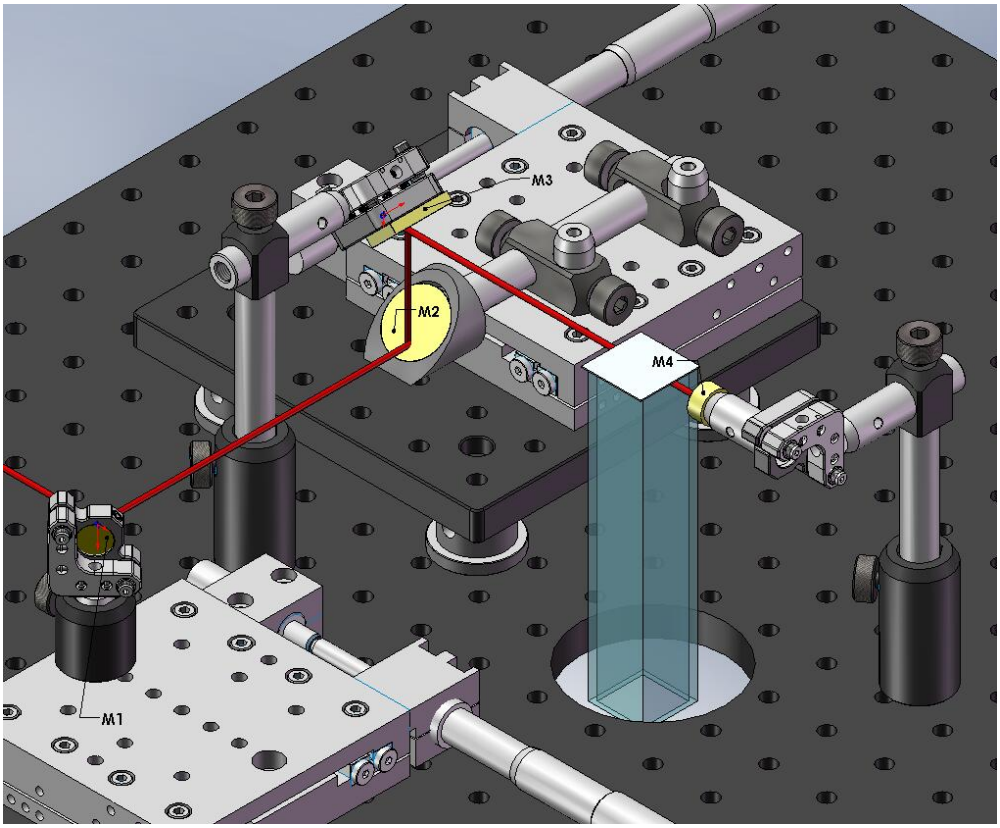

Figure 6.1: Setup for beamsplitting mirrors and translation stages relative to an atom chip and cell. Not shown are magnetic field coils or the optics for the 3D MOT or imaging beams.

vertical position and angle of the beam are adjusted by translating and rotating mirror M2. As mentioned one difference between this alignment and previous splitting beam alignments [99, 102] is the atom chip is bowed due to external air pressure. Fortunately the bowing of the atom chip creates a unique reflection signature that can be used to align the splitting beam parallel to the center region of the chip (see Figure 6.2).

Once the splitting beam is aligned parallel to the chip in the vertical direction the horizontal angle of the splitting beam is purposely set $2-3°$ relative to the cell wall for two reasons. The first is to better match the angle of the dimple trap with the splitting beam. The other reason is to avoid interference effects from the partial reflections from multiple passes though the cell walls. The angle is achieved by appropriately adjusting

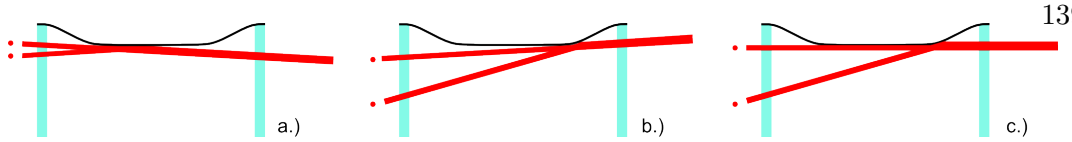

Figure 6.2: Alignment of splitting beam using the reflection signature from the deformed atom chip. The dots at the end of the beams show the expected pattern is the light is viewed with a card in the beam. Parts a.) and b.) show the signature when the splitting beam is angled relative to the flat center section of the chip. Part c.) shows the beam with the proper angle but too close to the chip. When the alignment is close the signatures of a.) and c.) can both be seen.

M2 remembering that rotating a mirror by θ results in a beam rotation of 2θ. After the splitting beam is aligned relative to the chip and cell wall the retroreflecting mirror (M4) is added and aligned to retroreflect the splitting beam. The final alignment is performed by holding a BEC in the splitting position and turning the splitting beam on for 10 ms. The splitting beam is aligned with the magnetic trap by adjusting M1 and M2 for maximal splitting loss. The power in the splitting beam is adjusted so there is always a small number of atoms at the minimum to better identify the optimal position. This method is sensitive to 20-40 μm which is about 10% of the beam diameter. Other alignment methods [108] improve on the loss based alignment by adjusting the beam position to minimize the splitting power needed to split the atoms without leaving atoms in the zero momentum order. For all of the data in the splitting section the splitting beam position was only optimized for loss with a continous 10-20 ms pulse.

6.1.2 Atom splitting optimization

The atoms are split by using a double pulse scheme [66] that allows the atoms to be split with high fringe contrast [84] into $\pm\hbar k$ orders. For diagnostics and testing both the double pulse format and a single pulse format were used to split the atoms. The splitting signature of the single pulse format qualitatively matches the splitting signal of Reference [66]. The agreement is only qualitative because the splitting power is not characterized for all AOM voltages. The maximum splitting power is $\sim$1.5 mW.

The splitting of the double pulse versus power also qualitatively agrees with data of Reference [66]. The power of the splitting beam varied over the time scale of a day so before each data set the splitting power of the double pulse sequence is adjusted to minimize the number of atoms in the central peak. Additionally during splitting and recombination data runs the splitting optimization is checked by turning off the recombination pulse and then taking several shots to verify the splitting condition is not drifting. The splitting condition typically did not drift over the period of a few hours so it is assumed the splitting and recombination data does not suffer from splitting power variations.

The objective of using a double pulse format instead of a single pulse format is to optimize splitting into the $\pm$ orders with no atoms in the zeroth order. In this experiment after the atoms are split the atom clouds sit on top of a background that makes it hard for the splitting power and time to be optimized (see Figure 6.3). Despite the background there it is possible to optimize the splitting such that there is no peak left in the middle of the distribution. This background can be attributed to three sources: collisions due to high atom density, a residual thermal background, and splitting beam inhomogeneities. Scattering due to high atomic density is a probable cause and is quickly solved by reducing the MOT loading time to reduce the final atom number. While reducing the MOT time is a quick fix it assumes the evaporation trajectory is still optimized for lower starting number. In this experiment reducing the MOT loading time reduced the atom number without sacrificing BEC production.

The other method for reducing the density of the atoms is to relax the trap frequencies to reduce the density of the cloud while maintaining atom number. This is the better way to deal with density related scattering because it maintains the atom number for signal to noise issues. However decompressing to a different trap frequency is slightly more involved because decompressing too fast can introduce breathing modes. The first trap used for atom splitting had trap frequencies of $\omega_{t,w} = (18, 180)$ Hz or

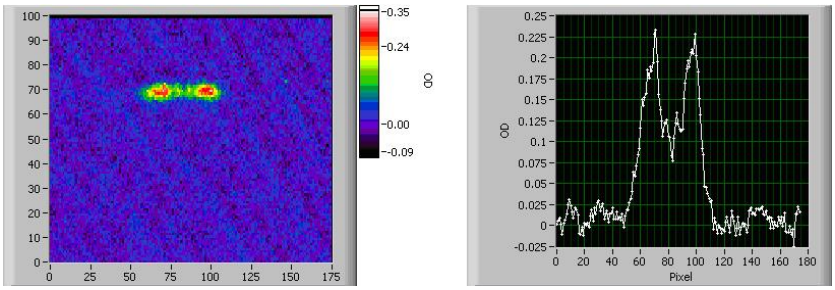

Figure 6.3: Image of atoms split with a double pulse. The atoms are split and are then propogated in the waveguide to separate the two clouds. The atoms are imaged after a few miliseconds of TOF. While two clouds are obviously visible the atom density does not go to zero for the optimal splitting time and power.

$\bar{\omega} \approx 80$ Hz with $20 - 30 \times 10^3$ atoms. Compared to previous splitting experiments of 10×10^3 atoms at $\bar{\omega} \approx 37$ Hz [66] and 8×10^3 atoms at $\bar{\omega} \approx 81$ Hz [27] the density of the initial trap is too high. The trap was then relaxed to $\omega_{t,w} = (12, 130)$ Hz with approximately the same atom number for $\bar{\omega} \approx 60$ Hz. Reducing the trap frequency made the splitting slightly better but did not notably change background atoms. Additionally the atom background is cleaner after the the atoms has been through one oscillation cycle. If the background was due to density collision then the atom clouds would have collided twice and should have doubled the scattered atom signal The improved background after two cycles seems to indicate atom density is not the cause of the atom background signal.

A background of thermal atoms is another possible cause of the background signal. While this is a plausible cause thermal atoms (beam and cloud) have been split and recombined using an optical standing wave [98, 100]. To test the splitting of a condensate versus a non-condensate the RF knife is held off the bottom by up to a few MHz. Increasing the RF knife (i.e. the atoms are hotter) by a few hundred kHz does not significantly change the appearance of the atom background. Increasing the RF knife further increases the temperature of the atom cloud significantly above the transition temperature. When the splitting pulse is applied to this hotter cloud the atoms still

split but the splitting modulation is on the order of 10-20% of the peak OD. It is obvious there is splitting and it is also obvious the background is significantly larger.

This extra background only happens when the cloud is significantly hotter. The temperature of the hot atoms was not measured, but small changes in the atom temperature around the BEC transition do not significantly change the background. Additionally there is no 'phase transition' from clean splitting to poor splitting when the cloud switches from a BEC to a thermal cloud. Thus a thermal cloud does not significantly contribute to the splitting background when the atoms a near condensate temperatures.

Another possible cause of the poor splitting is poor beam quality due to passing though the uncoated cell walls up to three times during the splitting. This was determined to be the cause of system instability in other BEC interferometry experiments [84]. Spatial intensity variations from interference can cause different parts of the BEC to experience different intensities and have different optimal splitting times. Variations in the splitting beam due to interference effects should be small because the beam is purposely aligned a few degrees off normal from the cell walls. Intensity variations could come from imperfections from the glass blowing, hand polishing, and anodic bonding procedures. There are no deep scratches in the area where the splitting beam passes though the cell but there are some areas of the cell that are obviously scratched. There are several obvious remedies: following References [99, 84] add optics to the chip to avoid passing light outside the cell, AR coat the cell walls, and/or improve the quality of the glass finishing near the chip.

6.1.3 Atom splitting and recombination data

The end goal of splitting and recombining the atom cloud is to make an interferometric measurement of some measurable quantity (e.g. rotation or gravity). A key requirement of any type of interferometer is the coherence length of the light, atoms, neutrons, etc. must be longer than the total length of the interferometer arms. The

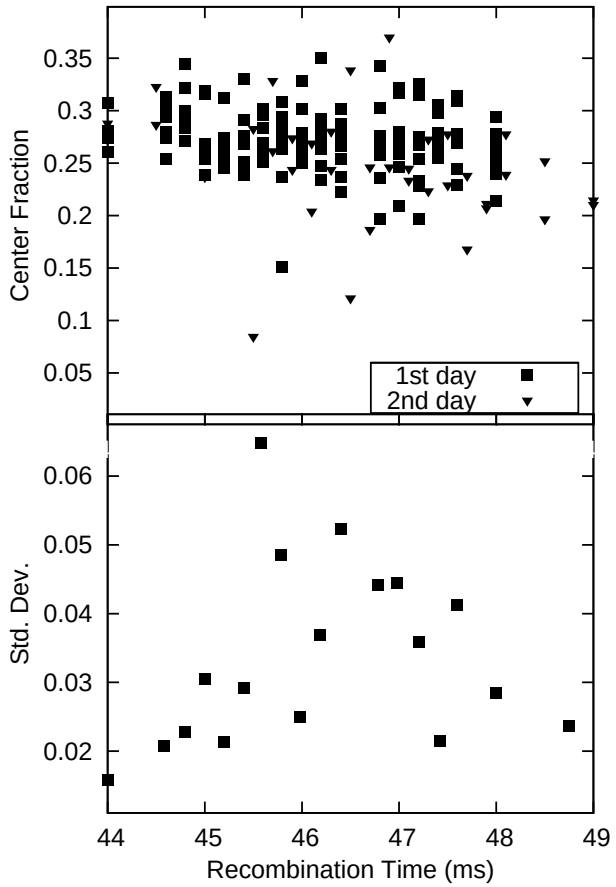

Figure 6.4: Increased noise in the splitting signal as a function of the recombination time. The upper graph shows the fraction of atoms in the center cloud compared to the fraction in the outer lobes. The lower graph shows a plot of the standard deviation of the upper data. The increased standard deviation is one sign of coherence between the atoms, however this data is significantly affected by noise or loss of coherence.

longest coherent time for the current state of the art is approximately one second, however phase can be recovered only out to ∼150 ms [109]. This can be compared to a light interferometer where for short arm separations there is a well defined fringe pattern at the output ports. When the arms are lengthened there is shaking fringe pattern indicating there is still coherence but the fringe variability is a result of significant noise in the system. If the light was incoherent when it reached the end of the interferometer there would be no fringes rather a constant intensity at the output ports. Thus an increase in noise at the correct recombination time indicates the split BEC packets are

still coherent but overwhelmed by technical noise.

As mentioned above one signature of coherence is increased noise when the atoms are recombined at the proper time. In an effort to see coherence effects in a BEC cloud the experiment of Reference [102] is recreated with a single laser frequency. In the case of a single splitting laser frequency the atoms are split near the bottom of the magnetic trap and then propagate out to the classical turning points where the atoms turn around. The atoms propagate back to the center of the weak dimple trap where a second double pulse is applied to recombine the atoms. The recombination time is initially determined by measuring the size of the cloud as a function of time in the waveguide without a recombination pulse. The apparent size of the cloud is minimized when the clouds are overlapping. The recombination time is varied around the overlapping recombination time. At each time multiple shots are taken at each time and the standard deviation of the point is plotted to better quantify the increased noise (see Figure 6.4).

6.2 Circular waveguiding

The other key element of implementing a rotation sensor is moving the atoms on a path that encloses area. One method for guiding atoms in a circle was implemented using a chip pattern shown in Figure 6.5. In this experiment the atoms are magnetically trapped and transported after being laser cooled. In principle a BEC could be transported with a similar moving trap assuming the acceleration is slow enough to avoid exciting low energy modes that are not visible with laser cooled atoms.

The trap confinement is the dot product of the external magnetic field with the spatially varying magnetic field created by the curved wire. This creates a curved wire magnetic trap

$$B(\theta) = \beta \frac{I}{z_0} \cos(\theta) - B_{\perp} \tag{6.1}$$

where θ determines a position along the curve of the wire. The trap can also be param-

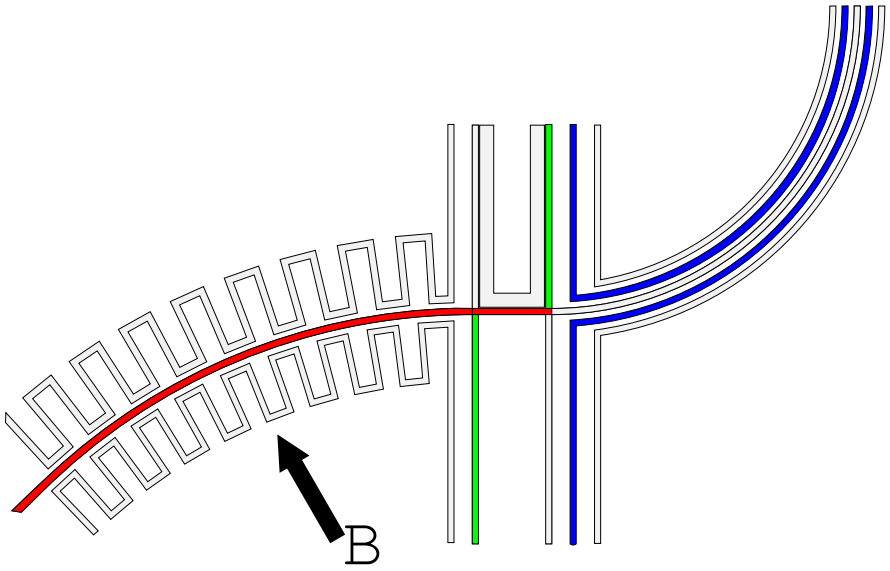

Figure 6.5: The chip design used for circular waveguiding. The red shaded wire is the circular guiding wire. The green shaded wires are the endcaps of the chip Z-wire that is used for the initial magnetic trap. The blue wires are briefly turned on when the atoms are released in the guide to increase the velocity of the atoms. Other wires on the chip (not shaded) are for other guiding options that were not pursued.

eterized along the arc of the curve

$$B(a) = \beta \frac{I}{z_0} \left(1 - \left(\frac{a}{r_w} \right)^2 \right) - B_\perp \tag{6.2}$$

where a is the coordinate along the arc and r_w is the radius of the wire. The trap curvature is

$$B''(a) = \beta \frac{2I}{r_w \, z_0}. \tag{6.3}$$

The compression of the atoms in the curved trap is proportional to the field at the trapping height and the radius of the trapping wire. The trap is moved by rotating the angle of $B_\perp$. As long at the wire has the same radius the trapping potential will always have the form of Equation 6.2 because of cylindrical symmetry.

The atoms are transported in the curved wire trap by a varying the angle of $B_\perp$ relative to the arc of the guiding wire. The angular rotation rate of the trap is simply the angular rotation rate of the magnetic field. Accelerating the atoms in a curved waveguide could be a very important part of an atom gyroscope because BEC

coherence times may be limited to a few hundred miliseconds. Atoms that are split with optical standing waves into $\pm\hbar k$ have velocities of ~ 12 mm/s. Using an interferometer with a 1 cm^2 enclosed area it would take 3-4 s to make one revolution; Far longer than the coherence time of the atoms. Actively accelerating the atoms after splitting could in principle enclose the same area on a much faster time scale.

In the curved waveguiding experiment the atoms are first captured in the chip Z-wire magnetic trap in the center of the wire pattern (see Figure 6.5). The atoms are launched into the curved waveguide by turning one leg of the chip Z-wire off and at the same time turning the curved wire current on. Turning off one side of the Z-wire allows creates a potential the pushes the atoms toward the curved wire. When the atoms reach the edge of the curve $B_\perp$ is rotated by changing the ratio of the B_x and B_y fields to match the velocity of the atoms in the waveguide. The atoms rotate the full extent of the curve (slightly more than a quarter circle) and at the end of the guide are recompressed because the guide abruptly ends. Figure 6.6 shows absorption images of the atom movement taken by reflecting the imaging beam off the chip at a near incident angle and then steering the light into a camera with mirrors.

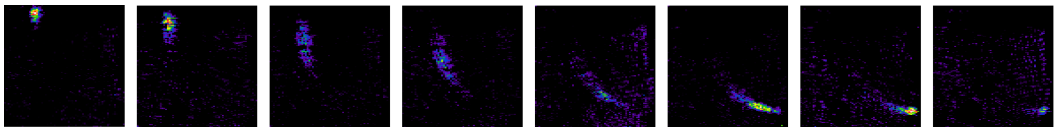

Figure 6.6: This shows atoms being guided 90° using a curved wire and a rotating bias field. The pictures images are taken at 4 ms intervals.

6.3 Future directions

The natural extension of this work is a vacuum system with more than two chambers so a MOT can be loaded while atoms are being evaporated in a light isolated region of the vacuum system. As seen in Table 4.1 the MOT loading and RF evaporation are

both accomplished in $\sim$ 1 s. With a few improvements the BEC duty cycle could be faster than 1 Hz. There are several design problems related to achieving this. One issue to solve is a method to transport the atoms between light isolated chambers. This could involve a moving shutter similar to Reference [110], but preferably a chamber could be designed that involved no moving parts but still maintain good light baffling. Anodic bonding could be used to construct a multichamber system and maintain a compact vacuum system.

The other extension of this work would be to implement an atom interferometer that encloses area and that can be used to detect rotation. There are several issues that need to be addressed. The first is a method to move atoms so they enclose a significant area ($\sim$ 1 cm^2). The other fundamental issue to be addressed is the coherence time of cold atoms in a magnetic trap. Reproducible phase has been demonstrated out to several hundred ms [109, 101], but at long times the interference fringes have low contrast or are overwhelmed by noise [102, 111]. This could be a technical noise issue and would require isolating the atoms from external influences or the dephasing could be a fundamental issue of atom interferometry [111].

Bibliography

[1] W. Hänsel, P. Hommelhoff, T. W. Hänsch, and J. Reichel. "Bose-Einstein condensation on a microelectronic chip". *Nature* **413**, 498 (2001).

[2] H. Ott, J. Fortágh, A. Grossmann, and C. Zimmermann. Bose-Einstein condensation in a surface microtrap. *Phys. Rev. Lett.* **87**, 230401 (2001).

[3] J. Fortágh, A. Grossmann, T. W. Hänsch, and C. Zimmermann. Fast loading of a magneto-optical trap from a pulsed thermal source. *J. App. Phys.* **84**, 6499 (1998).

[4] M. H. Anderson, J. R. Ensher, M. R. Matthews, C. E. Wieman, and E. A. Cornell. Observation of Bose-Einstein condensation in a dilute atomic vapor. *Science* **269**, 198 (1995).

[5] K. B. Davis, M. O. Mewes, M. R. Andrews, N. J. van Druten, D. S. Durfee, D. M. Kurn, and W. Ketterle. Bose-Einstein condensation in a gas of Sodium atoms. *Phys. Rev. Lett.* **75**, 3969 (1995).

[6] Heather J. Lewandowski, D. L. Whitaker, and Eric A. Cornell. Simplified system to create a Bose-Einstein condensate. *Journal of Low Temperature Physics* **132**, 309 (2003).

[7] S. Alshuler and L. M. Frantz, Matter wave interferometric apparatus, US Patent 3,761,721 (1973).

[8] Dmitry Budker, Derek F. Kimball, and David P. DeMille, *Atomic physics: An Exploration Through Problems and Solutions* (Oxford University Press, 2003).

[9] Erik W. Streed, Ananth P. Chikkatur, Todd L. Gustavson, Micah Boyd, Yoshio Torii, Dominik Schneble, Gretchen K. Campbell, David E. Pritchard, and Wolfgang Ketterle. Large atom number Bose-Einstein condensate machines. *Rev. Sci. Instrum.* **77**, 023106 (2006).

[10] J. Reichel. Microchip traps and BoseEinstein condensation. *Appl. Phys. B* **74**, 469 (2002).

[11] M.D. Barrett, J.A. Sauer, and M.S. Chapman. All-optical formation of an atomic Bose-Einstein condensate. *Phys. Rev. Lett.* **87**, 010404 (2001).

[12] Kurt Warren Miller, Trapping and cooling rubidium in far-off-resonant optical dipole traps, Ph.D. thesis, University of Colorado at Boulder (2004).

[13] M. Horikoshi and K. Nakagawa. Atom chip based fast production of Bose-Einstein condensate. *Appl. Phys. B* **3**, 363 (2006).

[14] Shengwang Du, Atom-chip Bose-Einstein condensation in a portable vacuum cell, Ph.D. thesis, University of Colorado at Boulder (2005).

[15] A. Einstein. Zur quantentheorie der strahlung. *Phys. Z.* **18**, 121 (1917).

[16] A. Einstein. Quantentheorie des einatomigen idealen gases. *Sitzungsber. Kgl. Preuss. Akad. Wiss.* p. 261 (1924).

[17] E.W. Hagley, L. Deng, W.D. Phillips, K. Burnett, and C.W. Clark. The atom laser. *Opt. Photon. News* (2001).

[18] Shengwang Du, Matthew B. Squires, Yutaka Imai, Leslie Czaia, R. A. Saravanan, Victor Bright, Jakob Reichel, T. W. Hänsch, and Dana Z. Anderson. Atom-chip Bose-Einstein condensation in a portable vacuum cell. *Phys. Rev. A* **70**, 053606 (2004).

[19] J. Hecht, *City of Light: The Story of Fiber Optics* (Oxford University Press, 1999).

[20] M.Bertolotti, *The History of the Laser* (Institute of Physics, 2005).

[21] D. Muller, D. Z. Anderson, R. J. Grow, P. D. D. Schwindt, and E. A. Cornell. Guiding neutral atoms around curves with lithographically patterned current-carrying wires. *Phys. Rev. Lett.* **83**, 5194 (1999).

[22] X. Luo, P. Krüger, K. Brugger, S. Wildermuth, H. Gimpel, M. W. Klein, S. Groth, R. Folman, I. Bar-Joseph, and J. Schmiedmayer. Atom fiber for omnidirectional guiding of cold neutral atoms. *Optics Letters* **29**, 2145 (2004).

[23] W. Ketterle and D. E. Pritchard. "Trapping and focusing ground state atoms with static fields". *Appl. Phys. B* **54**, 403 (1992).

[24] W. Petrich, M. H. Anderson, J. R. Ensher, and E. A. Cornell. Stable, tightly confining magnetic trap for evaporative cooling of neutral atoms. *Phys. Rev. Lett.* **74**, 3352 (1995).

[25] J. Reichel, W. Hänsel, and T. W. Hänsch. Atomic micromanipulation with magnetic surface traps. *Phys. Rev. Lett.* **83**, 3398 (1999).

[26] Jakob Reichel, W. Hansel, P. Hommelhoff, and T. W. Hänsch. Applications of integrated magnetic microtraps. *Appl. Phys. B* **72**, 81 (2001).

[27] Munekazu Horikoshi, Condensate interferometer on an atom chip, Ph.D. thesis, The University of Electro-Communications (2007).

[28] Spencer E. Olson, Rahul R. Mhaskar, and Georg Raithel. Continuous propagation and energy filtering of a cold atomic beam in a long high-gradient magnetic atom guide. *Phys. Rev. A* **73**, 033622 (2006).

[29] T. Lahaye, Z. Wang, G. Reinaudi, S. P. Rath, J. Dalibard, and D. Guery-Odelin. Evaporative cooling of a guided rubidium atomic beam. *Phys. Rev. A* **72**, 033411 (2005).

[30] T. Lahaye and D. Guéry-Odelin. Discrete-step evaporation of an atomic beam. *Eur. Phys. J. D* **33**, 67 (2005).

[31] A. Günther, M. Kemmler, S. Kraft, C. J. Vale, C. Zimmermann, and J. Fortágh. Combined chips for atom optics. *Phys. Rev. A* **71**, 063619 (2005).

[32] K. Lindquist, M. Stephens, and C. Wieman. Experimental and theoretical study of the vapor-cell Zeeman. *Phys. Rev. A* **46**, 4082 (1992).

[33] C. J. Dedman, J. Nes, and T. M. Hanna. Optimum design and construction of a Zeeman slower for use with a magneto-optic trap. *Rev. Sci. Instrum.* **75**, 5136 (2004).

[34] Harold J. Metcalf and Peter van der Straten, *Laser Cooling and Trapping* (Springer, 1999).

[35] William D Phillips. Nobel Lecture: Laser cooling and trapping of neutral atoms. *Rev. Mod. Phys.* **70**, 721 (1998).

[36] J. Dalibard and C. Cohen-Tannoudji. Laser cooling below the Doppler limit by polarization gradients: simple theoretical models. *JOSA B* **6**, 2023 (1989).

[37] W. Petrich, M. H. Anderson, J. R. Ensher, and E. A. Cornell. Behavior of atoms in a compressed magneto-optical trap. *J. Opt. Soc. Am. B* **11**, 1332 (1994).

[38] S. Wildermuth, P. Krüger, C. Becker, M. Brajdic, S. Haupt, A. Kasper, R. Folman, and J. Schmiedmayer. Optimized magneto-optical trap for experiments with ultracold atoms near surfaces. *Phys. Rev. A* **69**, 030901(R) (2004).

[39] B. Lev. Fabrication of micro-magnetic traps for cold neutral atoms. *Quantum Information and Computation* **3**, 450 (2003).

[40] C J Vale, B Upcroft, M J Davis, N R Heckenberg, and H Rubinsztein-Dunlop. Foil-based atom chip for Bose-Einstein condensates. *Journal of Physics B: Atomic, Molecular and Optical Physics* **37**, 2959 (2004).

[41] E. L. Raab, M. Prentiss, Alex Cable, Steven Chu, and D. E. Pritchard. Trapping of neutral sodium atoms with radiation pressure. *Phys. Rev. Lett.* **59**, 2631 (1987).

[42] Joseph Thywissen, Personal Communication.

[43] Valadin Vuletic, Personal Communication (2004).

[44] Igor Tepper, Personal Communication (2005).

[45] Fujio Shimizu, Kazuko Shimizu, and Hiroshi Takuma. Four-beam laser trap of neutral atoms. *Opt. Lett.* **16**, 339 (1991).

[46] Christopher R Monroe, Experiments with optically and magnetically trapped cesium atoms, Ph.D. thesis, University of Colorado at Boulder (1992).

[47] Joseph A. Schetz and Allen E. Fuhs, *Fundamentals of Fluid Mechanics* (John Wiley & Sons, 1999).

[48] A. L. Garcia, *Numerical Methods for Physics* (Prentice Hall, 2000), second edn.

[49] R. S. Conroy, Y. Xiao, M. Vengalattore, W. Rooijakkers, and M. Prentiss. "Compact, robust source of cold atoms for efficient loading of a magnetic guide". *Opt. Commun.* **226**, 259 (2003).

[50] W. D. Phillips and H. Metcalf. Laser deceleration of an atomic beam. *Phys. Rev. Lett.* **48**, 596 (1982).

[51] Z. T. Lu, K. L. Corwin, M. J. Renn, M. H. Anderson, E. A. Cornell, and C. E. Wieman. Low-velocity intense source of atoms from a magneto-optical trap. *Phys. Rev. Lett.* **77**, 3331 (1996).

[52] E. Riis, D. S. Weiss, K. A. Moler, and S. Chu. Atom funnel for the production of a slow, high-density atomic beam. *Phys. Rev. Lett.* **64**, 1658 (1990).

[53] James M. Kohel, Jaime Ramirez-Serrano, Robert J. Thompson, Lute Maleki, Joshua L. Bliss, and Kenneth G. Libbrecht. Generation of an intense cold-atom beam from a pyramidal magneto-optical trap: experiment and simulation. *J. Opt. Soc. Am. B* **20**, 1161 (2003).

[54] Milton Ohring, *The Material Science of Thin Films* (Elsevier, 1992).

[55] S. Dushman, *Scientific Foundations of Vacuum Technique* (John Wiley & Sons, 1962), second edn.

[56] Haruo Hirano, Yukihito Kondo, and Nagamitsu Yoshimura. Matrix calculation of pressures in high-vacuum systems. *J. Vac. Sci. Tech. A* **6**, 2865 (1988).

[57] A. Roth, *Vacuum Technology* (North-Holland, 1982), second edn.

[58] W. H. Kohl, *Handbook of Materials and Techniques for Vacuum Devices*, AVS Classics (American Institute of Physics, 1997).

[59] Makoto Yamashita, Masato Koashi, and Nobuyuki Imoto. Quantum kinetic theory for evaporative cooling of trapped atoms: Growth of bose-einstein condensate. *Phys. Rev. A* **59**, 2243 (1999).

[60] Makoto Yamashita, Masato Koashi, Tetsuya Mukai, Masaharu Mitsunaga, Nobuyuki Imoto, and Takaaki Mukai. Optimization of evaporative cooling towards a large number of bose-einstein-condensed atoms. *Phys. Rev. A* **67**, 023601 (2003).

[61] Wolfgang Ketterle. Nobel Lecture: When atoms behave as waves: Bose-Einstein condensation and the atom laser. *Rev. Mod. Phys.* **74**, 1131 (2002).

[62] E. A. Cornell, J. R. Ensher, and C. E. Wieman, *Proceedings of the International School of Physics "Enrico Fermi" Course CXL*, S. Stringari M. Inguscio and C. E. Wieman, eds. (1999), pp. 15–66.

[63] Kerson Huang, *Statistical Mechanics* (Wiley, 1963).

[64] J. Stickney, Personal Communication (2006).

[65] Christopher J Myatt, Bose-Einstein condensation experiments in a dilute vapor of rubidium, Ph.D. thesis, University of Colorado at Boulder (1997).

[66] Ying-Ju Wang, An on-chip atom interferometer using a bose-einstein condensate, Ph.D. thesis, University of Colorado at Boulder (2005).

[67] C. A. Sackett, C. C. Bradley, and R. G. Hulet. Optimization of evaporative cooling. *Phys. Rev. A* **55**, 3797 (1997).

[68] O. J. Luiten, M. W. Reynolds, and J. T. M. Walraven. Kinetic theory of the evaporative cooling of a trapped gas. *Phys. Rev. A* **53**, 381 (1996).

[69] K.B. Davis, M.-O. Mewes, and W. Ketterle. An analytical model for evaporative cooling of atoms. *Phys. Rev. Lett.* **74**, 3352 (1995).

[70] S. Aubin, E. Gomez, L. A. Orozco, and G. D. Sprouse. High efficiency magneto-optical trap for unstable isotopes. *Rev. Sci. Instrum.* **74**, 4342 (2003).

[71] B. McCarthy, Solder self-assembled, surface micromachined MEMS for micromirror applications and atom trapping, Ph.D. thesis, University of Colorado at Boulder (2004).

[72] ASM, *ASM Handbook: Volume 3: Alloy Phase Diagrams* (ASM International, 1992), 10th edn.

[73] J. Crank, *The Mathematics of Diffusion* (Clarendon Press, 1979).

[74] H. S. Carslaw and J. C. Jaeger, *Conduction of Heat in Solids* (Clarendon Press, 1947).

[75] Yip-Wah Chung, *Practical Guide to Surface Science and Spectroscopy* (Academic Press, 2001).

[76] W. Holmgren and D.Z. Anderson, WH took the gold rubidium pump data and fit the data to a model that DZA developed, Personal Communication (2006).

[77] George Wallis and Daniel I. Pomerantz. Field assisted glass-metal sealing. *Jourl. Appl. Phys.* **40**, 3946 (1969).

[78] Li-Anne Liew, Svenja Knappe, John Moreland, Hugh Robinson, Leo Hollberg, and John Kitching. Microfabricated alkali atom vapor cells. *Appl. Phys. Lett.* **84**, 2694 (2004).

[79] K. Dieckmann, R.C. Spreeuw, M. Weidemüller, and J.T.M. Walraven. Two-dimensional magneto-optical trap as a source of slow atoms. *Phys. Rev. A* **58**, 3891 (1998).

[80] S.L Rutherford, S. L. Mercer, and R. L. Jepsen. On pumping mechanisms in getter-ion pumps employing cold cathode gas discharges. *Transactions of the Seventh National Symposium on Vacuum Technology* p. 380 (1961).

[81] P. Krüger, X. Luo, M. W. Klein, K. Brugger, A. Haase, S. Wildermuth, S. Groth, I. Bar-Joseph, R. Folman, and J. Schmiedmayer. Trapping and manipulating neutral atoms with electrostatic fields. *Phys. Rev. Lett.* **91**, 233201 (2003).

[82] N. D. Bhaskar and C. M. Kahla. "Cesium gettering by graphite - Improvement in the gettering efficiency". *IEEE Trans Ultrason Ferroelectrics Freq Contr* **37**, 355 (1990).

[83] J. H. Moore, C. C. Davis, and M. A. Coplan, *Building Scientific Apparatus: A Practical Guide to Design and Construction* (Addison Wesley, 1983).

[84] K. J. Hughes, B. Deissler, J. H. T. Burke, and C. A. Sackett. High-fidelity manipulation of a Bose-Einstein condensate using an optical standing wave. *Phys. Rev. A* **76**, 035601 (2006).

[85] Produced in collaboration with Teledyne Scientific and Imaging, LLC.

[86] Carissa Tudryn, Stefan Schweizer, Ralph Hopkins, Linn Hobbs, and Anthony J. Garratt-Reed. Characterization of Si and CVD SiC to glass anodic bonding using TEM and STEM analysis. *J. Electrochem. Soc.* **152**, E131 (2005).

[87] M.B. Squires and B. Leuy, The control and imaging programs were designed based on our own experience and from talking with other groups at JILA. BL did the majority of the coding on the control program and MBS did most of the programming on the imaging program. (2005).

[88] W. Ketterle, D.S. Durfee, and D.M. Stamper-Kurn, *Proceedings of the International School of Physics "Enrico Fermi", Course CXL*, M. Inguscio, S. Stringari, and C.E. Wieman, eds. (IOS Press, 1999), p. 67.

[89] J. Schoser, A. Batar, R. Low, W. Schweikhard, A. Grabowski, Yu. B. Ovchinnikov, and T. Pfau. Intense source of cold Rb atoms from a pure two-dimensional magneto-optical trap. *Phys. Rev. A* **66**, 023410 (2002).

[90] Brian DeMarco, Quantum behavior of an atomic fermi gas, Ph.D. thesis, University of Colorado at Boulder (2001).

[91] Evan Salim and Simon Braun, Personal Communication (2006).

[92] C. Salomon, J. Dalibard, W.D. Phillips, A. Clairon, and S. Guellati. Laser cooling of cesium atoms below 3 μk. *Europhys. Lett.* **12**, 683 (1990).

[93] T. Walker, D. Sesko, and C. Wieman. Collective behavior of optically trapped neutral atoms. *Phys. Rev. Lett.* **64**, 408 (1990).

[94] Harold J. Metcalf and Peter van der Straten, *Laser Cooling and Trapping* (Springer, 1999).

[95] Peter D. D. Schwindt, Magnetic traps and guides for bose-einstein condensates on an atom chip: Progress toward a coherent atom waveguide beamsplitter, Ph.D. thesis, University of Colorado at Boulder (2003).

[96] H.J. Lewandowski, Coherences and correlations in an ultracold bose gas, Ph.D. thesis, University of Colorado at Boulder (2002).

[97] J E Lye, C S Fletcher, U Kallmann, H-A Bachor, and J D Close. Images of evaporative cooling to Bose-Einstein condensation. *J. Opt. B* **4**, 57 (2002).

[98] B. Young, M. Kasevich, and S. Chu, *Atom Interferometry* (Academic Press, 1997), chap. Precision atom interferometry with light pulses, p. 363.

[99] Y.-J. Wang, D. Z. Anderson, V. M. Bright, E. A. Cornell, Q. Diot, T. Kishimoto, M. Prentiss, R. A. Saravanan, P. D. D. Schwindt, S. R. Segal, and S. Wu. Atom Michelson interferometer on a chip using a Bose-Einstein condensate. *Phys. Rev. Lett.* **94**, 090405 (2005).

[100] S. Wu, E. Su, and M. Prentiss. Demonstration of area-enclosing guided-atom interferometer for rotation sensing. *Phys. Rev. Lett.* **99**, 173201 (2007).

[101] O. Garcia, B. Deissler, K.J. Hughes, J.M. Reeves, and C.A. Sackett. Bose-Einstein condensate interferometer with macroscopic arm separation. *Phys. Rev. A* **74**, 031601(R) (2006).

[102] Munekazu Horikoshi and Kenichi Nakagawa. Dephasing due to atom-atom interaction in a waveguide interferometer using a Bose-Einstein condensate. *Phys. Rev. A* **74**, 031602(R) (2006).

[103] C.A. Sackett. Limits on weak magnetic confinement of neutral atoms. *Phys. Rev. A* **73**, 013626 (2006).

[104] David W. Keith, Christopher R. Ekstrom, Quentin A. Turchette, and David E. Pritchard. An interferometer for atoms. *Phys. Rev. Lett.* **66**, 2693 (1991).

[105] Y. Shin, C. Sanner, G.-B. Jo, T. A. Pasquini, M. Saba, W. Ketterle, D. E. Pritchard, M. Vengalattore, and M. Prentiss. Interference of Bose-Einstein condensates split with an atom chip. *Phys. Rev. A* **72**, 021604(R) (2006).

[106] Y. Shin, M. Saba, T. Pasquini, W. Ketterle, D.E. Pritchard, and A.E. Leanhardt. Atom interferometry with Bose-Einstein condensates in a double-well potential. *Phys. Rev. Lett.* **92**, 050405 (2004).

[107] T. Schumm, S. Hofferberth, L.M. Anderson, S. Wildermuth, S. Groth, I. Bar-Joeseph, J. Schmiedmayer, and P. Kroger. Matter-wave interferometry in a double well on a atom chip. *Nature Physics* **1**, 57 (2005).

[108] Steven Segal, Personal Communication (2007).

[109] G.-B. Jo, Y. Shin, S. Will, T. A. Pasquini, M. Saba, W. Ketterle, D. E. Pritchard, M. Vengalattore, and M. Prentiss. Long phase coherence time and number squeezing of two Bose-Einstein condensates on an atom chip. *Phys. Rev. Lett.* **98**, 030407 (2007).

[110] A. P. Chikkatur, Y. Shin, A. E. Leanhardt, D. Kielpinski, E. Tsikata, T. L. Gustavson, D. E. Pritchard, and W. Ketterle. A continuous source of Bose-Einstein condensed atoms. *Science* **296**, 2193 (2002).

[111] J. H. T. Burke, B. Deissler, K. J. Hughes, and C. A. Sackett. Experimental investigation of confinement effects in a condensate interferometer with interaction times up to one second. *arXiv* p. 0710.1081 (2007).

Appendix A

Monte Carlo for MOTs

Here is the front end for setting up the MOT MC

```
clear all;

%  The front end to vary the starting position and velocities
%     of the experiment

% Assume the atoms are in a box of width w and laser beams have a
%     diameter d_laser (defined in the called function);

% How long the solver should run and size of the cell
t=linspace(0,.5,1000);
w = 6e-2;

% Define all of the relevant constants once so they can be called
%     from a subroutine.  The variable must be globals to be
%     accessed from inside the called function
global g = 2*pi*6e6;
global hbar = 1.05e-34;
global lambda = 780e-9;
global k=2*pi/lambda;
global I0=4.1;
global I=6;
global S = I/I0;
global N=2;
global dl = 2*g;
global mohb = 8.8e10;
global Bp = 0.15;
global m = 87*1.66e-27;
global r=6e-3;
global o=2.5e-3;
```

```
% some combined values
global prefactor=k*hbar*g*I/2/I0/m;
global OpNS = 1+N*S;
global mohbTBp = mohb*Bp;
global Fdgs = 4/g/g;
global thetaBeam;
global wCell = w;

% The range of values that will be calculated

y_start = 0;
y_end = w/2;

theta_start = -80;
theta_end = 80;

t1=time();
xnot = -w/2;

% Loop over the angle of the MOT beams
for thetaB=0:5:90

%thetaBeam = 45;
thetaBeam = thetaB*pi/180;


% Dummy variable to keep track of the output data
m = 1;

%%%%%%%%%%%%%%%%%%%%%%%%%%%%%%%%%%%%%%%%%%%%%%%%%%%%%%%%%%%%%%%%%%%%%%%
%                                                                      %
% Only look along the upper left hand verticle wall %
%                                                                      %
%%%%%%%%%%%%%%%%%%%%%%%%%%%%%%%%%%%%%%%%%%%%%%%%%%%%%%%%%%%%%%%%%%%%%%%

% Position of atoms along wall
for ynot=y_start:w/20:y_end

% Angle of atoms leaving the wall
for thetaDeg=theta_start:10:theta_end

theta = thetaDeg*pi/180;

upper = 150;
lower = 0;

for n=1:8
```

```
% Perform 8 steps of the bisection method to find the
%     capture velocity.  Use bisection because the capture
%     velocity transition is binary

v = ( upper + lower )/2;

%x=[xnot,v*cos(theta),ynot,v*sin(theta),thetaBeam,w];
x=[xnot,v*cos(theta),ynot,v*sin(theta)];

xf = lsode("MOT2DAngledTopHatBeams",x,t);
final = length (xf);
final_v=sqrt( xf(final,2)^2 + xf(final,4)^2 );

final_r=sqrt( xf(final,1)^2 + xf(final,3)^2 );

% Check to see if the atoms have been cooled below a small value
%     and are near the center of the laser beams
if ( (final_v < .05) && (final_r < 1e-3) )
lower = v;
else
upper = v;
endif
endfor
v = ( upper + lower )/2;
% take into account the last iteration for the final value
%      of the capture velocity and then save the data

output(m,1) = xnot;
output(m,2) = ynot;
output(m,3) = theta;
output(m,4) = v;
m=m+1;

endfor

endfor

name1 = "VcaptureFullAngle_wCell_6cm__dbeam_10cm__theta_beams_";
name2 = "deg.dat";
name = strcat(name1, dec2base(thetaB,10), name2);

save("-text", name, "output");

endfor

total_time=(time() - t1)/60
```

Here is the function called by the ODE

```
function xdot = MOT2DAngledTopHatBeams (x, t)

%  SPEED NOTES
%  Dot products in Matlab/Octave are incredibly slow compared
%     to multiplying and adding by hand.  Because the vectors
%     are in 2D it is just as easy to write out the whole form
%     and get a speed bump

%  Referencing and building arrays is slow so if a variable
%     is called several times it is worth it to declare a
%     variable so the array is only reference once

%  To speed up the computation all of these variables should
%     be declared in the main calling program but need to be
%     defined here so they can be referenced

global k;
global dl;
global prefactor;
global OpNS;
global mohbTBp;
global Fdgs;
global thetaBeam;
global wCell;

%theta = x(5);
xX = x(1);
xY = x(3);
%wCell = x(6);

tan_theta = tan(thetaBeam);
cos_theta = cos(thetaBeam);
sin_theta = sin(thetaBeam);
wB=10e-2;

% First determine if the particle is in the plus beam by looking at
%     the sign of the position relative to the extents of the beam
upper = xX*tan_theta+wB/2/cos_theta;
lower = xX*tan_theta-wB/2/cos_theta;

% if the particle is inside the plus beam this value will be positive
inplus = (xY-upper)*(lower-xY);

% Now the same for the minus beam
```

```
upper = -xX*tan_theta+wB/2/cos_theta;
lower = -xX*tan_theta-wB/2/cos_theta;
inminus = (xY-upper)*(lower-xY);

% Now make sure the particle is inside the cell width
in_x = ( -wCell/2-xX )*( xX-wCell/2 );
in_y = ( -wCell/2-xY )*( xY-wCell/2 );

inside = in_x > 0 && in_y > 0;

r= sqrt(xX^2+xY^2); % Assume MOT is centered at orgin

% Calculate force from plus beam if conditions are right
if ( inside*inplus > 0 )
% determine the alignment of the magnetic field (quantization axis)
%    with the direction of the laser field and calculate once
alignP= ( cos_theta*xX + sin_theta*xY )/r;

dotkpv = k*( cos_theta*x(2) + sin_theta*x(4) );
Fp=prefactor*(1/(OpNS+Fdgs*(dl+dotkpv+alignP*mohbTBp*r)^2) \
     -1/(OpNS+Fdgs*(dl-dotkpv-alignP*mohbTBp*r)^2));
else
   Fp=0;
endif

% Repeat for the minus beam
if ( inside*inminus > 0 )
alignM= ( cos_theta*xX - sin_theta*xY )/r;

dotkmv = k*( cos_theta*x(2) - sin_theta*x(4) );
Fm=prefactor*(1/(OpNS+Fdgs*(dl+dotkmv+alignM*mohbTBp*r)^2) \
     -1/(OpNS+Fdgs*(dl-dotkmv-alignM*mohbTBp*r)^2));
else
  Fm=0;
endif

% Now update the xdot vector for the next iteration of the ODE

xdot(1) = x(2);
xdot(2) = Fp*cos_theta+Fm*cos_theta;
xdot(3) = x(4);
xdot(4) = Fp*sin_theta-Fm*sin_theta-9.8; % Include gravity
%xdot(5) = 0;
%xdot(6) = 0;

endfunction
```